Electrokinetic, Optical And Rheological Study Of Ordered Polymer Colloids And Its Rheological Implications On Printing.

Order Number 9129994

Electrokinetic, optical and rheological study of ordered polymer colloids and its rheological implications on printing

Lee, Yann-Per, Ph.D.

Lehigh University, 1991

U·M·I
300 N. Zeeb Rd.
Ann Arbor, MI 48106

ELECTROKINETIC, OPTICAL AND RHEOLOGICAL STUDY OF ORDERED POLYMER COLLOIDS AND ITS RHEOLOGICAL IMPLICATIONS ON PRINTING

by

Yann-Per Lee

A Dissertation

Presented to the Graduate Committee

of Lehigh University

in Candidacy for the Degree of

Doctor of Philosophy

in

Polymer Science and Engineering

Lehigh University

1991

Certificate of Approval

Approved and recommended for acceptance as a dissertation in partial fulfillment of the requirements for the degree of Doctor of Philosophy.

1/18/91
(date)

F. J. Micale
F. J. Micale, Professor in Charge

Accepted 1/18/91
(date)

Special committee directing
the doctoral work of
Yann-Per Lee

F. J. Micale
F. J. Micale, Chairman

M. S. El-Aasser

C. Silebi

H. D. Ou-Yang

Diego Valenzuela
D. Valenzuela

Acknowledgements

The author would like to express his sincere gratitude to the following people and institutions for their contributions during his years of graduate study:

Dr. F. J. Micale for his advice, guidance, and support throughout this work.

Dr. M. S. El-Aasser for his generous help and valuable discussion.

Dr. C. Silebi for his interest and for serving on the Dissertation Committee.

Dr. H. D. Ou-Yang for his helpful suggestion and continuous encouragement.

Dr. D. Valenzuela for his assistance and enthusiasm in this work.

Dr. Jiann Lin for his help in the reflection spectrophotometry work.

The staff and colleagues of the Printing inks Program for their friendship.

The Printing inks Program and Lehigh University for financial support.

The author's parents for their tremendous support.

The author's wife, Yuan-Yu, for her endless love, support and encouragement and for her patience in typing this dissertation.

Table of Contents

Abstract 1

1. GENERAL INTRODUCTION 3

2. CHARACTERIZATIONS OF MODEL COLLOIDS 8

2.1 INTRODUCTION 8
2.2 EXPERIMENTAL 12
2.2.1 Materials 12
2.2.2 Latex Cleaning by Serum Replacement 12
2.2.3 Particle Size Determination by Transmission Electron Microscopy 13
2.2.4 Conductometric Titration 13
2.2.5 Fourier Transform Infrared Spectroscopy 14
2.3 RESULTS AND DISCUSSION 15

3. INVESTIGATIONS OF PARTICLE INTERACTIONS 20

3.1 INTRODUCTION 20
3.2 EXPERIMENTAL 26
3.2.1 Materials 26
3.2.2 Microelectrophoresis 27
3.3 RESULTS AND DISCUSSION 28

4. EXPLORATIONS OF DISPERSION MICROSTRUCTURE 39

4.1 INTRODUCTION 39
4.2 EXPERIMENTAL 41
4.2.1 Materials 41
4.2.2 Reflection Spectrophotometry 42
4.3 THEORY OF BRAGG DIFFRACTION 42
4.3.1 Experimental Nearest Interparticle Distance (D_e) 43
4.3.2 Theoretical Nearest Interparticle Distance (D_t) 45
4.3.3 Estimated Irradiation Penetration Depth in Dispersion (t) 46
4.4 RESULTS AND DISCUSSION 48

5. RHEOLOGICAL STUDIES 59

5.1 INTRODUCTION 59
5.1.1 Historical Background 61
5.1.2 Role of Colloidal Forces in Dispersion Rheology 62
5.2 EXPERIMENTAL 66
5.2.1 Materials 66
5.2.2 Rheometry 67
5.3 THE THEORETICAL SHEAR MODULUS OF ORDERED LATEXES 69
5.4 RESULTS AND DISCUSSION 71
5.4.1 Steady State Viscometry 71
5.4.2 Dynamic Oscillation 81
5.4.3 Strain Sweep 84
5.4.4 Flow Oscillation 93
5.4.5 Stress Relaxation 95

5.4.6 The Comparison Between Experimental and Theoretical Shear Modulus 99
6. THE ORDER-DISORDER PHASE TRANSITION 106
6.1 INTRODUCTION 106
6.2 THEORY OF ORDER-DISORDER PHASE TRANSITION 109
6.2.1 Kirkwood-Alder Transition Theory and Hard Sphere Model for ϕ-[Salt] Phase Diagram 109
6.2.2 Thermodynamics for T-ϕ Phase Diagram 111
6.3 RESULTS AND DISCUSSION 113
7. THE RHEOLOGICAL IMPLICATIONS ON PRINTING 125
7.1 INTRODUCTION 125
7.2 EXPERIMENTAL 127
7.2.1 Model Inks 127
7.2.2 Ink Rheology 127
7.2.3 Ink Transfer 128
7.3 THE RHEOLOGICAL CONCEPTS 129
7.4 RESULTS AND DISCUSSION 130
7.4.1 Correlation of Ink Transfer with Dynamic Ink Rheology 130
7.4.2 Phase Diagram of Printing Inks 140
8. CONCLUSIONS 146
Reference 158
Vita 167

List of Figures

Figure 1-1: *Experimental research program of ordered polymer colloids.* 6

Figure 2-1: *TEM micrograph of latex A.* 15

Figure 2-2: *Conductometric titration of cleaned latex A (0.2474 g solids in 60 g dispersion) with 0.02 N NaOH(aq).* 17

Figure 2-3: *Infrared spectra of (a) standard polystyrene sample (b) latex A.* 19

Figure 3-1: *Schematic representation of the structure of the electrical double layer.* 22

Figure 3-2: *The schematic diagram of total potential energy between a pair of particles.* 24

Figure 3-3: *Electrophoretic mobility vs pH for latex A at various NaCl concentrations (mole/l) at 25 °C.* 30

Figure 3-4: *Electrophoretic mobility as a function of salt valency and salt concentration for latex A at 25 °C.* 31

Figure 3-5: *Dimensionless zeta potential vs. $a\kappa_o$ for latex A in various aqueous salt solutions at 25 °C.* 32

Figure 3-6: *Electrophoretic mobility vs. temperature for latex A at various aqueous NaCl concentrations (mole/l).* 34

Figure 3-7: *Zeta potential vs. temperature for latex A at various aqueous NaCl concentrations (mole/l).* 35

Figure 3-8: *Effect of 1:1 electrolyte concentration on the total pair potential energy curve for latex A at 25 °C; curves drawn with constant values of A_{121} ($3.5x10^{-21}$ Joule) and Ψ_d (16.5 mv); kT on y axis = $4.11x10^{-21}$ Joule.* 37

Figure 3-9: *Effect of temperature on the total pair potential energy curve for latex A; curves drawn with constant values of A_{121} ($3.5x10^{-21}$ Joule), Ψ_d (16.5 mv) and 1:1 electrolyte concentration (10^{-6} mole/l); kT on y axis = $4.11x10^{-21}$ Joule (at 25 °C).* 38

Figure 4-1: *Instrument configuration for reflection spectra measurements.* 42

Figure 4-2: *Optical cell for reflection spectra measurements.* 43

Figure 4-3: *Unit cells for bcc and fcc structure.* 44

Figure 4-4: *Typical reflection spectrum at constant diffraction angle.* 47

Figure 4-5: *Reflection spectra of cleaned latexes A at various particle volume fractions and 22 °C (intensity x 4 for secondary peaks).* 49

Figure 4-6: *Dimensionless nearest interparticle distance vs. particle volume fraction for cleaned latexes at 22 °C; ⊡: experimental data from reflection spectra, solid lines: theoretical calculation for perfect crystal lattice.* 50

Figure 4-7: *Effect of temperature (in °C) on reflection spectra of cleaned latexes A at various particle volume fractions ϕ (a) 6.25 % (b) 9.82 % (c) 18.28 % (d) 23.22 % (numbers on* 52

curves indicate temperature).
Figure 4-8: *Effect of temperature on the experimental nearest interparticle distance for cleaned latexes A at ϕ=6.25%.* 54
Figure 4-9: *Effect of salt concentration (in mole/l) on reflection spectra of latexes A with ϕ=9.03% at 22 °C.* 55
Figure 4-10: *Effect of salt valency on reflection spectra of latexes A with ϕ=9.03% at 22 °C and various salt concentrations.* 57
Figure 5-1: *The viscosity profile of cleaned latex A at various particle volume fractions at 25°C.* 72
Figure 5-2: *The low and high shear viscosity of cleaned latex A as a function of volume fraction at 25 °C (η_o=0.8937 mPas).* 74
Figure 5-3: *The viscosity profile of cleaned latex A at various temperatures (°C).* 76
Figure 5-4: *The temperature dependence of viscosity of cleaned latex A at various particle concentrations and shear rates.* 77
Figure 5-5: *Effect of salt concentration (mole/l) and valency on the viscosity profile of latex A with ϕ=8.96% at 25°C.* 79
Figure 5-6: *Effect of salt valency and concentration on the viscosity of latex A with ϕ=8.96% at 25°C and various shear rates.* 80
Figure 5-7: *Effect of frequency on the storage modulus G', loss modulus G", phase shift δ ($\tan^{-1}$(G"/G')) and dynamic viscosity η' of cleaned polystyrene latex A with ϕ=26.97% at 35°C.* 83
Figure 5-8: *Effect of strain and particle concentration (vol.%) on the storage modulus of cleaned latex A at 25°C and frequency 2 Hz.* 84
Figure 5-9: *Effect of particle concentration on the storage modulus G', loss modulus G" and phase shift $\tan^{-1}$(G"/G') of cleaned latex A at 25°C and frequency 2 Hz.* 86
Figure 5-10: *Effect of strain and temperature on the storage and loss modulus of cleaned latex A at frequency 2 Hz.* 87
Figure 5-11: *Effect of temperature on the storage modulus G', loss modulus G" and phase shift $\tan^{-1}$(G"/G') of cleaned latex A at frequency 2 Hz and various particle concentration (vol. %).* 89
Figure 5-12: *Effect of strain and salt concentration on the storage modulus G' of latex A with ϕ=20.70 % at 25°C and frequency 2 Hz.* 91
Figure 5-13: *Effect of salt valency and concentration on the storage modulus G', loss modulus G" and phase shift $\tan^{-1}$(G"/G') of latex A with ϕ=20.70 % at 25°C and frequency 2 Hz.* 92
Figure 5-14: *The oscillation at frequency 2 Hz after steady shearing for 1 sec of cleaned latex A with ϕ=26.97 % at 15°C.* 94
Figure 5-15: *Effect of temperature and particle concentration on the stress relaxation and relaxation spectra of cleaned polystyrene latex A.* 96
Figure 5-16: *Plot of the experimental glassy modulus, Gg, against the* 101

calculated $G(\infty)/\psi_d^2$.

Figure 5-17: *Effect of salt concentration on the elastic modulus of latex A with ϕ=20.70% at 25°C; G' at 2 Hz: experimental storage modulus; $G(\infty)$, $G_o(\infty)$: theoretical high frequency limiting modulus calculated by using corrected and uncorrected Debye length, respectively.* 102

Figure 5-18: *Effect of salt valency on the elastic modulus of latex A with ϕ=20.70% at 25°C; G' at 2 Hz: experimental storage modulus; $G(\infty)$: theoretical high frequency limiting modulus.* 103

Figure 5-19: *Effect of temperature on the elastic modulus of cleaned latex A at various particle concentrations (vol. %); G' at 2 Hz; experimental storage modulus; $G(\infty)$: theoretical high frequency limiting modulus.* 104

Figure 5-20: *Effect of particle concentration on the elastic modulus of cleaned latex A at 25°C; G' at 2 Hz; experimental storage modulus; $G(\infty)$: theoretical high frequency limiting modulus.* 105

Figure 6-1: *The schematic representation of effective hard sphere concept.* 110

Figure 6-2: *Photographs of monodisperse latexes with ϕ=9.03% and electrolyte concentrations of 0, $1.0x10^{-5}$, $3.0x10^{-5}$ and $5.5x10^{-5}$M (from left to right) at 22 °C; the top and bottom photograph represents NaCl and $MgCl_2$ series, respectively.* 115

Figure 6-3: *Phase diagram demonstrating the effect of salt valency and concentration on the crystal fraction for latexes A with ϕ=9.03% at 22 °C.* 116

Figure 6-4: *Phase diagram showing order-disorder transition for latex A at 25 °C, as predicted by Kirkwood-Alder transition theory and by specifying effective hard sphere diameter in terms of the (a) uncorrected or (b) corrected Debye length.* 119

Figure 6-5: *Phase diagram as a function of temperature and particle volume fraction for cleaned latex A; the solid curve is a representation of equation (6.9) with A=4.0 and $\Delta C/Nk=3.9x10^4$ °K.* 121

Figure 6-6: *The order-disorder phase transition with respect to the change in particle concentration, temperature, salt valency and concentration, showing schematically in terms of the combined pair potential energies.* 123

Figure 7-1: *Schematic of the intaglio printing process.* 126

Figure 7-2: *Frequency sweeps for (a) storage and loss modulus and (b) phase shift.* 129

Figure 7-3: *The viscosity profile for model inks MB1A, MB2A, and MB3A.* 131

Figure 7-4: *The viscosity profile for model ink MB1E, MB1A, and MB1C.* 131

Figure 7-5: *The frequency sweep for dynamic modulus of model inks MB1A, MB2A, and MB3A.* 132
Figure 7-6: *The frequency sweep for dynamic modulus of model inks MB1E, MB1A and MB1C.* 133
Figure 7-7: *The frequency sweep for phase shift of model inks MB1A, MB2A, and MB3A.* 134
Figure 7-8: *Phase shift as a function of Deborah number, D_ϕ for model inks MB1A, MB2A, MB3A.* 135
Figure 7-9: *The frequency sweep for phase shift of model inks MB1E, MB1A and MB1C.* 136
Figure 7-10: *phase shift as a function of Deborah number, D_ϕ for model inks MB1E, MB1A and MB1C.* 137
Figure 7-11: *Ink transfer as a function of Deborah number D_v for model inks.* 139
Figure 7-12: *Ink transfer as a function of phase shift for the model inks printed with cylinders (1) and (3) and Prufbau impression material.* 140
Figure 7-13: *Slope of ink transfer/phase shift curve vs. ink depth in the engraving (μm).* 141
Figure 7-14: *Ink transfer vs. phase shift for the model inks MB1A and MB3A printed with engraved cylinders (1) and (3) and Prufbau (P) and BEP (B) impression materials.* 142
Figure 7-15: *Phase diagram as a function of strain and time for MB1A and BEP inks at 25 °C and 80 °C.* 143
Figure 7-16: *Frequency sweep measurements for dynamic modulus at different imposed strains for MB1A at 80 °C.* 144
Figure 7-17: *Phase shift as a function of temperature for MB1A and BEP inks, measured at strain equal to 0.03.* 145

List of Tables

Table 2-1: *Characteristics of polystyrene latex A.* 17

Table 4-1: *Effect of particle concentration on the estimated irradiation penetration in cleaned latexes A at 22 °C.* 58

Table 5-1: *Dimensional analysis on particle interactions.* 64

Table 6-1: *Correlation of [1-(R_e/R)] with β at various particle volume fractions ϕ; please refer to text for symbol designation.* 117

Table 7-1: *Model intaglio ink formulations.* 127

Table 7-2: *Engraving dimensions of Prufbau cylinder.* 128

Table 7-3: *Intaglio ink transfer data at various printing speeds on Prufbau using Portals paper with two engraved cylinders and Prufbau impression material.* 138

Abstract

Dow latexes A were fully characterized by transmission electron microscopy, conductometric titration and Fourier Transform Infrared spectroscopy. The uniformity of particles and well characterized particle surface justify the use of polystyrene latexes A as model colloids.

The zeta potential and Debye length is decreased with increasing either salt valency, salt concentration or temperature. The strength and range of electrostatic repulsion between particles are thus reduced based on the DLVO theory.

Based on the Bragg's law, the reflection spectrophotometric results indicate the crystal structure is of face-centered cubic type at high particle concentration. The lattice structure transition occurs with rising temperature, i.e. from fcc to bcc.

The rising viscosity with higher particle concentration or lower temperature can be explained qualitatively by the secondary electroviscous effect. Storage modulus decreases while phase shift increases with decreasing particle concentration, or increasing either temperature or salt concentration. The theoretical shear modulus ($G(\infty)$) of ordered latexes has been derived from the increase in electrostatic energy caused by a small shear strain to a structured dispersion. $G(\infty)$ calculated by using the "corrected" Debye length and a realistic stern potential derived from relaxation modulus, are in good agreement with the experimental data.

The order-disorder phase transition boundary constructed by results of optical and rheological study is compared with the prediction based on either effective hard sphere model and Kirkwood-Alder transition theory or thermodynamics. While the latter predicts rather well, the former

underestimates the transition at high salt concentration. The order-disorder phase transition, rigidity or even the dynamics of monodisperse latexes with respect to the change in particle concentration, temperature, salt valency and concentration can be well explained in terms of the combined magnitude of pair potential energies which the middle particle feels.

The rheological implications of ordered polymer colloids on printing were demonstrated by two examples in terms of the solid-liquid phase transition. One is the linear correlation of ink transfer with dynamic viscoelasticity of ink under given printing conditions. The other is the phase diagram of printing inks constructed as a function of strain level and printing time.

Chapter 1
GENERAL INTRODUCTION

A polymer latex colloid, a surfactant-stabilized colloidal dispersion of spherical polymer particles in a continuous medium, has found wide commercial applications in the printing, paper, paint, photographic , construction, and medical industries. When formed by emulsion polymerization, a typical synthetic latex is polydisperse (has a broad particle size distribution) and appears milky white. The first monodisperse latexes were of polystyrene and were produced by the Dow Chemical Co. in the early 1950's. Since then, uniform polymer latexes have attained considerable interest as a model system for the investigation of various colloidal phenomena. The simple spherical geometry and uniformity of the particles makes a direct comparison possible between experimental findings and theoretical calculations on interparticle forces based on DLVO theory (1). From a practical point of view, monodisperse latexes also serve a wide variety of uses (2) in (i) calibration standards in electron and optical microscopy (ii) medical diagnostic test for human pregnancy (iii) pore size determination of filter membrane (iv) investigation of the mechanism and kinetics of emulsion polymerization and latex film formation.

One of the remarkable features of monodisperse latexes is the iridescence due to Bragg diffraction of visible light from ordered arrays of particles (3). This ordering was found to be distroyed with the addition of excess salt (4), the reduction of particle concentration (5), or an increase in temperature (6). It is believed that each of the above factors suppresses the electrostatic repulsions localizing the particles within the lattice , allowing Brownian motion to collapse the structure. Although crystal-like structure (7-30) and order-disorder phase transition (31-55) of monodisperse latexes attained considerable scientific

attention , tremendous efforts were also made in studying the dynamics (56-60) and rheological (61-98) properties of ordered dispersion because of their relationship to ceramic precursor (40), biological macromolecules (99) , and surface coating (100, 101).

Research on ordered polymer colloids has been extensively reviewed by Efremov (102), Pieranski (103), Krieger (104), Rajagopalan and Hirtzel (105), van Megen and Snook (106). Although a great deal of work have been accomplished, some deficiencies still exist within these investigations. In spite of their importance, the electrokinetic potential or other relevant measure of the particle charge is rarely reported on the ordered dispersion system. Hachisu and coworkers (32) attempted to map out the isothermal phase diagram, showing order-disorder transition, by simple visual observation of iridescence, but failed to present the surface charge density of latex particle. It is apparent that a quantitative comparison between experiment and theory will only become feasible when the operational parameters are identified. While variables such as particle size, particle concentration and salt concentration were thoroughly investigated, important variables salt valency and temperature did not attract much of the attention. Therefore, the effect of counterion valency and temperature were neglected in Russel's work (70) on mechanical properties of ordered latexes and only limited temperature range was employed in optical diffraction study of dispersion crystal-like structure by Krieger (5). Moreover, tedious procedures of instrument set-up and calibration were frequently observed in the literature, new and convenient rheological and optical techniques have to be explored in order to study the structured dispersion.

The four variables of particle concentration, temperature, salt valency and salt concentration were investigated over a wide range in the present study in order to supplement previous reseach deficiencies and provide new insight on

ordered latexes. Complete characterization of the electrokinetic properties of the latex samples were included as part of this investigation. Rheological techniques by means of continuous forced oscillation and stress relaxation, which have been seldom used on ordered latexes, were employed and were found to yield useful and fruitful information of storage modulus G' , loss modulus G", phase shift $\tan^{-1}(G''/G')$, and relaxation spectra simultaneously. Reflection spectrophotometry was also applied to study the ordered structure of monodisperse latexes.

It is of theoretical interest to relate the microstructure and macroscopic rheological properties of dispersion to interparticle forces and thence to the effect of variables, such as particle concentration, temperature, salt valency and salt concentration. Although ordered polymer colloids have limited practical importance, they do provide an excellent model for the study of multiparticle electrostatic and hydrodynamic interactions. This dissertation represents a systematic effort and integrated approach to elucidate the interplay among colloidal forces, dispersion microstructure and resulting rheological properties of ordered polymer colloids and to investigate the order-disorder phase transition behavior of monodisperse latex. The experimental approach designed to achieve the above reseach objectives is shown schematically in Figure 1-1.

An analogy for solid-liquid phase transition was also sought for printing ink type systems. Two examples will be shown in order to demonstrate the impact made by the understanding of condition-driven phase transition. One is the correlation of ink transfer with ink rheology under given printing conditions. The other is the phase diagram of printing inks. The former has been one of the long lasting goals in printing ink research.

This dissertation begins with the reseach results on complete characterizations of model polystyrene colloids in Chapter 2 with respect to the

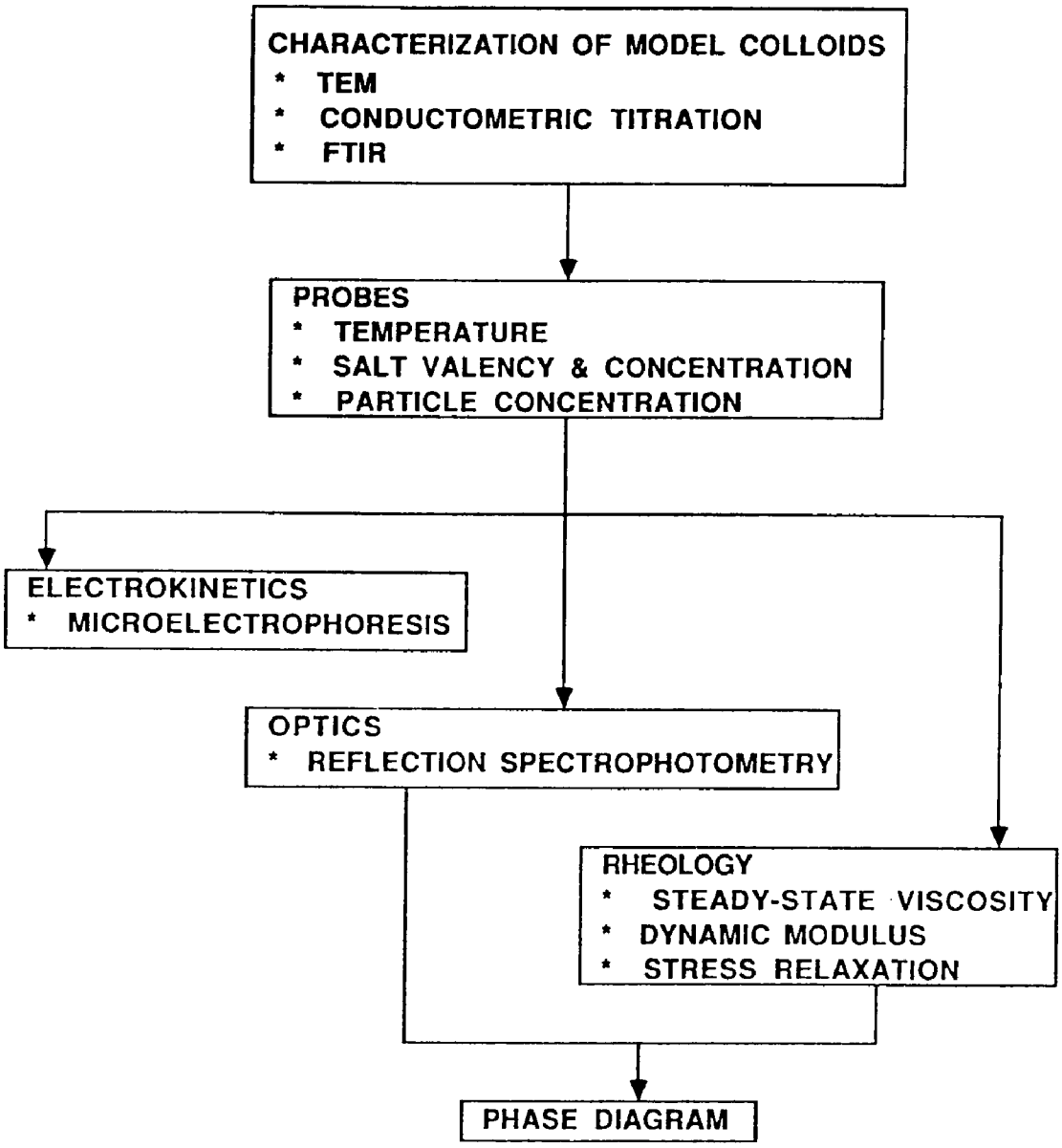

Figure 1-1: *Experimental research program of ordered polymer colloids.*

particle size and the nature and concentration of functional groups on the particle surface. Chapter 3 investigates particle-particle interaction as a

function of electrical double layer properties according to DLVO theory. These results will be used to interprete the optical and rheological properties of the ordered latex systems as a function of the operational parameters. Chapter 4 displays how the crystal-like dispersion microstructure can be probed and established by the technique of reflection spectrophotometry and the principle of Bragg's diffraction. The flow and viscoelastic properties of ordered dispersion are presented in Chapter 5 where the experimental elastic moduli are compared with predictions calculated from a crystal lattice model and pairwise additive theory. Chapter 6 discusses the order-disorder phase transition of monodisperse latexes. The phase boundary constructed by previous optical and rheological study is compared with the prediction based on either effective hard sphere model and Kirkwood-Alder transition theory (107) or thermodynamics (6). Chapter 7 demonstrates how the concept of solid liquid phase transition places an impact on the understanding of printing performances. Finally, this dissertation finishes with conclusions in Chapter 8. The above progression reflects the author's strong belief that macroscopic observables can be related directly to microscopic characteristics.

Chapter 2
CHARACTERIZATIONS OF MODEL COLLOIDS

2.1 INTRODUCTION

Model colloids are defined as stable dispersions of rigid, monodisperse spherical particles of constant surface charge (108). The particle size distribution has to be established in order to ensure the particle uniformity. The surface of model colloids must also be well characterized regarding the nature, concentration, and distribution of functional groups. The determination of these parameters involves two stages: the removal of electrolytes, oligomers and excess emulsifier from the latex and the subsequent analysis of surface groups. In this work, transmission electron microscopy, conductometric titration and infrared spectroscopy were used to establish the particle size distribution, the concentration and nature of particle surface groups ,respectively. Brief review on making monodisperse latexes, latex cleaning, particle surface groups and surface charaterization is presented in the following paragraphs.

Monodisperse polystyrene latexes have been popular in recent years as model dispersions for the study of a number of fundamental colloidal phenomena. Wachtel and La Mer (110) have used the term monodisperse to describe sols having a coefficient of variation in the particle diameter range of < 10 %. The use of emulsion polymerization to prepare polystyrene latexes in which the particles have a very narrow size distribution is well known, particularly as a consequence of the pioneer work of Vanderhoff and his collaborators (109). Emulsion polymerization comprises the emulsification of an immiscible monomer in a continuous medium followed by polymerization with a

free radical initiator. The many mechanisms proposed for the initiation of polymer particles can be divided into four main categories according to the locus of particle nucleation: (i) monomer-swollen micelles; (ii) aqueous phase; (iii) adsorbed emulsifier layer; (iv) monomer droplets. The details of emulsion polymerization mechanisms have been presented elsewhere (111).

In order to obtain monodisperse latexes, the duration of the particle nucleation stage has to be maintained short relative to that of the particle growth stage. If the particle nucleation stage lasts 4 hours and the particle growth stage 10 hours, the particle lifetimes would range from 600 to 840 min. If the particle volumes were proportional to the particle lifetimes, the largest particle would have a diameter 12 % greater than that of the smallest particle. If th particle nucleation stage lasts only 15 min, however, with the same particle growth stage, the largest particle would have a diameter only 0.8 % greater than that of the smallest particle, and the particle size distribution would be extremely narrow. The methods and factors used to control particle size in the formation of polymer latexes have been investigated (112).

It had been established that the free radicals from the decomposition of the initiator form end groups on the polymer chains of latexes, and that these end groups are acidic and offer the means of rendering the particle colloidally stable (112). Hence, it is worthwhile to present the three major kinetic steps, i.e. initiation, propagation and termination, which are involved in a typical radical chain polymerization. An initiator (I) initially undergoes homolytic dissociation to produce two free radicals:

$$I \rightarrow 2R\bullet$$

These free radicals then react with monomer (M) to form a polymeric radical as follows:

$$R\bullet + M \rightarrow RM\bullet$$

and propagation takes place by the growth of polymeric radicals through the successive addition of large numbers of monomer molecules according to:

$$RM\bullet + nM \rightarrow R(M)nM\bullet$$

Competing with the reaction of polymeric radicals with monomer are various termination reactions:

(i) combination:

$$R(M)nM\bullet + R(M)mM\bullet \rightarrow R(M)nMM(M)mR$$

(ii) disproportionation:

$$R(M)nM\bullet + R(M)mM\bullet \rightarrow R(M)nM' + R(M)mM''$$

(iii) termination with primary radicals (R•):

$$R(M)nM\bullet + R\bullet \rightarrow R(M)nMR$$

(iv) termination by chain transfer to monomer (M), initiator (I), or polymer (P) is also possible:

$$R(M)nM\bullet + M(I \text{ or } P) \rightarrow R(M)nM' + M\bullet(I\bullet \text{ or } P\bullet)$$

"Cleaning" of a latex is a process which is used to remove part or all of the electrolytes, oligomers and emulsifiers in the system. An extensive review of cleaning methods and experimental techniques for qualitative and quantitative characterization of surface groups has been presented by El-Aasser (113). Latexes are usually cleaned by dialysis or ion exchange technique. Dialysis is slow and removes only part of emulsifiers. Ion exchange is rapid but requires tedious purification of the commercial ion exchange resins which contain leachable polyelectrolytes that adsorb on the surfaces of polystyrene latex particle. The third technique to clean latexes is the serum replacement. The latex is placed in a stirred cylindrical cell, and distilled, deionized water is forced by gravity through the latex while the particles are confined with a nuclepore filtration membrane. This washing with water removes the adsorbed emulsifier from the latex particle surface and solute electrolyte and emulsifier from the aqueous phase, but does not replace Na^+ and K^+ counterions with H^+ ion. Further washing with diluted hydrochloric acid ($5x10^{-4}$ N), followed by

water to remove excess acid, replaces the counterions with H^+ ions completely. This method is simple and efficient, and gives surface charges results in good agreement with ion exchange.

The chemically bound groups on the surface of latex particles may be polymer end groups, reaction products of these end groups, and incorporation of monomers containing functional groups. The surface groups most commonly encountered for polystyrene latex are sulfate, hydroxyl, and carboxyl. Sulfate groups arise from persulfate initiator fragments covalently bonded at the end of polymer chains. Hydroxyl groups can result from the use of hydrogen peroxide initiator or the hydrolysis of sulfate groups. Carboxyl groups originate from the oxidation of hydroxyl groups.

Much of the controversy about the absence or presence of surface carboxyl groups on polystyrene latexes has appeared in the literature. This ambiguity is further amplified by the relative effectiveness of the latex cleaning methods and surface characterization techniques used by different authors. Ottewill and Shaw (114) found the presence of weak acid group on latexes made using both hydrogen peroxide and persulfate initiators in the presence of different kinds of emulsifiers by employing the dialysis purification and electrophoresis technique. However, Wu (115) produced polystyrene latexes in an oxygen-free medium that carried only sulfate surface groups. Wu reported that the weak acid group can be introduced deliberately upon the addition of oxidizing catalysts, such as heavy metal ion Ag^+. Stone-Masui and Watillon (116), using ion exchange resins to clean latexes, demonstrated that the emulsifier used may affect the type of surface groups produced.

The surface charge of polymer latexes is generally characterized by conductometric and potentiometric titrations as well as by electrophoretic

mobility measurements (117). However, as these quantitative techniques are not specific to a particular surface group, the qualitative interpretation is sometimes ambiguous and requires other surface charge analyses, such as X-ray photoelectron spectroscopy (XPS) and infrared spectroscopy (118).

2.2 EXPERIMENTAL

2.2.1 Materials

Dow polystyrene latexes (Dow Chemical Company, Midland, Michigan) were used in this study and designated latex A. The water used for the latex cleaning and for dispersion preparation was distilled and deionized by Milli-Q water system.

2.2.2 Latex Cleaning by Serum Replacement

A filtration cell with a capacity 400 ml (Micro Filtration Systems, Dublin, CA) was used to replace the latex serum with distilled, deionized water. The cell consists of a cylindrical polycarbonate reservoir held between two polyacetal plates. A polycarbonate filtration membrane with uniform pore size 0.2 μm and diameter 76 mm (Nucleopore Corp., Pleasanton, CA) is supported by a porous polyethylene disk at the bottom of the cell. A Teflon-coated stirring bar rotates close to the membrane surface to prevent clogging of the membrane by the latex particles and to give a steady flow rate over long periods of time. Distilled and deionized water is fed from a reservoir positioned above the cell (to adjust the pressure head), and diluted serum or filtrate was collected from the bottom. The filtration rate depends on the latex concentration, the pressure head applied by the water reservoir and membrane porosity. Cleaning 4 % solids latex with a pressure head of about 2 psi gave satisfactory results. The latex was washed with water until the conductance of the filtrate was about the same

as that of the feed water. The latex was further washed with 3 liters of $5x10^{-4}$ N hydrochloric acid to replace the Na^+ and K^+ ions with H^+ ions. The latex was subsequently washed with water until the desired conductivity, measured by General Radio Impedance Bridge, was obtained. The monodisperse latexes displayed the characteristic iridescence after about 10 days of complete cleaning cycle.

2.2.3 Particle Size Determination by Transmission Electron Microscopy

Phillips EM-300 was used to obtain the transimission electron micrographs of latex particles. The magnification of the instrument was calibrated by a grating replica. One drop of diluted latex dispersion was placed on the stainless steel grid (200 mesh) coated with polyvinyl formvar film and carbon. The grid was then allowed to dry in dust-free environment at room temperature. The grids were then examined by transmission electron microscopy, and photographs were taken.

The electron micrograph negatives were printed and enlarged. Approximately 400 particles were measured on a Zeiss MOP3 image analyzer in order to obtain the particle size distribution. The data thus obtained were analyzed by computer to determine the number average diameter and standard deviation of the latex particles.

2.2.4 Conductometric Titration

After serum replacement, the cleaned latex was weighed into the titration beaker, diluted by distilled deionized water, and then sparged with nitrogen for 20 minutes. The latex was then titrated conductometrically under a nitrogen blanket (avoid reentry of CO_2) with 0.02 N standard sodium hydroxide solution added continuously at a rate of 1 cc/min under continuous stirring. The

conductance was measured by a conductivity meter and recorded continuously. These measurements were calibrated using standard electrolyte solutions to obtain absolute values of the conductance. The tip of the constant-flow-rate titrant burette was positioned just under the surface of the latex to obtain a smooth, precise conductometric titration curve.

Surface charge density (σ) was calculated from the conductometric endpoint, which can be determined by extrapolating the linear legs of the titration curve and locating the intersections, according to the following equation :

$$\sigma = \frac{Fn\rho a}{3W} \tag{2.1}$$

where F is the Faraday constant (96487 coul/mole), n is the number of moles of NaOH taken up by the particles, ρ is the density of polystyrene latex particles (1.054 g/cm^3), a is the radius of latex particles, and W is the total solid content of latex (g).

2.2.5 Fourier Transform Infrared Spectroscopy

Samples of the purified latexes were examined with a Sirius 100 FTIR Spectrometer (Mattson Instrument, U.S.A.). Transmittance was recorded as a function of wave number. Spectra were obtained on the solid polymer in the form of a thin film. The film was made by casting a solution of freeze-dried latex in carbon tetrachloride onto the rock salt window and removing the solvent in *vacuo*.

A pure polymeric film (Analect Instrument-IR standard) designated as standard polystyrene was used in order to establish a standard in spectra band assignments. The spectrum of this standard sample did not display any bands which could be attributed to surface functional groups.

2.3 RESULTS AND DISCUSSION

Figure 2-1 shows the transmission electron micrograph of polystyrene latex A. Image analysis and computer calculation indicated that latex particle has number average diameter 233 nm with standard deviation 14 nm and polydispersity index 1.01. In view of the small coefficient of variation on the mean particle diameter, the particle size distribution was considered to be monodisperse.

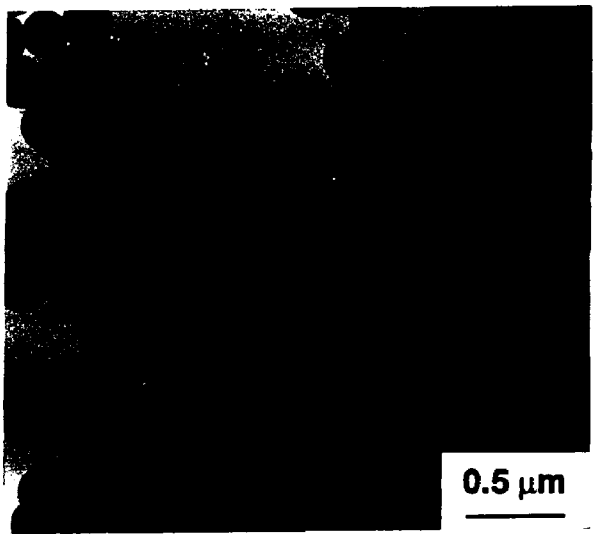

Figure 2-1: *TEM micrograph of latex A.*

It is known that the conductivity of a solution of an acid or a base is determined by its concentration and extent of ionization. Thus, the shape of the titration curve between an acid and a base depends on the dissociation constant of the acid and the base. Conductometric titration of cleaned latex A in H^+ form is shown in Figure 2-2. The two inflection points observed in the titration curve indicate the coexistence of strong and weak acidic group on the particle surface. In the first stage of neutralization, the stronger acid HA will suppress the ionization of the weaker acid HB, so that the initial part of the titration curve is

entirely due to the neutralization between the NaOH and the stronger acid HA. At this stage, the conductivity of diluted dispersion is reduced upon progressive addition of NaOH because of the decreasing concentration of highly mobile H^+ and increasing concentration of less mobile Na^+. When all the H^+ dissociated from stronger acid HA are replaced and the neutralization is complete, the conductivity will reach its minimum. The rounding near endpoint is due to slow attainment of equilibrium near equivalence point. Thereafter, neutralization of weaker acid with NaOH comes into play. Less dissociated H^+ from weaker acid HB is neutralized and at the same time the conductivity climbs up owing to the formation of B^-, Na^+ and already existed A^-. The end point is reached as the neutralization is complete. Beyond this point, the addition of NaOH further increases the conductivity and the slope of titration curve, but does not result in a sharp inflection. Surface charge density can then be calculated from equation (2.1) by knowing the amount of NaOH consumed by each acidic group. Table 2-1 summarizes the results of surface charge density and particle size distribution of latex A.

Conductometric titration offers quantitative surface characterization concerning the concentration and acidic strength of surface groups. Furthermore, the discrepancy about the presence or absence of weak acidic group on particle surface still exists in literature as was discussed in Introduction. The infrared spectrum study is required to further identify the nature of surface functional groups, confirm the latex chemical composition and provide additional evidence for the existence of weak acidic surface group on latex particles.

Comparison of the IR spectra between the (a) standard and (b) latex A in Figure 2-3, show that very weak but significant absorptions at 1200, 1230 1300 cm^{-1} in (b) were found and attributed to the vibrations of surface sulfate group

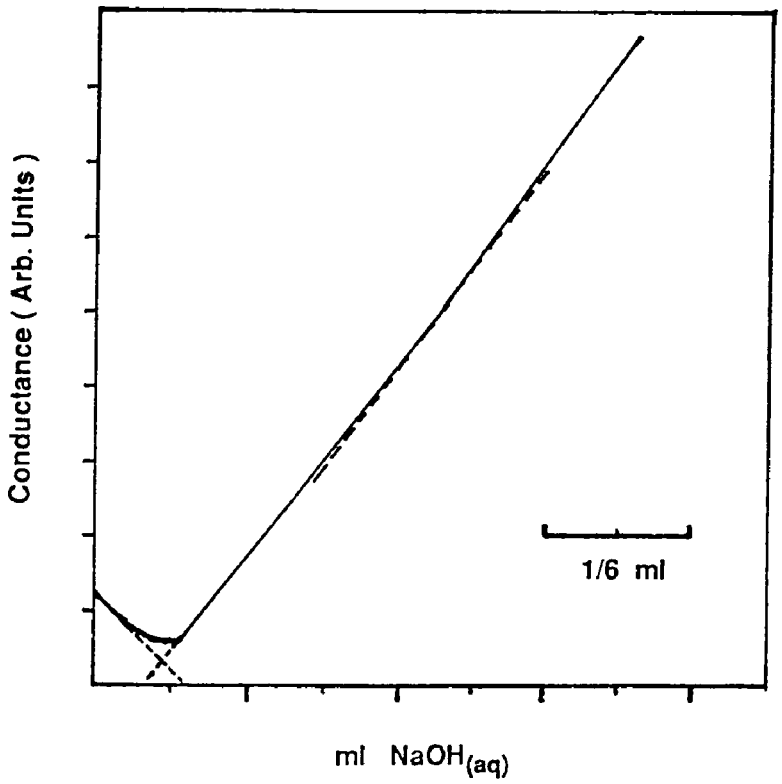

Figure 2-2: *Conductometric titration of cleaned latex A (0.2474 g solids in 60 g dispersion) with 0.02 N NaOH(aq).*

Table 2-1: *Characteristics of polystyrene latex A.*

Diameter	233	nm
Standard Deviation	14	nm
Surface Charge Density		
Strong Acidic Group	2.46	$\mu coul/cm^2$
Weak Acidic Group	9.70	$\mu coul/cm^2$

(119). This is expected since latex A was synthesized by the $K_2S_2O_8$ initiated emulsion polymerization process. The absorption frequency shift from 1675 in (a) to 1657 cm^{-1} in (b) ascribed to the carbonyl group vibrations provides complementary support to the observation of the extra absorption band at 1770

cm^{-1} in (b). The later absorption has been assigned to the C=O stretching of phenylacetic acid (120). The absorption at 3590-3650 cm^{-1} in (b) is considered to be free OH stretching. Based on the above discussions, it is strongly suggested that the latex particle contains both strong (sulfate) and weak (carboxyl) surface acidic groups, and possibly hydroxyl groups. The origins of these surface groups have been discussed in Introduction.

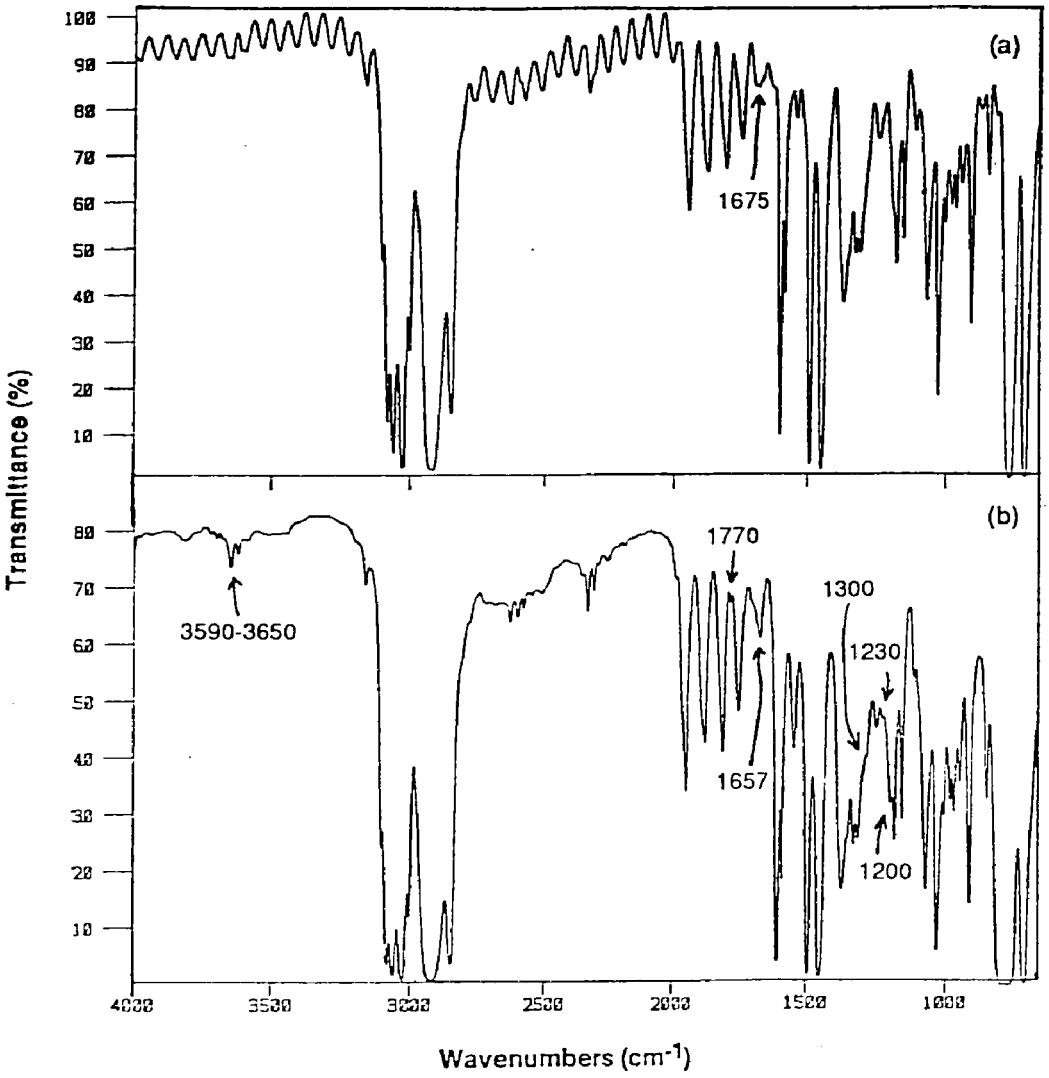

Figure 2-3: *Infrared spectra of (a) standard polystyrene sample (b) latex A.*

Chapter 3
INVESTIGATIONS OF PARTICLE INTERACTIONS

3.1 INTRODUCTION

Based on the Derjaguin-Landau-Verwey-Overbeek theory (DLVO theory) of colloidal stability (1), the interparticle interaction consists of electrostatic repulsion and van der Waals attraction. In the ordered latex system, the short range attractive van der Walls force can be neglected (31) when compared with the electrostatic repulsion due to overlay of electrical double layers. The important properties of the electrical double layer that are experimentally available are the zeta potential and the thickness of double layer. Unfortunately, the electrokinetic potential or other relevant measure of the particle charge is rarely reported on the ordered dispersion system. In the present study, the electrophoretic mobility and the corresponding zeta potential of model latexes were obtained under various conditions of temperature, pH, salt valency and salt concentration. The zeta potential and thickness of the electrical double layer control the strength and range of electrostatic repulsion between particles. An understanding concerning the magnitude and range of repulsion forces under given conditions is necessary to interprete the optical and rheological properties of model dispersions which will be discussed in Chapter 4 and 5. The latex charging mechanism, electrical double layer model, DLVO theory and the conversion between electrophoretic mobility and zeta potential will be briefly examined below.

The basic principle behind the electrostatic stabilization of any colloidal system is the acquisition of charges at the surface of the particles. The origin of electrical charge might be a single mechanism or a combination of more than

one mechanism as given below.

(i) Ionization

The ionogenic groups on particle surface can dissociate and give rise to surface charge.

(ii) Adsorption of Ionized Surfactants

Particles can become positively or negatively charged by adsorption of cationic and anionic surfactants.

(iii) Adsorption of Potential-Determining-Ions

A silver iodide particle adsorbs an excess of Ag^+ or I^-, depending on their relative concentration in the equilibrium solution.

(iv) Preferential Adsorption of Ions

OH^- from aqueous phase are preferentially adsorbed on non-ionogenic colloidal particles because of the ion-induced dipole interaction (121).

(v) Contact Electrification

Based on the electron injection concept for two phases in contact, the material with lower dielectric constant will acquire a negative charge (121). Hence, O/W emulsion droplet will be mostly negatively charged.

Charged colloidal particles are surrounded by a diffuse layer of counter ions of equal but opposite charge. The schematic representation of the structure of the electrical double layer is illustrated in Figure 3-1. It is assumed that this double layer can be treated by the classical Gouy-Chapman theory or a modified one proposed by Stern (122).

The thickness of the double layer or Debye length $1/\kappa_o$ is given as

$$[a\kappa_o]^2 = \frac{a^2 e^2 (\Sigma n_{io} Z_i^2)}{\varepsilon_o D k T} \tag{3.1}$$

where a is the particle radius, e, the electronic charge, D, the dielectric constant of continuous medium (78.54 for water at 25 °C), ε_o, the permittivity of free

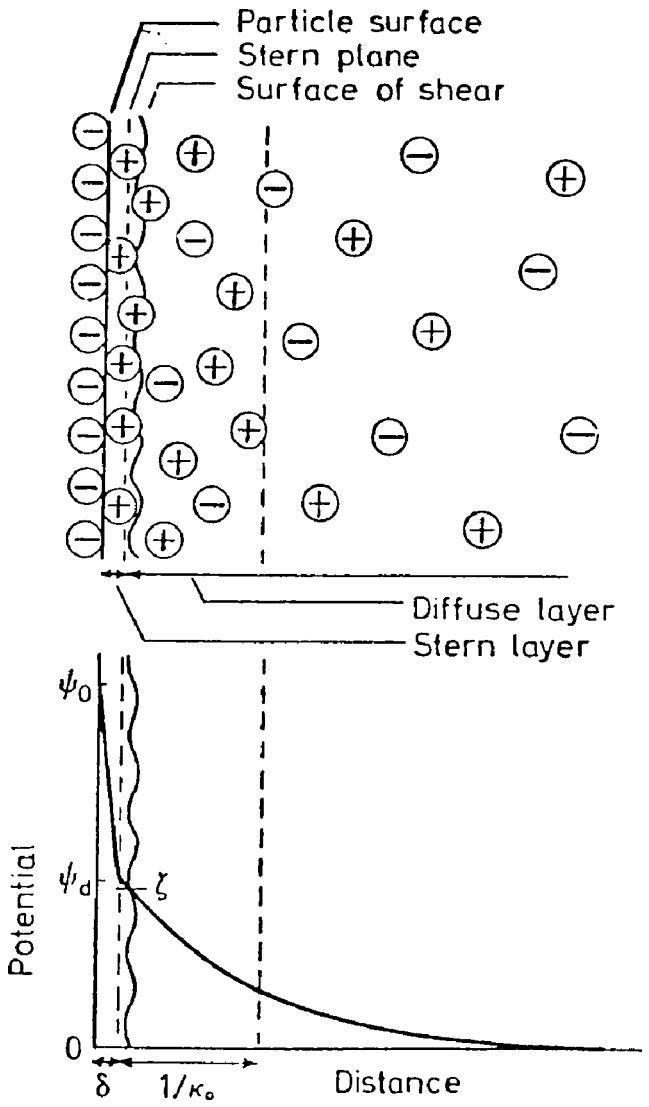

Figure 3-1: *Schematic representation of the structure of the electrical double layer.*

space (8.854 x 10^{-12} coul/volt m), k, Boltzmann's constant (1.38 x10^{-16} erg/molecule °K), T, the absolute temperature (°K), n_{io}, the ion concentration in the bulk of the solution (mole/l) and Z_i, the ion valency.

The surface charge of particle gives rise to an electrostatic potential (ψ_o) which exists at the surface relative to a point in the bulk of the solution.

Another Stern potential (ψ_d) exists at the diffuse double layer, which is positioned at a distance δ from the interface. This Stern plane is caused by the specific ion adsorption. None of these two potentials could be measured experimentally and their precise relations to the measurable zeta potential ζ located at a shear plane outside the stern layer is unknown. The zeta potential is usually taken as a good approximation of the potential change across the diffuse double layer.

The determinant of colloidal stability against coagulation is the balance between the electrostatic repulsion (V_R) due to overlap of the electrical double layers, and the van der Waals attraction (V_A) because of electromagnetic fluctuations. These two major contributions compose the total potential energy of interaction between a pair of particles. As suggested by DLVO theory (1), these two contributions can be added to give the total energy of interaction (V_T), as follows:

$$V_T = V_R + V_A \tag{3.2}$$

For spherical particles of radius a, with center-to-center separation distance R and constant stern potential ψ_d<50 mv, then (123)

$$V_R = \frac{4\pi a^2 D\varepsilon_o \psi_d^2 \, exp[-\kappa_o(R-2a)]}{R} \qquad ,for\ \kappa_o a<3 \tag{3.3}$$

$$V_R = 2\pi a D\varepsilon_o \psi_d^2 \, ln\{1+exp[-\kappa_o(R-2a)]\} \qquad ,for\ \kappa_o a>10 \tag{3.4}$$

The potential energy of attraction between two spheres in a liquid medium is given by (123)

$$V_A = -\frac{A_{121}}{6}\left[\frac{2}{S^2-4} + \frac{2}{S^2} + ln\left(1-\frac{4}{S^2}\right)\right] \tag{3.5}$$

where S=R/a and A_{121} is the composite Hamaker constant for polystyrene in water.

The schematic total pair potential energy curve is shown in Figure 3-2. At short distances, a deep minimum in potential energy occurs. This primary

minimum arises from the Born repulsion between adjoining electron clouds. At intermediate distances, the electrostatic repulsion makes the largest contribution and therefore a primary maximum (Vm) occurs. At larger distances, the exponential decay of the electrical double layer causes this term to fall of more rapidly than the inverse power law of the attractive term and another secondary minimum (Vs).

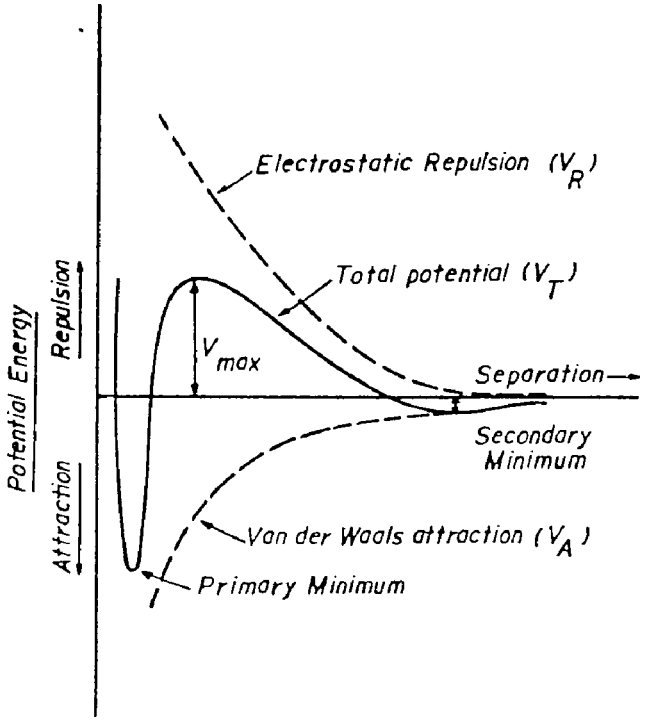

Figure 3-2: *The schematic diagram of total potential energy between a pair of particles.*

The potental energy barrier discourages the particle contact so that entering the deep energy well, causing irreversible coagulation, is avoided. Since the barrier is of only limited extent, the stabilizing effect is kinetic and not thermodynamic in origin. The shape of the curve and the height of primary maximum depend on all of the parameters that affect V_A and V_R. If the secondary minimum is deep enough, approximately 5 kT or greater, a weak

flocculation is possible. This phenomenon is not usually observed with smaller particles because the energy well is comparable to the mean thermal energy and flocculation is easily reversed by Brownian motion.

The most common experimental method for evaluating the sign and magnitude of charge of the electrical double layer at particle surface is electrophoresis, which involves the measurement of particle velocity in an electric field. Electrophoresis theory (124, 125) takes into account the particle charge and field strength, the frictional drag on the particles, the electrophoretic retardation due to the backward flow of the solvent, and the relaxation effect due to distortion of the ionic atmosphere surrounding the particle and build-up of opposing electric field for particle movement.

The calculation of zeta potential (ζ) from measured electrophoretic mobility (U) requires a theoretical relation between the two quantities. Without the complication of relaxation and retardation effect, Smoluchowski and Huckel (122) independently derived two limiting relationships.

$$u = \frac{v}{E} = \frac{(4\pi\varepsilon_o D)\zeta}{4\pi\eta} \quad , for\ a\kappa_o > 100 \tag{3.6}$$

$$u = \frac{v}{E} = \frac{(4\pi\varepsilon_o D)\zeta}{6\pi\eta} \quad , for\ a\kappa_o < 0.1 \tag{3.7}$$

where u is the electrophoretic mobility, v is particle velocity, E, the electric field gradient, η, the solvent viscosity. Henry (122) showed that if correct allowance was made for retardation effect, the relationship between u and ζ for spherical particles depended on particle radius and Debye length. Overbeek (126) derived analytical expressions for the mobility, which included corrections for retardation and relaxation in terms of an incomplete power series in zeta potential. The coefficients of these analytical expressions are functions of $\kappa_0 a$. The limitation of these latter expressions was that they were only valid for zeta potentials less than 25 mV. More recently, Wiersema (124) have obtained a

numerical solution of the problem, which gives the mobility as a complete power series in zeta potential, valid for potentials greater than 25 mV. O'Brien and White (125) described the numerical computations of reduced mobility as a function of reduced zeta potential for various $\kappa_0 a$ values, all for 1-1 electrolyte of equivalent conductance corresponding to KCl at 25 °C. Curves of this format are often the most convenient for experimental study of a given sol. Moveover, they claimed their computation is free of the convergence difficulties which hampered Wiersema, and consequently the results are applicable over a wider range of zeta potentials

A number of experimental or theoretical studies on the electrokinetic properties of colloidal systems have been carried out for diluted (117, 127-135, 140-142) dispersions by microelectrophoresis or concentrated (136-139) dispersions by electro-acoustic technique (139). The effect of latex particle concentration on the electrophoretic mobility was not pursued in the present study. Further investigation is thus needed in order to elucidate the impact of particle concentration on the interparticle force.

3.2 EXPERIMENTAL

3.2.1 Materials

The analytical grade (Fisher Scientific) of the following chemicals were used as received: NaCl, $MgCl_2$, $AlCl_3$, $NaOH_{(aq)}$, $HCl_{(aq)}$. Solutions and suspensions were prepared using distilled deionized water. pH, measured by pH meter (Orion Model 701 A), was adjusted by the addition of acid or alkali in electrophoretic study.

3.2.2 Microelectrophoresis

The electrophoretic mobilities of model latex were measured directly by Pen Kem System 3000 (Pen Kem Inc.), at infinite dilution for a range of pH, temperature and salt concentrations. Latex concentration for mobility studies were in the range of 0.0005-0.001 % w/w (by weight). For each sample the reported mobility represents an average of 5 measurements.

The Pen Kem 3000 is a computer controlled, automated instrument. It employs a novel electrophoresis chamber well suited to automated cleaning and maintenance--a single piece of precision-formed silica tubing with two slightly enlarged portions having palladium electrodes permanently bonded to the silica surface.

The chamber is mounted horizontally in a thermostatically-controlled water bath. A vertically mounted 2 mW helium-neon laser and associated optics provide a curtain of laser light which illuminates only the particles at the focal plane of a computer-controlled microscope system. An image of these illuminated particles is projected onto the surface of a rotating glass disk containing a precision radial grating. The movement of the particle image with respect to this grating causes a fluctuation in the intensity of the transmitted light which is then converted to an electrical signal by a suitable detector.

If an electric current is applied between the electrodes, the particles move electrophoretically-negatively charged particles toward the anode, positive ones to the cathode. If the image of a given particle moves in the same direction as the grating, it crosses few line-pairs per unit time. Thus the signal for that particles will be at a lower frequency than the signal from the reference detector which senses the movement of the grating alone. Conversely, if the image moves in the opposite direction, the signal will be at a slightly higher frequency compared to the reference. Typically, many particles are measured

simultaneously, each particle contributing a signal at a frequency shift determined by its electrophoretic velocity.

A Fast Fourier Transform Analyzer (FFT) computes a frequency spectrum from this doppler signal and then averages successive spectra to obtain the electrophoretic distribution function. The relationship between the particle velocity and the observed frequency shift depends only on the microscope magnification and the periodicity of the grating, both of which can be determined with great accuracy.

Electrophoretic migrations are always superimposed on other displacements which must either be eliminated or corrected to give accurate values for mobility. Examples of these other kinds of movement are Brownian motion, sedimentation, convection and electro-osmotic flow. Brownian motion, being random, is eliminated by averaging a series of individual observations in Pen Kem 3000. Convection may be minimized by effective thermostating. Sedimentation of the particles does not produce an error in the mobility determination since this motion is along the radial direction of the grating in system 3000. At 70.7 % of the radial distance from the center of the capillary lies a circular surface of zero liquid flow. Any particle tracked at this position in the capillary will display its mobility uncomplicated by the effects of electro-osmosis.

3.3 RESULTS AND DISCUSSION

Figure 3-3 shows the effect of pH on the electrophoretic mobility of latex A at various NaCl concentration. The general patterns were essentially identical for latexes at three different NaCl concentrations. At low pH, the latex particle adsorbed enough protons or Na^+ ions to undergo charge reversal, the trend being stronger for samples with higher NaCl concentration, since the isoelectric

point increases with increasing solution NaCl concentration. With further increasing pH, particle mobility increases due to the dissociation of surface acidic groups. At intermediate pH ranges ca. 5-9, the mobility reaches a plateau where complete ionization occurs. Also, the number of added ions was too small to cause any appreciable changes in mobility within this pH range. At higher pH, the mobility climbs up to a maximum followed by a rapid decrease. The increase was attributed to the preferential adsorption of OH^- on latex particle. The final decrease of mobility at higher ionic concentrations was found to be similar to that at extremely low pH. At this stage, more distorted counterions cloud sets up a higher electric field which opposes the particle movement. In addition, the ions distort more rigorously the velocity field of the liquid around the particle, for the ions drag liquid with them as they move. As a result the electrolyte ions decrease the electrical force and increase the viscous drag on the particle. Therefore electrophoretic mobility is greatly reduced.

The effect of salt valency and salt concentration on the electrophoretic mobility of latex A is illustrated in Figure 3-4. In the case of NaCl and $MgCl_2$, it is shown that there is a gradual decrease in mobility up to a salt concentration of 10^{-4} M, after which the mobility increases to a maximum at about 10^{-2} M followed by a dramatic decrease. The initial decrease was attributed to the decreasing ionization potential of surface groups with increasing concentration of counterions, because counterions might interact specifically with the surface groups. The maximum was believed to result from the preferential adsorption of coions (Cl^-) on the hydrophobic parts of the particle surface. This can be explained by the fact that anions, which are less hydrated than cations, are more surface active on apolar surfaces. Also, the acidic functional groups may not prevent the coions from approaching close to the surface if they are spaced far apart from each other. The final decrease in the mobility curve was

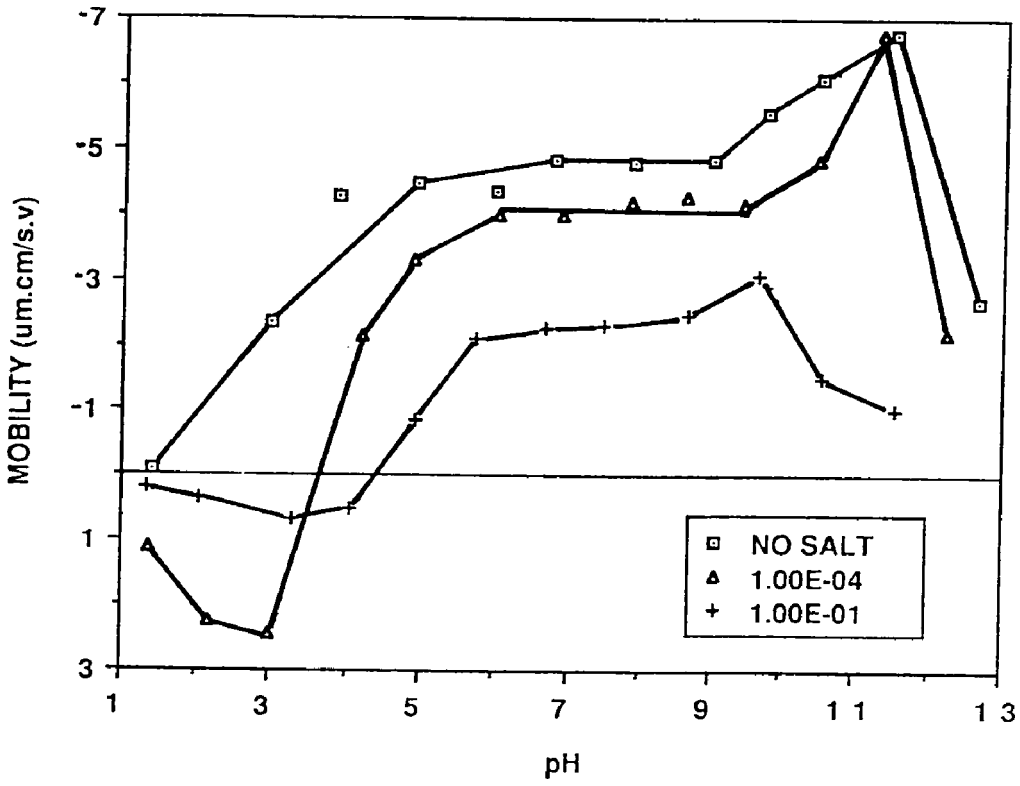

Figure 3-3: *Electrophoretic mobility vs pH for latex A at various NaCl concentrations (mole/l) at 25 °C.*

associated with the compression of diffuse double layer and the charge neutralization.

The difference between the mobility curves with 1:1 electrolyte as compared to 2:1 electrolytes is ascribed to the fact that the counterions of higher valency are more effective in reducing the negative electrokinetic potential of the particles as compared to monovalent counterions. As a result of charging mechanim of coions adsorptions, the steeper slope of the ascending leg of the mobility curve and the higher value of mobility at maximum were observed for samples containing lower valency salt.

In the case of $AlCl_3$, electrophoretic mobility drops catastrophically from 10^{-6} to 10^{-5} M and remains close to zero with further addition of salt

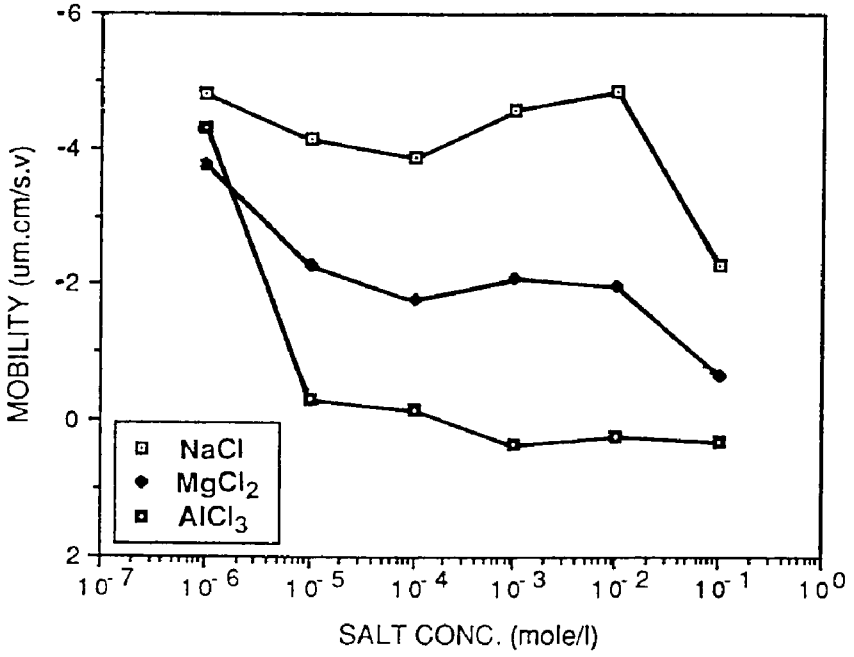

Figure 3-4: *Electrophoretic mobility as a function of salt valency and salt concentration for latex A at 25 °C.*

concentration. Matijevic (143) reported that the effect of aluminum salt on the aqueous colloidal stability is not fully described unless the possibility of complex ion formation in the solution is taken into account. At low pH, the counterion is Al^{3+}; as the pH is increased the counterions are higher order complexes formed by hydrolysis, such as $Al_8(OH)_{20}^{+4}$. Complex ion in the medium have two major effects: they change the ionic strength of the medium, and they can change the particle charge by adsorption. Because of their higher valency, these complexes are more effective coagulants. In the present study, pH of sample solutions is around 5.5 which tends to cause the complex ion formation and particles coagulate even at low aluminum salt concentration. As a consequence, the velocity of the massive particle aggregates in an electric field becomes essentially zero. The effect of salt $AlCl_3$ on the dispersion properties was not further investigated because of the complications discussed above.

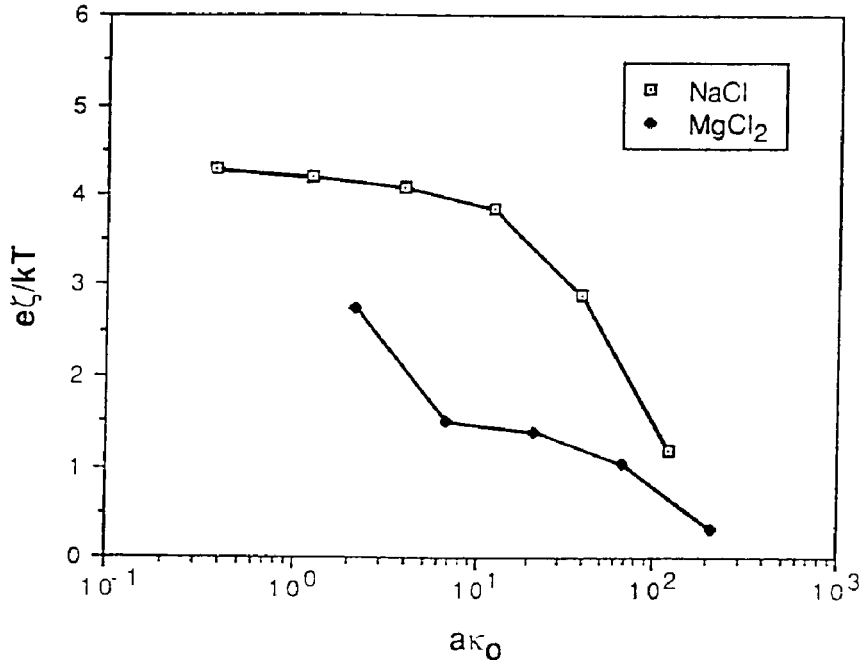

Figure 3-5: *Dimensionless zeta potential vs. $a\kappa_o$ for latex A in various aqueous salt solutions at 25 °C.*

The results in Figure 3-3 and 3-4 support the concept of a dual charging mechanism for polymer latexes (131). One mechanism is controlled by the ionization of surface groups. The other mechanism is controlled by the nature of the bare polymer surface which preferentially adsorbs coions. The former mechanism dominates when particles carry high concentration of surface functional groups. The above model has been successfully used to interprete the mobility maximum observed in Figure 3-4. Another qualitative explanation which has become popular recently is the hairy layer model (132-134). In this model, the surface of polymer latexes is comprised of polyelectrolyte chains carrying the surface charge. This layer expands upon decreasing the ionic strength due to repulsion of the functional groups, and contracts with increasing ionic strength. The expansion and contraction of the hairy layer affects the location of shear plane and consequently the electrokinetic potential. While this

model is capable of explaining qualitatively some of the mobility results, it fails to explain the normal decrease in the mobility with salt concentration for hydrophilic latexes with high surface charge (126, 131) where these particles have a significant hairy layer.

The corresponding zeta potentials for the measured electrophoretic mobilities as a function of salt concentration is given in Figure 3-5. Zeta potentials for the latex particle at different salt concentration were obtained from Ottewill's numerical tables (126) which take into account the electrophoretic retardation due to backward flow of the solvent and the relaxation effect due to distortion of the ionic atmosphere surrounding the particle. The zeta potential data for $AlCl_3$ were not attained for lack of numerical tables. The zeta potentials decrease monotonically with increasing ionic strength or decreasing double layer thickness $1/\kappa_0$ (see equation (3.1)), as predicted by electrical double layer theory, in both cases of NaCl and $MgCl_2$. Lower zeta potential was obtained with higher counterion valency.

The effect of temperature on the electrophoretic mobility of model polystyrene latex A is illustrated in Figure 3-6. A slight increase in mobility with increasing temperature was observed for the latexes without added salt and with high NaCl concentration (0.1 M). The notation of up and down indicates the reversibility of the measurements. In a real system the temperature dependences are very complicated, not only is the dielectric constant and viscosity of the medium temperature dependent, but so is the dissociation of any salt in the system and the dissociation of surface acidic groups from the colloidal particles. Though increasing temperature reduces the viscous drag in electrophoresis measurement, its effect on two retarding forces (relaxation and retarding effect) arising from distorted counterions cloud discussed previously in the Introduction is still not known. Nevertheless, an

attempt for the conversion between electrophoretic mobility and zeta potential was made and interesting results were obtained.

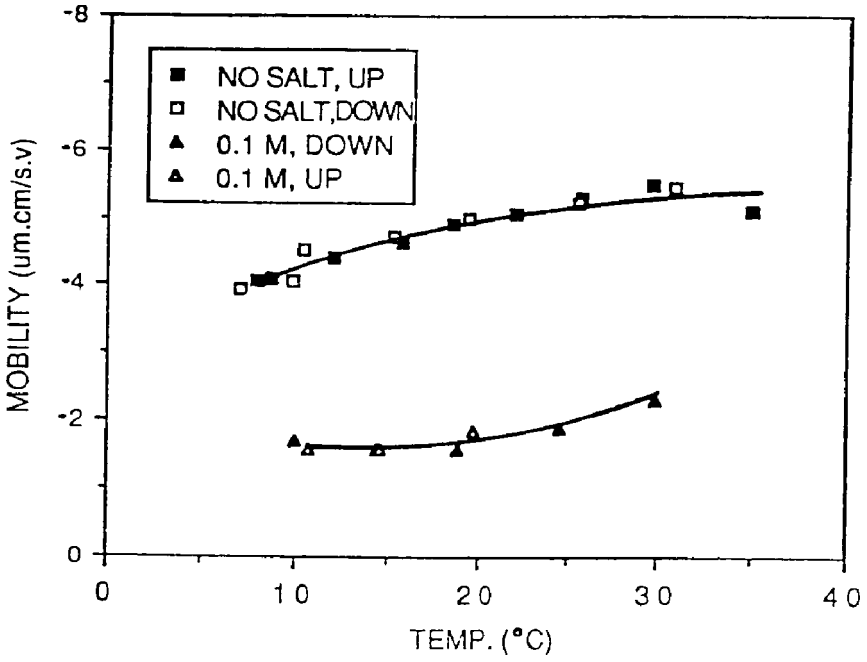

Figure 3-6: *Electrophoretic mobility vs. temperature for latex A at various aqueous NaCl concentrations (mole/l).*

The corresponding zeta potentials for the measured electrophoretic mobilities as a function of temperature is shown in Figure 3-7. The zeta potential was calculated from the electrophoretic mobility by using Smoluchowski and Huckel equation (equation (3.6) and (3.7), respectively) and taking into account the temperature dependence on the viscosity and dielectric constant of water (144). The results show that the zeta potential decreases as temperature is increased for the latex without added salt. Whereas for the latex with high NaCl concentration (0.1 M), the zeta potential is essentially independent of temperature. The pronounced dependency of temperature on the zeta potential can be understood by recognizing the corresponding thicker electrical double layer around the latex particles.

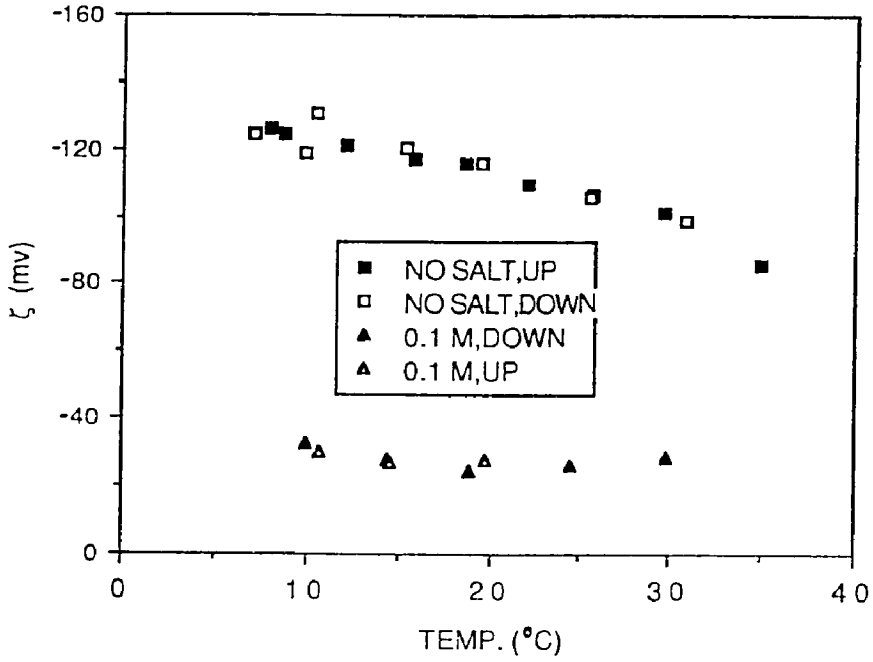

Figure 3-7: *Zeta potential vs. temperature for latex A at various aqueous NaCl concentrations (mole/l).*

According to equation (3.1), the electrical double layer thickness ($1/\kappa_o$) is reduced with increasing either salt valency, salt concentration or temperature (since D is proportional to $T^{-1.5}$, T in °K). The above experimental results also show that the zeta potential of latex A is decreased with increasing salt valency, salt concentration and temperature (for cleaned latex), respectively. The zeta potential (ζ) is usually taken as a good approximation of stern potential (ψ_d). Therefore, the strength and range of electrostatic repulsion between particles is decreased with decreased Debye length and zeta potential based on equation (3.3) and (3.4). The following two figures are used to demonstrate the above perception in terms of the total pair potential energy curve. Figure 3-8 shows the effect of 1:1 electrolyte concentration on the total pair potential energy curve for latex A at 25 °C. Upon increasing the salt concentration, the height for potential energy barrier and effective interaction range are dramatically

reduced. The secondary minimum appears as salt concentration approaches 10^{-2} M. This minimum is not deep enough to cause any appreciable particle flocculation. Even as the secondary minimum becomes significant at higher salt concentration, it occurs at such a smaller interparticle distance (i.e. high particle concentration, $\phi > 50\%$) that it won't be applicable for the present study. Figure 3-9 illustrates the effect of temperature on the total pair potential energy curve for latex A. With increasing temperature from 25 °C to 95 °C, the shape of potential energy profile remains unchanged but the height for potential energy barrier and interaction range are decreased gradually. The above understanding is instrumental in interpreting the optical, rheological and order-disorder phase transition properties of model dispersions which will be discussed in Chapter 4, 5 and 6, respectively.

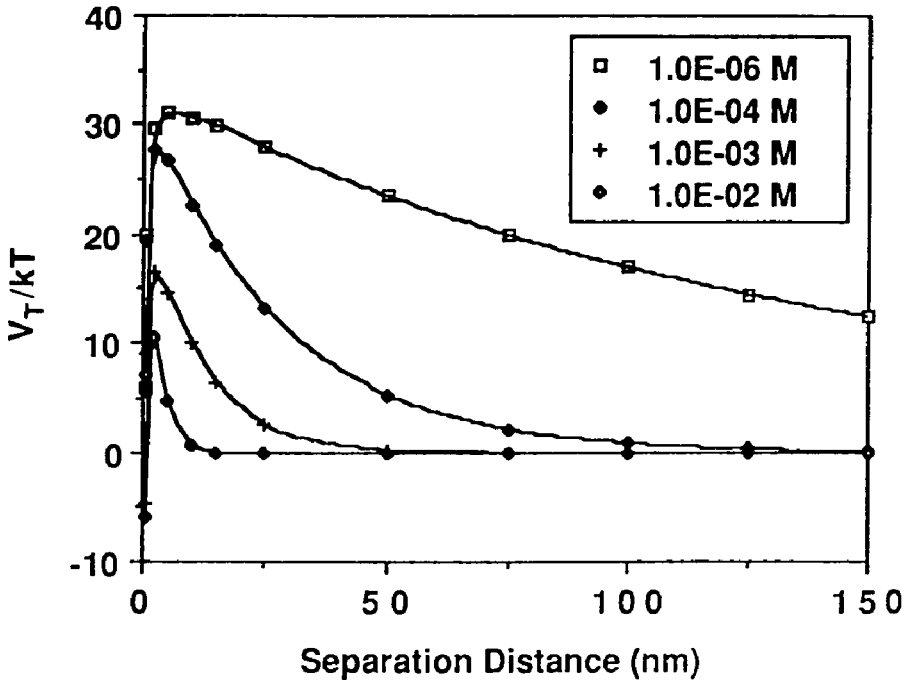

Figure 3-8: *Effect of 1:1 electrolyte concentration on the total pair potential energy curve for latex A at 25 °C; curves drawn with constant values of* A_{121} *(3.5x10*$^{-21}$ *Joule) and* ψ_d *(16.5 mv); kT on y axis = 4.11x10*$^{-21}$ *Joule.*

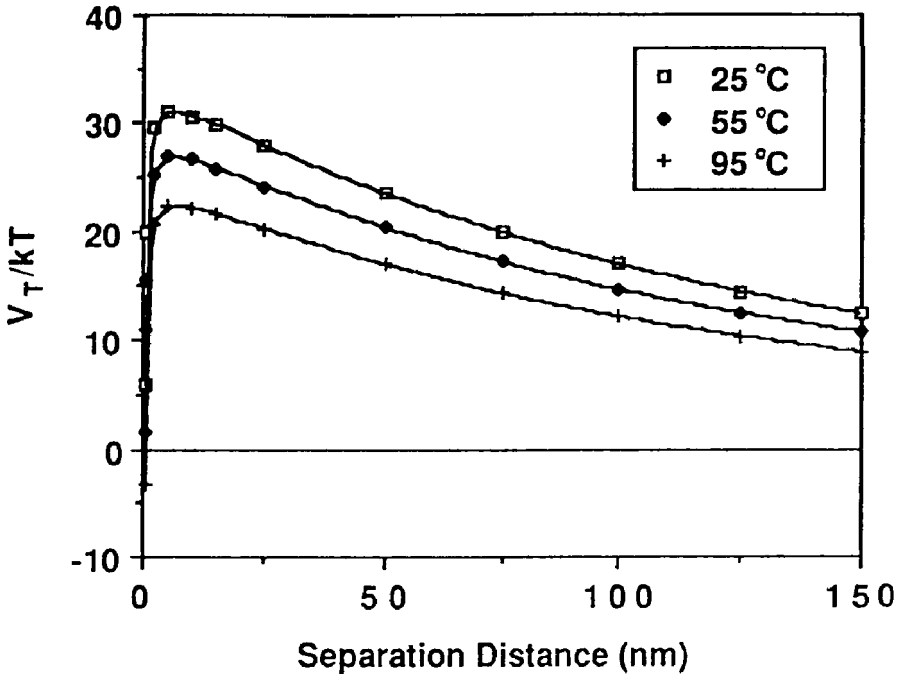

Figure 3-9: *Effect of temperature on the total pair potential energy curve for latex A; curves drawn with constant values of A_{121} ($3.5x10^{-21}$ Joule), ψ_d (16.5 mv) and 1:1 electrolyte concentration (10^{-6} mole/l); kT on y axis = $4.11x10^{-21}$ Joule (at 25 °C).*

Chapter 4
EXPLORATIONS OF DISPERSION MICROSTRUCTURE

4.1 INTRODUCTION

Monodispersed polystyrene latex is an excellent system to investigate the correlation between ordered dispersion microstructure and the interparticle interaction. The crystal-like structure of ordered latexes has been studied by several workers. Hachisu (11) demonstrated unequivocally the presence of a regular latticelike distribution of the particles in dilute dispersion by using a metallurgical microscope. The photograph taken by Hachisu (11) showed clearly the ordered region coexisting with the disordered region. Williams and Crandall (12) found, by means of Bragg diffraction of laser night, that at low particle concentrations only a body-centered cubic (bcc) structure exists whereas a face-centered cubic (fcc) structure exists at higher concentration. An external field has great impact on the particle distribution in the dispersion. Tomita and van de Ven (25) reported that the Bragg diffraction intensity curves obtained from ordered latexes subjected to an electric field shifted to longer and shorter wavelengths depending on the polarity of the electric field. Crandall and Williams (63) studied the effect of gravitational field on the latex structure by optical methods. They found that particle packing gradually changes in the direction of gravity, particles being most densely packed at the bottom of sample container. Okubo and Aotani (30) observed, by metallurgical microscope, the formation of crystal-like structure of giant colloidal spheres (diameter 2-66 μm). They found the balance between electrostatic repulsive force and the compressional force, by the weight of other spheres of the upper layers due to the gravitational field, determined whether spheres will have direct contact or

not. Various optical methods have also been employed to probe the ordered structure. The adaptation of a Bragg X-ray goniometer to measure optical diffraction was described by Krieger (3) and was the procedure utilized to obtain lattice parameters from diffraction data. Ise et al. (22) examined the structure transformation between fcc and bcc and their coexistence by Kossel lines analysis for colloidal crystal of highly charged polystyrene latexes in semidilute aqueous solutions. Pieranski and Pansu (26) proved the utility of the microspectroscopy, an association of reflecting microscope with a monochromatic illumination, for the study of crystal structures and defects (such as grain boundaries and dislocation). The choice of experimental technique for observing ordering depends on the dimensions of the supra molecular species under observation and may include one of the many radiation scattering techniques such as X-ray scattering (55).

The similarity of the structure strongly suggests that the ordered latex is a crystal. But there are three major features which distinguish the ordered latexes from atomic crystals. First, the lattice dimension of colloidal crystal, a few hundred nanometers, is three orders of magnitude larger than atomic crystals, and results in extraordinary physical properties, such as light diffraction (iridescence) and extremely low elastic modulus. Second, the interaction between particles is believed to be screened electrostatic repulsion. Third, the ordered latex is a liquid dispersion. Because of these unique characteristics, convenient parameters, such as particle size, particle concentration, particle surface charge, electrolyte, solvent and temperature, may be employed to finetune the properties of ordered dispersion according to DLVO theory. The dynamics of electrically charged colloidal particles in a dilute solution is also interesting. Ise et al. (23, 58) found that the latex particles in the disordered region show random Brownian motion, whereas those

in the ordered region display oscillatory motion around the equilibrium point. The surprisingly large amplitude of the vibrational motion (10% standard deviation) of the particles in the ordered region indicates that an ordered arrangement of particles is not so rigid as was imagined.

In this work, the effect of particle concentration, temperature, salt valency and salt concentration on the ordered structure of monodisperse latexes were studied by reflection spectrophotometry, a simple and convenient optical technique. Following the treatment of Krieger (3), but with deeper appreciation, the nearest interparticle distance was determined from the wavelength at the reflection peaks according to Bragg's law. The calculated nearest interparticle distance (D_e) was compared with the theoretical nearest interparticle distance (D_t) computed on the assumption of a perfect crystalline lattice. Order-disorder phase transition temperature and salt concentration estimated via the diminishing reflection intensity helped to establish the experimental phase diagram which will be discussed in Chapter 6. The penetration depth of irradiation in the dispersion was estimated from the reflection peak width. The above optical studies not only served to provide more insights into the crystal-like structure of dispersion but also demonstrated the interplay between colloidal forces and dispersion microstructure.

4.2 EXPERIMENTAL

4.2.1 Materials

The water used for the latex cleaning and for dispersion and salt solution preparation was distilled and deionized by Milli-Q water system. The filtration cell used in serum replacement was applied to concentrate the latex. The volume fractions of particles were determined gravimetrically by heating latex samples to 100 °C and knowing polystyrene density 1.054 g/cm^3.

4.2.2 Reflection Spectrophotometry

The reflection spectra of latex samples were recorded by a Cary 2300 spectrophotometer (Varian Associates) which was interfaced with an Apple IIe microcomputer capable of performing spectra display, data analysis and data storage. The instrument set-up is illustrated in Figure 4-1. The system includes a beam monochromator with spectral range from 3152 to 185 nm and separate light detectors for both near infrared and visible/uv regions The Eastman White Reflectance Standard (barium sulfate, $BaSO_4$) was used to establish the baseline of the instrument. The relative reflectance (in %), a ratio between sample and reference reflection intensity, was shown as a function of wavelength. The latex samples were held in a quartz optical cell (Figure 4-2) with a circular window having 3 cm diameter, 0.6 cm thickness and 10 ml volume.

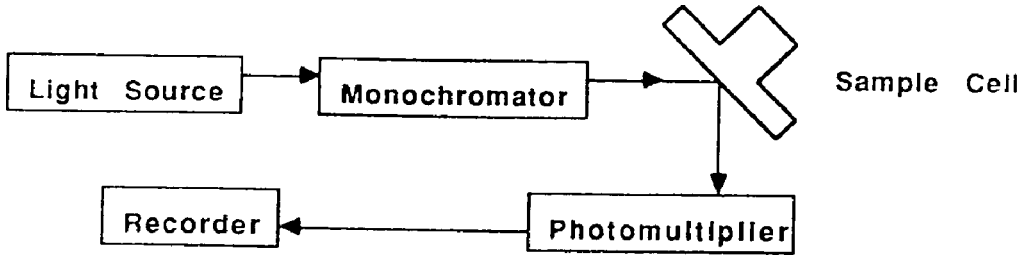

Figure 4-1: *Instrument configuration for reflection spectra measurements.*

4.3 THEORY OF BRAGG DIFFRACTION

4.3.1 Experimental Nearest Interparticle Distance (D_e)

If the distance between the particle centers is of the order of the wavelength of visible light, the monodisperse latex will display a brilliant iridescence due to Bragg diffraction. In order to analyze light diffraction data, Krieger (30) introduced equation (4.1) by analogy of the Bragg's law in X-ray diffraction.

$$2d_{(h\,k\,l)}\sin\theta = m\left(\frac{\lambda_o}{n_s}\right) \tag{4.1}$$

where θ is the diffraction angle in the latex, $d_{(h\,k\,l)}$ is the interplanar spacing in a crystal structure, h, k, l is the Miller indices, m is the diffraction order, λ_o is the wavelength of the light in air, n_s is the mean refractive index of latex suspension.

The optical cell used for reflection spectra measurements is shown in Figure 4-2. The refrative indices of air, quartz glass, water and polystyrene particle are designated by n_a, n_g, n_w and n_p, respectively. n_s can be estimated from the empirical equation (4.2) (3) where ϕ denotes the volume fraction of the latex.

$$n_s = (1-\phi)n_w + \phi n_p \tag{4.2}$$

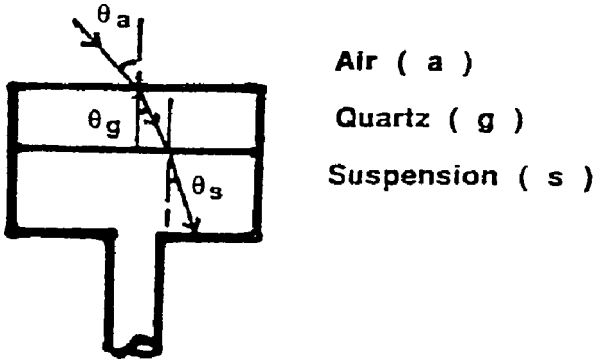

Figure 4-2: *Optical cell for reflection spectra measurements.*

Applying Snell's law at the air-quartz-latex interface, we have

$$\frac{sin\theta_a}{sin\theta_g} = \frac{n_g}{n_a} \tag{4.3}$$

$$\frac{sin\theta_g}{sin\theta_s} = \frac{n_s}{n_g} \tag{4.4}$$

$$\frac{sin\theta_a}{sin\theta_s} = \frac{n_s}{n_a} \tag{4.5}$$

$$so \quad sin\theta = sin(\frac{\pi}{2} - \theta_s) = cos\theta_s = [1 - (\frac{n_a}{n_s})^2 sin^2\theta_a]^{\frac{1}{2}} \tag{4.6}$$

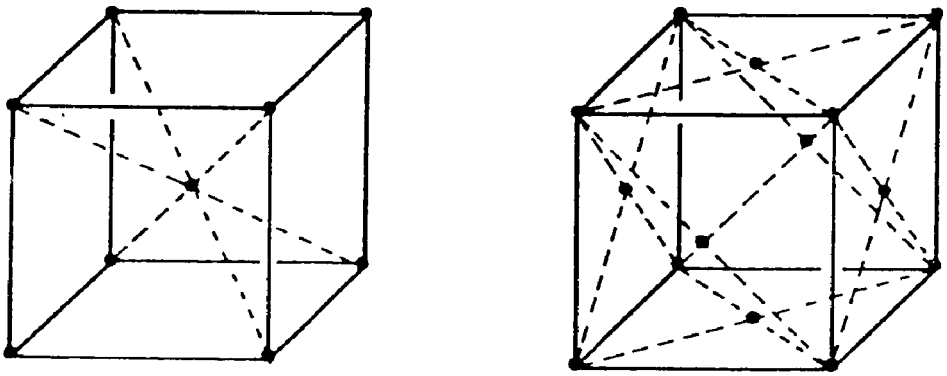

Figure 4-3: *Unit cells for bcc and fcc structure.*

It is expected that double reflection peaks will appear if dual crystal structure exists in the dispersion. But since single peak is observed, each structured dispersion only carrys single type of crystal lattice. Because the type of crystal lattice formed in the ordered latex is usually face-centered cubic (f.c.c.) or body-centered cubic (b.c.c.) (12, 22), the following analysis will be based on these structures. Unit cells for bcc and fcc structure are shown in Figure 4-3. Furthermore, the best fit between experimental and theoretical nearest

interparticle distance (D_e and D_t, respectively) was found if (111) plane of the fcc lattice or (110) plane of bcc lattice was parallel to the interface of optical cell. Therefore

$$d_{(111)\ \text{for fcc}} = \left(\frac{1}{3}\right)^{\frac{1}{2}} b = \left(\frac{2}{3}\right)^{\frac{1}{2}} De \tag{4.7}$$

$$d_{(110)\ \text{for bcc}} = \left(\frac{1}{2}\right)^{\frac{1}{2}} b = \left(\frac{2}{3}\right)^{\frac{1}{2}} De$$

where b is the unit cell dimension. Substitute equation (4.6), (4.7) into equation (4.1), we have

$$2\left(\frac{2}{3}\right)^{\frac{1}{2}} D_e \left[1 - \left(\frac{n_a}{n_s} \sin\theta_a\right)^2\right]^{\frac{1}{2}} = \frac{m\lambda_o}{n_s} \tag{4.8}$$

In the present study, θ_a is equal to 3.33° and n_a, n_w and n_p were taken as 1.00, 1.33 and 1.60, respectively. D_e was thus determined from the wavelength at the reflection peak via equation (4.8).

4.3.2 Theoretical Nearest Interparticle Distance (D_t)

The experimental nearest interparticle distance (D_e) will be compared with the theoretical one (D_t) computed on the assumption of perfect crystalline lattice throughout the latex sample. Consider the volume occupied by the spheres and unit cell, we have

$$\text{for fcc}: \quad \frac{4\frac{4}{3}\pi\left(\frac{D_0}{2}\right)^3}{b^3} = \phi \tag{4.9}$$

$$\text{for bcc}: \quad \frac{2\frac{4}{3}\pi\left(\frac{D_0}{2}\right)^3}{b^3} = \phi \tag{4.10}$$

where D_o is the particle diameter. The relationship between the theoretical nearest interparticle distance and the unit cell dimension is already known as

$$\text{for fcc}: \quad D_t = \frac{\sqrt{2}}{2} b \tag{4.11}$$

$$\text{for bcc}: \quad D_t = \frac{\sqrt{3}}{2} b \tag{4.12}$$

Substitute equation (4.11), (4.12) into equation (4.9), (4.10) , respectively, we

have

$$for\ fcc \cdot \quad (\frac{D_o}{D_t})^3 = \frac{\phi}{0.74} \tag{4.13}$$

$$for\ bcc \cdot \quad (\frac{D_o}{D_t})^3 = \frac{\phi}{0.68} \tag{4.14}$$

D_t can thus be calculated from equation (4.13) & (4.14) by knowing particle volume fraction and particle diameter.

4.3.3 Estimated Irradiation Penetration Depth in Dispersion (t)

Information on the degree of crystal perfection in an atomic crystal is obtainable from the peak width in X-ray diffraction (145). However, in optical diffraction of latex dispersions, peak broadening may be caused by the high scattering factor of the polymer spheres. In the concentrated dispersions, only several crystalline planes near the cell interface contribute to diffraction. On the other hand, it is expected that the decreased turbidity in diluted dispersions allows deeper irradiation penetration and sharpens the diffraction peaks. Particle scattering tendency is not only affected by particle concentration in the dispersion but also influenced by the particle size and refractive index difference between dispersion medium and particle. It was found (10) that when the refractive index difference is increased, the peaks become broader, and virtually the entire peak width could be accounted for by the concept of limited irradiation penetration and beam attenuation.

The typical reflection spectrum at constant diffraction angle θ is illustrated in Figure 4-4. λ_1 and λ_2 are the wavelengths where complete destructive interference occurs. λ_B is the peak wavelength where complete constructive interference occurs. $\Delta\lambda_{1/2}$ is the peak width at half maximum intensity. The path difference equations for two wavelength λ_1 and λ_2 related to the irradiation penetration depth (t) rather than interplanar spacing are listed

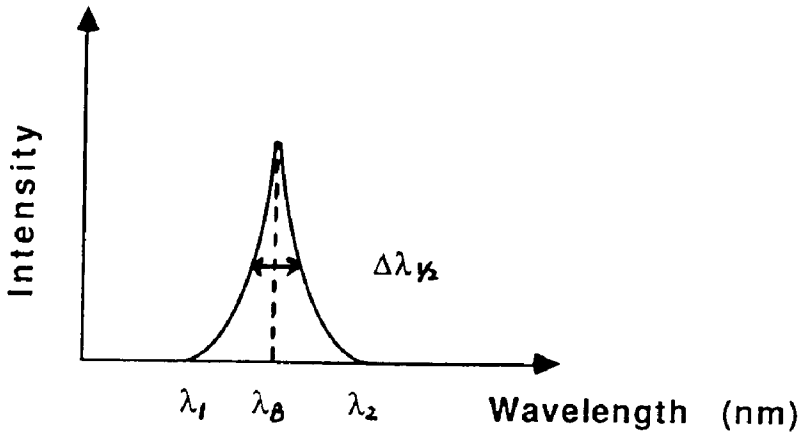

Figure 4-4: *Typical reflection spectrum at constant diffraction angle.*

below.

$$2t\ sin\theta = (m + \frac{1}{2})\ \lambda_1 \tag{4.15}$$

$$2t\ sin\theta = (m - \frac{1}{2})\ \lambda_2 \tag{4.16}$$

In this work, it is difficult to define the λ_1 and λ_2 which gives reflection intensity, and establish the baseline of spectrum. Therefore, λ_1 and λ_2 were alternately obtained from the more reliable information of λ_B and $\Delta\lambda_{1/2}$ by assuming the reflection line is triangular in shape. Hence,

$$\lambda_2 = \lambda_B + \Delta\lambda_2^1 \tag{4.17}$$

$$\lambda_1 = \lambda_B - \Delta\lambda_2^1 \tag{4.18}$$

Substitute equations (4.18) and (4.17) into equations (4.15) and (4.16). The irradiation penetration depth (t) can now be estimated from equation (4.19).

$$t = \frac{[\lambda_B{}^2 - (\Delta\lambda_{1/2})^2]}{4\sin\theta\ \Delta\lambda_{1/2}} \tag{4.19}$$

The number of crystalline layers (N) being penetrated by irradiation can then be calculated from equation (4.20) with the knowledge of interplanar spacing (d) obtained from equation (4.7).

$$N = \frac{t}{d} \tag{4.20}$$

4.4 RESULTS AND DISCUSSION

The latex dispersions with particle volume fractions ranging from 4.37 % to 23.22 % were employed in this reflection spectrum study. These samples were milky and opaque but displayed brilliant iridescence under controlled conditions. The iridescence disappears immediately as the dispersion is shaken and reappears in several seconds if the dispersion is left to stand. A rheological flow oscillation technique described in Chapter 5 is suggested to investigate the kinetics of above crystallization phenomenon.

Figure 4-5 exhibits the reflection spectra of cleaned latexes A at various particle concentrations and 22 °C. These results clearly show that ordered structure is formed in the dispersion. The results also show that the reflection peaks become progressively broader and are shifted in the direction of smaller interparticle spacings with increasing particle concentration. The increase in peak sharpness with dilution is attributed to the smaller irradiation scattering from latex particles and deeper irradiation penetration as discussed in the previous section. Because irradiations are strongly scattered by the particles in the dispersion, it is anticipated that intensity of the reflection peak becomes weaker with higher diffraction order. Indeed, secondary peaks (m=2), although weak, appear at half the wavelength of primary peaks (m=1) and tertiary peaks (m=3) are too weak to be observed. It is also interesting to note that the reflection peak was found at a volume fraction as low as 4.37 % where the particles are 2.5 diameters apart. This implies that long-range electrostatic repulsion between particles is related to the existence of order in dilute dispersion.

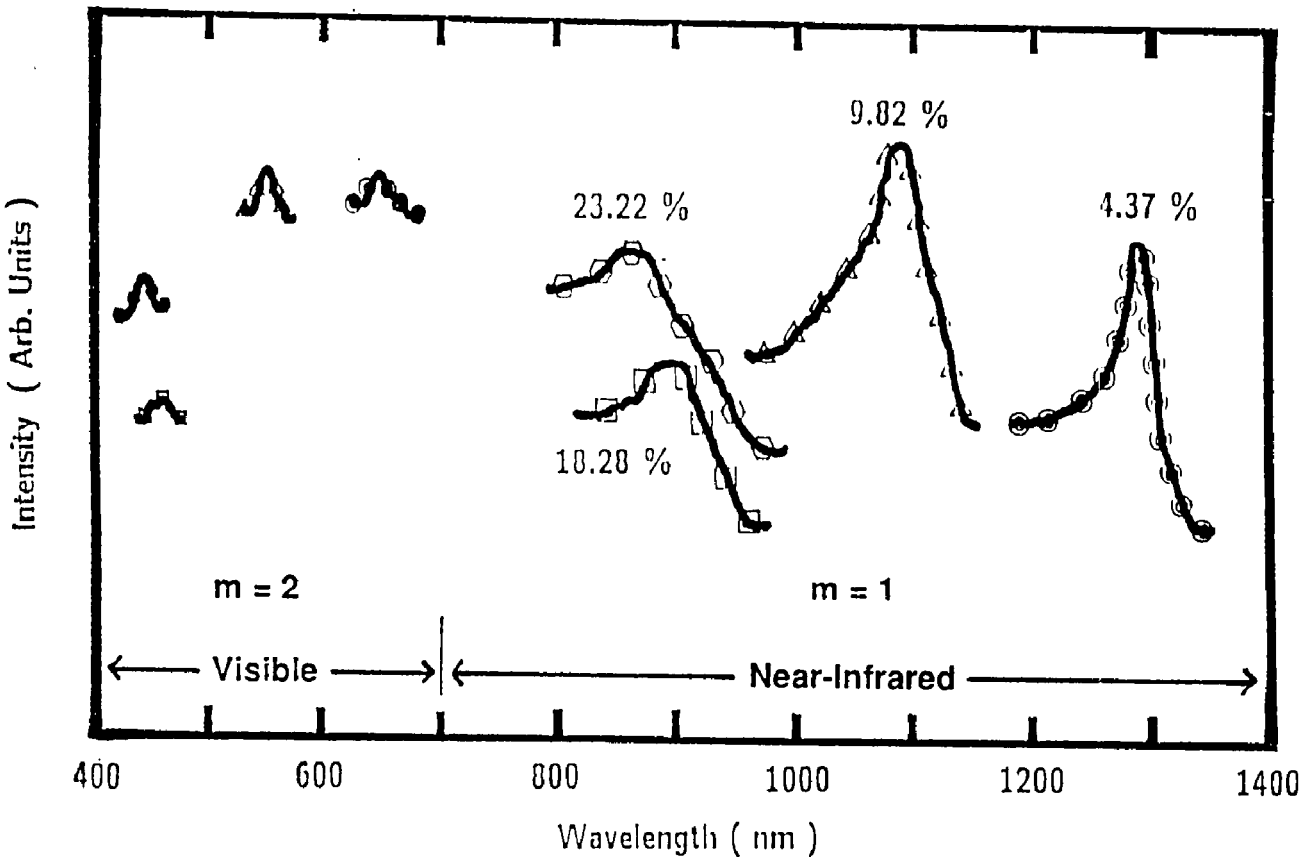

Figure 4-5: *Reflection spectra of cleaned latexes A at various particle volume fractions and 22 °C (intensity x 4 for secondary peaks).*

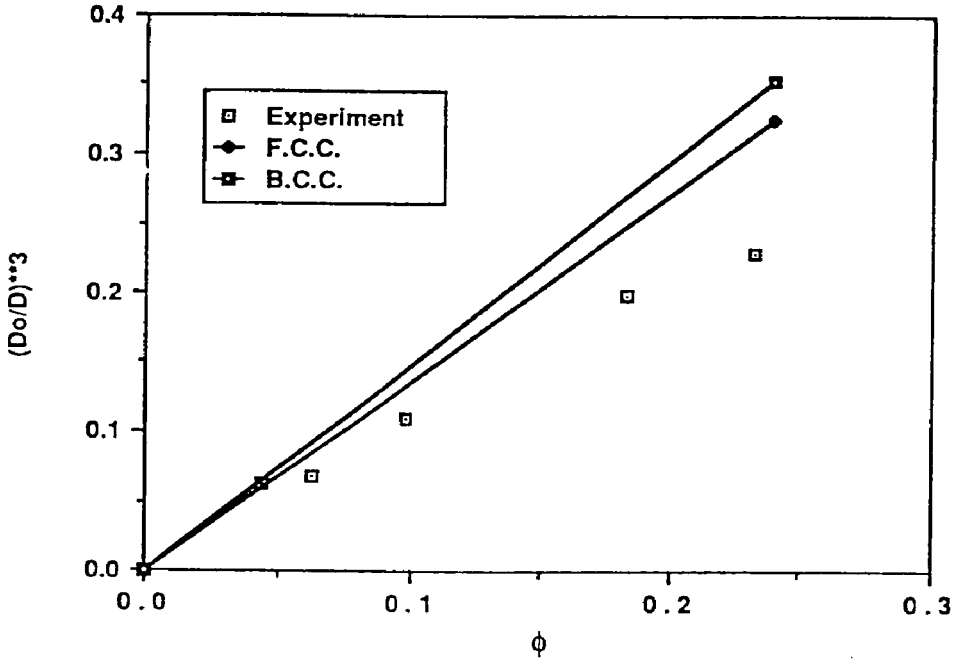

Figure 4-6: *Dimensionless nearest interparticle distance vs. particle volume fraction for cleaned latexes at 22 °C;□: experimental data from reflection spectra, solid lines: theoretical calculation for perfect crystal lattice.*

Based on the Bragg's law, the experimental nearest interparticle distance (D_e) could be obtained from equation (4.8). The theoretical one (D_t) could be calculated from equations (4.13) and (4.14) by assuming a crystal lattice and uniform particle distribution throughout the dispersion. Figure 4-6 provided the comparisons between D_e and D_t. It is shown that the agreement between D_e and D_t is reasonably good but the relative difference $(D_e-D_t)/D_t$ increases with increasing particle concentration. Crystal defects due to the presence of smaller or larger particles and coexistence of ordered and disordered regions might explain the larger deviation at higher particle concentration. A closer match between D_e and D_t of face-centered cubic agrees with the experimental findings in literature (12, 22) that fcc structure is much more stable than bcc at high

particle concentration. It is possible that structure transformation from fcc to bcc at lower partical concentration enables closer match between D_e and D_t of body-centered cubic. Ise et al. (20) examined the interparticle distance as a function of latex concentration by a modified metallurgical microscope. They found $D_e<D_t$ and $(D_e-D_t)/D_t$ decreases with increasing particle concentration which are opposite to what have observed in this reflection spectrum study. Ise often employed diluted dispersion (below 4%) whereas higher particle concentrations were used here. Additional source of electrostatic attraction other than Coulombic repulsion might operate at smaller interparticle distance as particle concentration is increased. Sogami (146) has elucidated such interparticle attraction theoretically. With the coexistence of ordered and disordered regions in the dispersion, it is possible particle motion in the disordered phase were restricted somehow and left more space for the ordered phase to expand their interparticle distance. Hence, $D_e>D_t$ for latexes in high particle concentration region. The above interpretation requires further experimental support and should be viewed critically.

The temperature dependence of the reflection spectra of cleaned latexes A at various particle concentrations is illustrated in Figure 4-7. The spectra measurements were executed ten minutes after the sample cells immersed in a thermostated waterbath had reached the desired temperature. Generally speaking, the reflection intensity decreased with increasing temperature. The peak position displaced unexpectedly toward smaller wavelength with increasing temperature. One possible explanation for this surprising trend is the lattice structure transition, i.e. from fcc to bcc with rising temperature, because bcc possesses narrower interparticle distance than fcc does at constant particle concentration. In order to support the above interpretation and compare the stability of different phases we must look at the difference in their

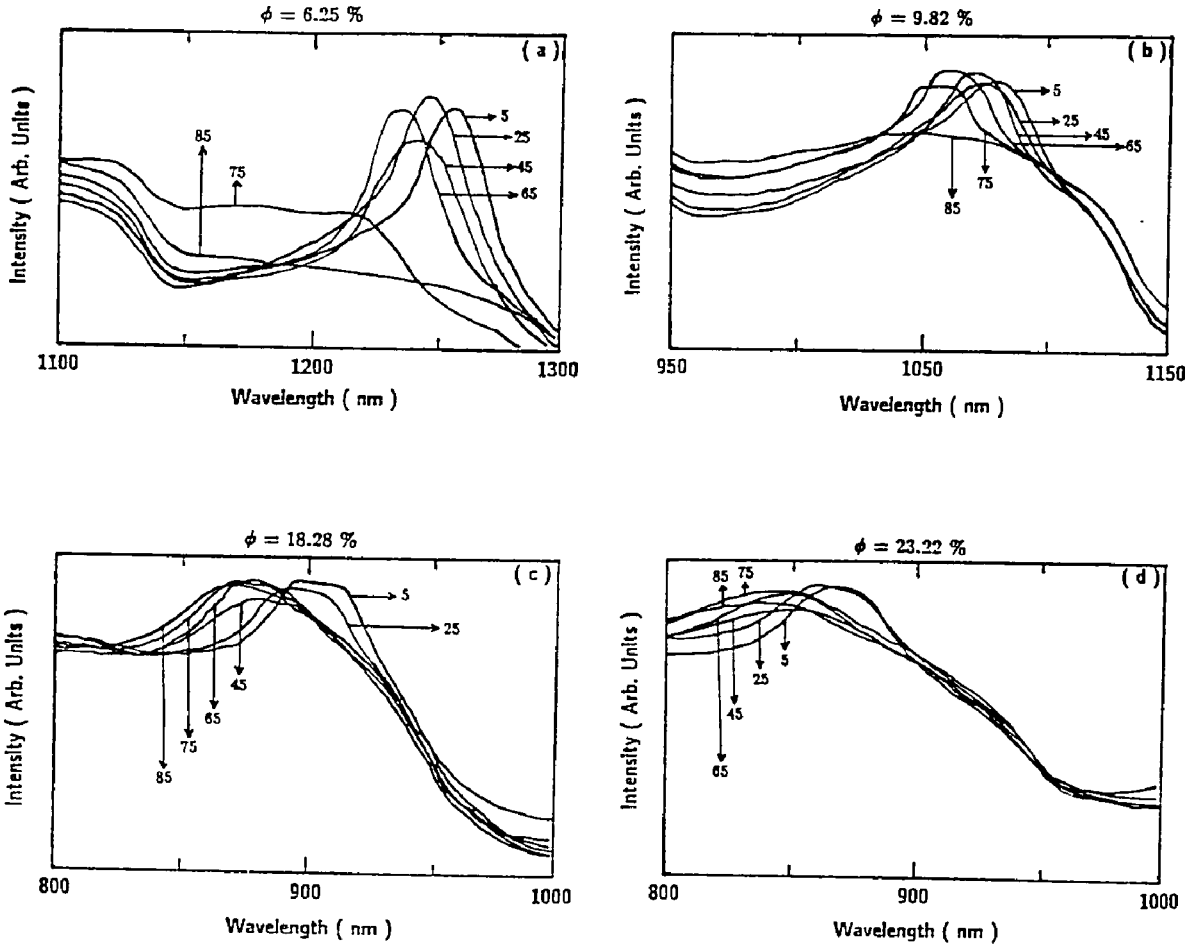

Figure 4-7: *Effect of temperature (in °C) on reflection spectra of cleaned latexes A at various particle volume fractions ϕ (a) 6.25 % (b) 9.82 % (c) 18.28 % (d) 23.22 % (numbers on curves indicate temperature).*

free energies (ΔG) according to the classic thermodynamics :

$$\Delta G = \Delta H - T\,\Delta S \tag{4.21}$$

The enthalpy difference (ΔH) between two crystal configurations is approximately proportional to the screened Coulombic interaction over the nearest-neighbor distances relevant to the two states. The entropy difference (ΔS) accounts for different randomness involved in different phases. If there is a phase transformation from fcc to bcc, the difference in number of the nearest neighbour particles and structure looseness results in negative value of ΔH and positive value of ΔS. The tendency of structure transition becomes higher as temperature is increased because ΔG is forced to be more negative, an indication that the spontaneous transition is more likely to occur. Chaikin et al. (37) took into account the Debye-Huckel electrostatic interaction and temperature-dependent dielectric constant of dispersion medium, and quantitatively described the criteria for structure transitions. Their calculated results further strengthen the credibility of above thermodynamics interpretation.

At higher temperature, more rigorous Brownian motion and reduced strength and range of electrostatic repulsion between particles concluded in Chapter 3 give rise to more freedom to particle motions. Latex spheres can no longer be locked into crystal lattice position. The order-disorder phase transition temperature estimated by monitoring the diminishing reflection intensity increased with increasing particle concentration. The phase transition temperature varied from 75 °C for 6.25 %, 85 °C for 9.82 % and above 85 °C for both 18.28 % and 23.22 %. A higher "melting" temperature is not unexpected with closer packing of particles since the similarity of structure suggests that the ordered latex behaves as a crystal. The electrostatic interactions become stronger and more numerous as particle concentration is increased. These fortified interactions are more capable of resisting the attempt of thermal

motions to disrupt the ordered dispersion structure. Therefore, reflection peak can persist at higher temperatures.

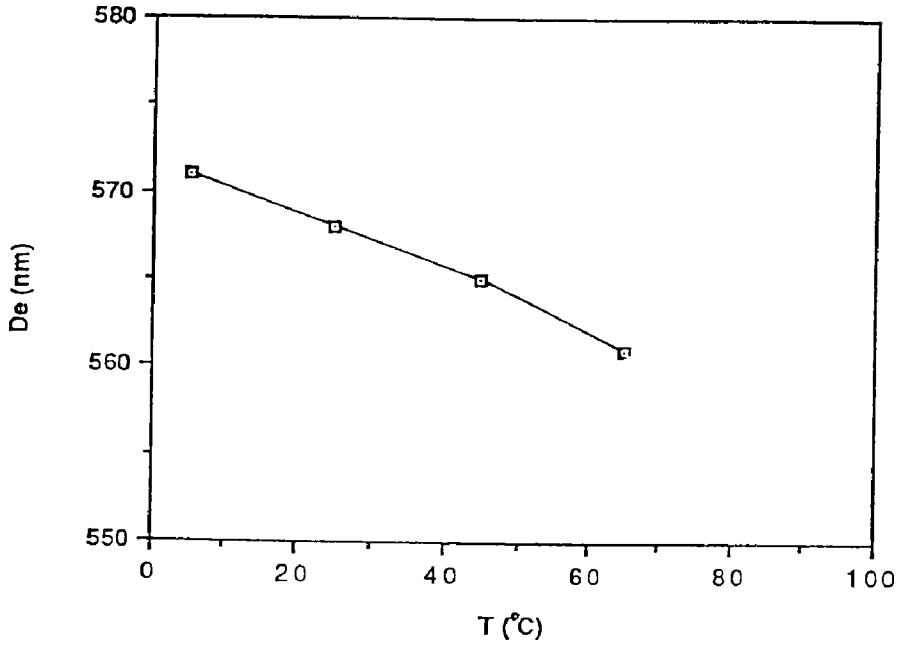

Figure 4-8: *Effect of temperature on the experimental nearest interparticle distance for cleaned latexes A at ϕ=6.25%.*

Figure 4-8 illustrates the effect of temperature on the experimental nearest interparticle distance (D_e) for cleaned latexes A with particle concentration 6.25 %. D_e was calculated from equation (4.8) by finding out the reflection peak wavelength in Figure 4-7. The results show that D_e decreases in a linear fashion with elevating temperature, being 10 nm drop for 60 °C climb-up. This explains why Krieger and Hiltner (5) could not find significant change in their diffraction curve by heating because only limted temperature range (25 ° C-30 °C) was studied.

The effect of salt concentration on the ordered structure of latex dispersions was studied by reflection spectrophotometry as shown in Figure 4-9.

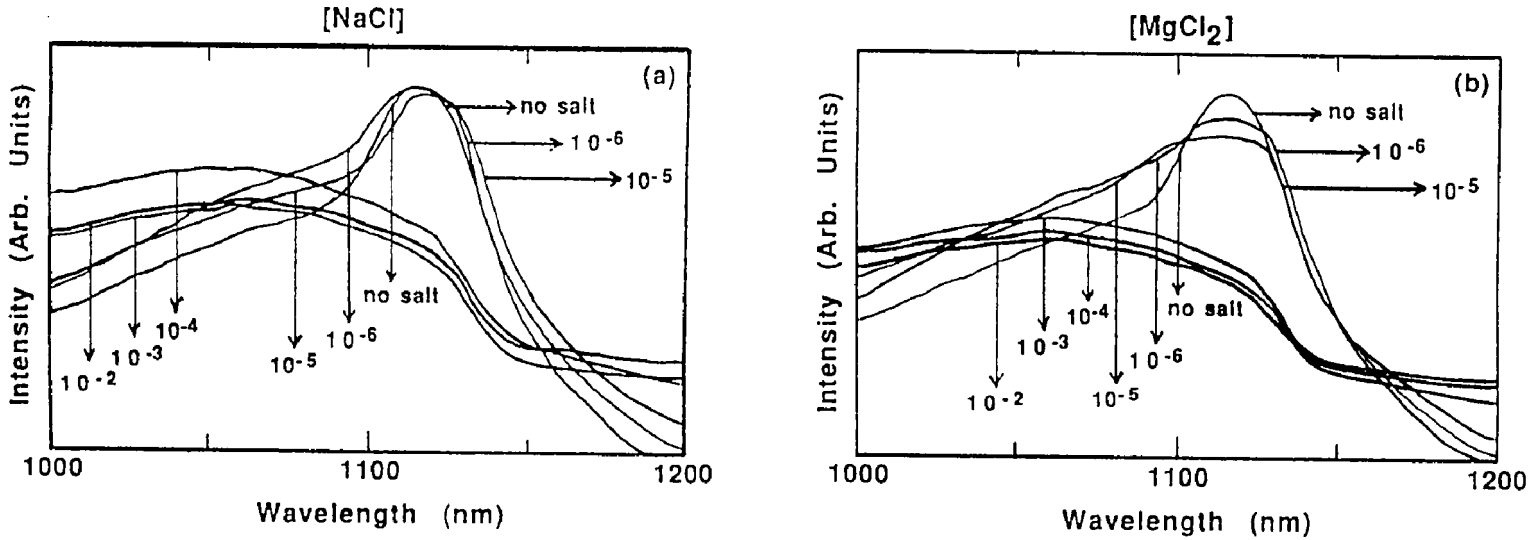

Figure 4-9: *Effect of salt concentration (in mole/l) on reflection spectra of latexes A with* ϕ*=9.03% at 22 °C.*

Generally speaking, the reflection intensity becomes lower and reflection peak becomes broader upon increasing the salt concentration in the range of 10^{-6}-10^{-2} M. It is also shown that the peaks for the polystyrene latex at a volume fraction of 9.03 % at 22 °C shift slightly toward the larger wavelength up to a salt concentration of 10^{-5} M, after which the peaks disappear. The vanishing peak is an indication of order-disorder phase transition since the suppressed electrostatic repulsion no longer can freeze the particles within the crystal lattice and the Brownian motion collapses the ordered structure upon adding excess electrolyte. As the dispersions become more disordered, the limited irradiation penetration and beam attenuation due to particle scattering reduce the reflection intensity and broaden the reflection peaks.

The strength and range of electrostatic repulsion between particles is very sensitive to the counterion valency of the salt. Figure 4-10 exhibits the effect of salt valency on reflection spectra of latexes A with ϕ=9.03 % at 22 °C and various salt concentrations. Higher reflection intensity and narrower peak width were always obtained for the case of NaCl with salt concentration up to $3x10^{-5}$ M, after which the reflection curves for respective concentration of NaCl and $MgCl_2$ overlapped and no reflection peaks were observed. The salt $MgCl_2$ contributes higher ionic strength and suppresses the Debye length more markedly. Hence, the monovalent NaCl can maintain dispersion order at a higher salt concentration than the divalent $MaCl_2$. The order-disorder phase transition phenomenon observed from Figure 4-10(a) to (d) will be fully described and elucidated in Chapter 6. It was found that visual observation of iridescence provided a more sensitive and convenient method to detect the gradual change in order-disorder phase transition than reflection spectra method did.

Effect of particle concentration on the estimated irradiation penetration of

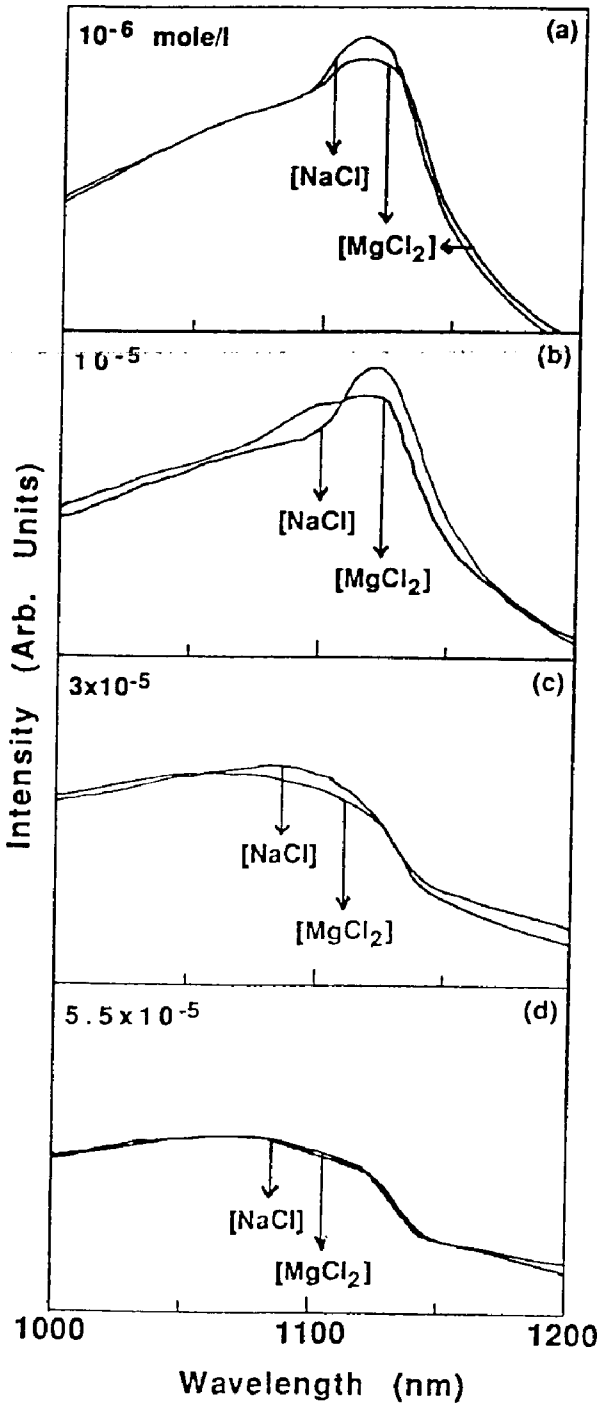

Figure 4-10: *Effect of salt valency on reflection spectra of latexes A with ϕ=9.03% at 22 °C and various salt concentrations.*

cleaned latex A at 22 °C is shown in Table 4-1. The terminology and calculations should be consulted with previous section of Bragg diffraction theory. The number of crystalline layers being penetrated (N) were estimated from the consideration that the peak width is entirely accounted by irradiation penetration depth (t), not by the degree of crystallinity. The results indicate that N decreases from 19 to 5 as particle concentration increases from 4.37 to 23.22 %. This is in agreement with the expectation that less turbidity and particle scattering with lower particle concentraion lead to deeper irradiation penetration into dispersion. Other calculated results for t and N show essentially no dependence on temperature for cleaned latexes with ϕ=6.25 % and slight dependence on salt valency and concentration for latexes with ϕ=9.03 % at 22 °C. N gradually decreases with increasing salt concentration or valency because the disorder of dispersion is easier to be induced under these conditions.

Table 4-1: *Effect of particle concentration on the estimated irradiation penetration in cleaned latexes A at 22 °C.*

ϕ (%)	λ_B (nm)	$\Delta\lambda_{1/2}$ (nm)	t (nm)	De (nm)	d (nm)	N
4.37	1290	45	9250	589	481	19
9.82	1080	71	4097	488	398	10
18.28	900	86	2337	400	327	7
23.22	865	117	1572	381	311	5

Chapter 5
RHEOLOGICAL STUDIES

5.1 INTRODUCTION

Rheology is the science of flow and deformation of materials. Much of the attention on rheological anomalies has focused on polymeric liquids. These materials, which position somewhere between highly elastic solids following Hooke's law and simple viscous liquids obeying Newton's law, show a range of rather unusual responses to flow including Weissenberg effect - the ability to climb up the rotating rod in a regular mixing and significant drag reduction in highly turbulent flow of diluted polymer solution. Both phenomena can be attributed from the substantial deformation of individual polymer molecule by flow. The former is due to the normal stress caused by the elastic nature of macromolecules (147). The later is due to the higher elongational viscosity than that of a newtonian liquid with comparable shear viscosity (147). As the polymer chain is extended, the number of possible chain conformations diminish. Hence, macromolecular elasticity arises through the entropy reduction rather than through changes in enthalpy.

Colloidal dispersions encountered in many industrial applications (eg. paints, pigments, paper coating, printing inks, pharmaceutical and pesticidal preparation, etc.), also deviate from the expected newtonian flow behavior of simple liquids and frequently exhibit such rheological anomalies as pseudoplastic, dilatant and time-dependent thixotropy. Krieger (89) has developed a theory for non-Newtonian flow in hard sphere dispersions. A rotating doublet, formed by Brownian diffusion, causes more dissipation of energy than would two isolated spheres and shear-induced destruction of doublets causes the system to behave as shear-thinning (pseudoplastic) fluid.

The rheological properties of colloidal dispersions are important not only because of the consideration of easy processibility and material handling but also because these properties measure the strength and range of interparticle force. The rheological behavior of ordered dispersions are very interesting because of the elasticity caused by the screened electrostatic forces between particles. Hence, the elasticity of dispersions originated from enthalpy change rather than entropy change as observed in macromolecular fluids. Disordered dispersions usually behave as shear-thinning fluids with a Newtonian low-shear limit. However, infinite low-shear viscosity was obtained with the introduction of order, indicating that a yield stress must be employed to initiate steady flow (62). The ordered dispersion then responds as a linear viscoelastic solid upon small amplitude deformation. In addition, the large crystal lattice spacings in ordered dispersions produce elastic modulus about 10^{10} less than conventional solids (64). It is therefore easy to study rheological properties at accessible stress/elastic modulus ratios higher than previously available.

It is very important to be able to relate the macroscopic rheological properties of dispersion to interparticle forces which are controlled by parameters, such as particle concentration, temperature, salt valency and salt concentration. In the present work, steady state viscosity, dynamic modulus and stress relaxation of ordered latex dispersions were studied as a function of above convenient variables. The applicability of rarely used rheological techniques will be explored. The rheological data were rationalized within the framework of DLVO theory. Efforts were also made to compare the experimental shear modulus with the theoretical high frequency limiting modulus calculated from a crystal lattice model and pairwise additive theory proposed by Goodwin and his coworkers (76). The brief review on historical background of rheological study for ordered polymer colloids and role of colloidal

forces in dispersion rheology will be presented as follows.

5.1.1 Historical Background

The viscoelasticity of structured dispersions can be quantified by static or dynamic techniques. Crandall and Williams (63) obtained the Young's modulus by measuring the vertical compression of the ordered structure due to gravity. They obtained a value of 1 dyne/cm^2 for a latex containing 10^{12}-10^{13} particles/cm^3. This method would be difficult to use systematically to measure the elastic modulus because of a prohibitively long time required for sedimentation equilibrium. The high frequency limit of the storage modulus and the low-shear limit of viscosity have been measured by shear wave propagation and by creep compliance measurements, respectively (75). The rigidity and viscosity of monodisperse latexes were measured by the torsional quartz crystal method (64, 66) at high excitation frequency (40 KHz and 70 KHz), and an abrupt change was found at the order-disorder transition. In an experiment performed with a Zimm low shear viscometer, Mitaku et al. (66) measured the yield stress of about 1 dyne/cm^2 . Using the relation which relates the yield strss to the elastic modulus, they find the value of elastic modulus (about 10^3 dyne/cm^2) compatible with that obtained by torsional quartz crystal methods. Pieranski et al. (79) proposed a simple method to determine the elastic modulus of the ordered dispersion from the spectrum of their mechanical vibrations. Upon exciting shear wave in latex samples, the amplitude and phase of vibrations were detected using Kossel rings phenomena. Analysis of the resonance peaks observed in the mechanical spectrum allows the determination of elastic modulus. Ackerson (86) demonstrated the complex variety of behavior observed for viscosity vs. shear rate for model suspensions of spherical particles : (i) Newtonian behavior, (ii) shear-thinning behavior, (iii)

shear thinning followed by shear thickening, followed by shear thinning as the shear rate increases, (iv) shear thinning interrupted by a discontinuous viscosity jump at a finite shear rate. Okubo (88) claimed the stress-strain relationship for the crystal holds in the range of small shear rate values where the crystal-like structures are distorted but do not flow by the shear. Therefore, he evaluated the elastic modulus of ordered dispersions by a rotational viscometer to be 330-1900 Pa from plots of shear stress against shear rate times time. These moduli values are the highest among those reported in the literature (0.01-100 Pa). Russel et al. (70) used a home-made membrane osmometer and oscillatory viscometer and found the osmotic pressures and shear moduli increase by orders of magnitude with increasing particle concentration and decreasing particle radius or ionic strength. Chaikin et al. (81) observed the "shear melting transition" accompanied by an increase in viscosity at sufficiently high stress in going from solid to liquid, as reported by Hoffman (92). The concept is that below this transition ordered flow of layers are formed, and that above the transition the particles are disordered.

5.1.2 Role of Colloidal Forces in Dispersion Rheology

The rheological characteristics of dispersions depend strongly on the interparticle forces. A particle in a suspension is subjected to various forces, e.g. hydrodynamic, thermal, van der Waals, electrostatic and steric repulsion, etc. which in turn, are associated with various parameters such as shear rate ($\dot{r}$), particle radius (a), solvent viscosity (η_0), temperature (T), dielectric constant of solvent (D), stern potential of particle (ψ_d), surface to surface particle separation (H), adsorbed stabilizer layer thickness (Δ), Flory-Huggins interaction parameter (χ), volume of solvent molecule (V_s), Hamaker constant (A), particle volume fraction (ϕ), minimum separation (δ), Debye length ($1/\kappa$), salt valency

and salt concentration. Dimensional analysis of the relevant forces (Table 5-1) (96) allows a classification of dispersions according to their stability and the effect of externally imposed flow. Typical colloidal dispersions without hydrodynamic interference are either in a flocculated state, with $A/kT>1$ and $D\psi_d^2 a\exp(-\kappa H)/kT<<1$ or $[(1/2)-\chi]<0$, or in a stable state, with $D\psi_d^2 a\exp(-\kappa H)/kT>>1$ or $[(1/2)-\chi]>0$. For neutrally stable dispersions, if Brownian motion could not restore the equilibrium microstructure being disturbed by viscous force, the dispersions then display non-Newtonian behavior. Hence, for simple fluids with smaller molecular dimensions to produce nonlinear rheology, extremely high shear rates were required because of $\eta_o a^3\dot{r}/kT<<1$.

Neutrally Stable Dispersions

The appropriate dimensionless group to characterize this system is Peclet number $Pe=6\pi\eta_o a\dot{r}^3/kT$. Models of hard sphere polystyrene latex suspensions were prepared by Krieger (89) screening the coulombic repulsion forces with sufficient electrolyte or using less polar media such as benzyl alcohol or m-cresol. Evidence of hard sphere was provided by the fact that the relative viscosity over a specific volume fraction obtained with dispersions of variety particle radii and medium viscosities superimpose when plotted against the dimensionless shear rate (Pe). These results show conclusively that only Brownian and hydrodynamic forces are responsible for the flow and attractive and repulsion forces are minimized.

Electrostatically Stabilized Dispersion

This represents the case where the particle interaction is dominated by long-range electrostatic repulsion. The proper dimensionless group to characterize the system is $\eta_o a^2\dot{r}/D\psi_d^2\exp(-\kappa H)$. Krieger and Eguiluz (62) employed polystyrene latexes and presented series of viscosity curves

Table 5-1: *Dimensional analysis on particle interactions.*

Interaction Energy	Scale	Dimensionless Groups
Viscous	$\eta_o a^3\dot{\gamma}$	-
Brownian	kT	$\eta_o a^3\dot{\gamma}/kT$
Electrostatic	$D\psi_d^2 a \exp(-\kappa H)$	$\eta_o a^2\dot{\gamma}/D\psi_d^2 \exp(-\kappa H)$
Steric	$a\Delta^2(1/2-\chi)kT/V_s$	$\eta_o a^2\dot{\gamma} V_s/\Delta^2(1/2-\chi)kT$
Dispersion	A	$\eta_o a^3\dot{\gamma}/A$

Length	Scale	Dimensionless Groups
Particle Radius	a	-
Mean Separation	$2a(\phi^{-1/3}-1)$	$2(\phi^{-1/3}-1)$
Repulsion	$1/\kappa$ or Δ	$a\kappa$ or Δ/a
Attraction	δ	δ/a

Time	Scale	Dimensionless Groups
Viscous	$1/\dot{\gamma}$	-
Brownian	$6\pi\eta_o a^3/kT$	$6\pi\eta_o a^3\dot{\gamma}/kT$

corresponding to various $HCl_{(aq)}$ concentration. At the high shear limit where hydrodynamic forces dominate, the viscosity changes little and curves tend to converge. Whereas at the low shear limit where repulsive forces dominate, the viscosity differs dramatically and Newtonian plateau disappears for the latex with longer Debye length and lower HCl concentration. The viscosity under the above conditions diverges at a critical stress, indicating a solid rest state which can withstand a yield stress before flowing.

The presence of electrical charges on the latex particles can lead to contributions to the viscosity of the dispersion from electroviscous effects. There

exist three distinguishable electroviscous effects. The primary effect is due to the distortion of the double layer of the particles under shear. This effect is difficult to measure due to only a small increment in intrinsic viscosity over the Einstein value for uncharged spheres. Recent efforts by Ali and Sengupta (84) showed that the surfactant-free polystyrene latexes with larger particle size yield the primary effect which decreases with increasing connterion concentration as expected. Honig et al. (149) claimed the primary effect is measurable within low particle concentration regime and is important only if the double layer thickness is of the same order of magnitude as the size of the particle. This implies that the particles must be very small in order for the primary effect to be dominant. The secondary effect results in an increase in the viscosity at finite concentrations due to coulombic interactions between the double layers of different particles. This effect can change dispersion viscosity by an order of magnitude and is more pronounced in cleaned latexes system. Wang (150) attributed the increase in viscosity to an increase in the effective hydrodynamic radius of the particle by the double layer thickness which is sensitive to electrolyte content. An alternate explanation (151) involves the displacements of the paths of neighboring particles due to electrostatic repulsions. The tertiary effect is due to the distortion of the particle itself as a result of electrostatic forces. This effect is eliminated in latex systems where the particles are rigid.

Sterically Stabilized Dispersions

These are dispersions where particle interactions were dominated by steric repulsion achieved by adsorbed layers of surfactants, nonionic polymers or polyelectrolyte on particle surface. The proper dimensionless group to characterize this system is $\eta_o a^2 \dot{r} V_s / \Delta^2 [(1/2)-\chi] kT$. Non-aqueous dispersions with insignificant electrostatic interaction and where the adsorbed layer is relatively

small compared to the particle radius approach hard spheres system. This has been demonstrated by Willey and Macosko (148) using sterically stabilized poly (vinyl chloride) suspensions in several solvents. They successfully correlated the relative viscosities at a particular particle concentration with the Peclet number alone, independent of the magnitude of the repulsive potential and the particle size.

Flocculated Dispersions

Unstable, or flocculated dispersions pose more difficult problems both theoretically and experimentally because of the nonequilibrium nature of the structure at rest resulting from relatively weak Brownian motion (95). The appropriate dimensionless group to characterize this system is $\eta_0 a^3 \dot{r}/A$. At a high volume fraction, the particles can form a volume-filling network capable of supported stress. At low shear rates, the network deforms plastically. At high shear rates, the network is broken down into discrete flocs. The size of the flocs will be determined by a balance between the shear forces and forces of attraction which hold the particles together. In steady shear, many flocculated dispersions display pseudoplastic behavior.

5.2 EXPERIMENTAL

5.2.1 Materials

The water used for the latex cleaning and for dispersion and salt solution preparation was distilled and deionized by Milli-Q water system. The Rotary Evaporator (Buchi-Rotavapor, Switzerland) under reduced pressure or filtration cell used in serum replacement were applied to concentrate the latexes. Particle volume fractions were measured by drying weighed samples at 100°C to constant weight. To prepare latexes containing electrolyte, the particle concentration was first adjusted to a value somewhat higher than desired, so

that subsequent dilution by stock electrolyte solution would yield the desired concentrations. Salt concentrations of latexes reported here are molarities (mole/l) based on the total volume of dispersion.

5.2.2 Rheometry

A model Bohlin VOR Rheometer (Bohlin Reologi, Lund, Sweden) interfaced with an IBM/AT personal computer and electronically controlled thermobath was used for rheological measurements including steady-state-viscometry, dynamic oscillation, strain sweep, flow oscillation and stress relaxation. The instrument has interchangeable torsion bars covering a wide range of sensitivities. A coaxial cylinder (C14) with a moving cup of diameter 15.4 mm and a fixed detector bob of diameter 14 mm was used for shear viscosity measurements. Another coaxial cylinder (C25) with cup of diameter 27.5 mm and bob of diameter 25 mm was used for dynamic and transient measurements. Calibration of the instrument was carried out using Newtonian mineral oil (Cannon Instrument Co., U.S.A.). In order to avoid errors due to evaporative drying of latex samples, high humidity was maintained around the sample by an aqueous aerosol spray.

Steady-State-Viscometry

The stress response of a sample to a constant shear rate is measured in a viscosity measurement. The ratio of shear stress to shear rate is the apparent viscosity. The instrument is capable of running shear rate sweep (10^{-3}-10^{3} 1/s), time and temperature sweep. Stress growth is a phenomenon of an elastic liquid that shows up as a response to a transient shear rate. Finite delay time is required for the stress response to reach a steady value. 5 sec delay time and 10 sec integration time to average stress responses were used in this work.

Dynamic Oscillation, Strain Sweep and Flow Oscillation

In the oscillatory measurements, one applies a sinusoidal strain with a certain amplitude and angular frequency ω ($\omega=2\pi f$, f in Hz) to the cup of a concentric cylinder and then simultaneously compares the measured stress with the strain. If the system is purely elastic, within this amplitude and frequency range, the stress and the strain will be exactly in phase, i.e. the phase angle shift $\delta=0^{o}$. But, if the system is purely viscous, then $\delta=90^{o}$. Viscoelastic system falls between above two extremes and has $0^{o}<\delta<90^{o}$. The phase shift is automatically computed from the time displacement between the sine waves of stress and strain, i.e. $\delta=\omega\,\Delta t$. From phase shift (δ) and amplitudes of stress (τ_o) and strain (ε_o) one can obtain various rheological parameters (152), i.e. complex modulus ($G^*=\tau_o/\varepsilon_o$), storage modulus ($G'=G^*\cos\delta$), loss modulus ($G''=G^*\sin\delta$). phase shift ($\delta=\tan^{-1}(G''/G')$), dynamic viscosity ($\eta'=G''/\omega$) and $G^*=G'+iG''$ where i is equal to $(-1)^{1/2}$. However, for the above relationships to be applicable, one should be in the linear viscoelastic region, i.e. where G*, G' and G'' are independent of applied strain (ε_o). Strain sweep is thus carried out at fixed frequency. In this work, linear dynamic moduli was always obtained if the peak strain was less than 7 %. G' storage modulus is a measure of energy stored per cycle of deformation and represents elastic contribution. G'' loss modulus is a measure of energy dissipated per cycle of deformation and represents viscous contribution.

An elastic liquid suddenly subjected to a sinusoidal strain will respond with a gradual attainment of steady dynamic stress. Finite delay peroids were applied in the present work to avoid this problem. The instrument is capable of oscillating at frequency ranging from 10^{-3} to 20 Hz. However, in order to avoid instrumental effects, the operation frequency is always below 0.3 times resonance frequency depending on measuring geometry and torsion bar.

The flow oscillation technique used to follow the structure recovery of the

latex dispersion involves an oscillation measurement after steady shearing for a finite period of time. G', G" and δ are displayed as a function of time.

Stress Relaxation

In the stress relaxation experiment, material is subjected to a rapidly applied small strain which is held constant for the remainder of the experiment. The relaxation behavior is then studied by continuously monitoring the decayed stress vs. time, t. The stress divided by the constant strain gives the relaxation modulus G(t), and the relaxation spectrum H(λ), to the first order approximation, can be readily calculated from $[-dG(t)/dlnt]_{t=\lambda}$ by applying Alfrey's rule (153). G(t) is a constant with time for a perfect elastic material. Whereas for a perfect viscous fluid, G(t) drops to zero immediately upon an instantaneous strain. G(t) for a viscoelastic material falls between above two limiting cases and usually show the exponential decay behavior with time.

Strain rise time which is the time it takes the angular deflection of the cup to reach from zero to the set value should be short compared to the sample relaxation time. If this is not the case, some relaxation will occur during the initial straining period. In this case the relaxation modulus will depend on the strain rise time. On the other hand, a short rising time will give more pronounced contribution from instrument and sample inertia effects. Strain rise time 0.02 sec was used in this work.

5.3 THE THEORETICAL SHEAR MODULUS OF ORDERED LATEXES

It has been established by reflection spectrum study in Chapter 4 that latex particles will form ordered structures under condition of low electrolyte concentration, high particle concentration or low temperature. With the knowledge of crystal lattice and the applicability of DLVO theory, it seems

proper at this moment to theoretically account for the mechanical propeties of the structured dispersions and correlate these properties to particle interactions. Comparisons between experimental observations and theoretical predictions can thus be made. One of the targets in mechanical properties is the shear modulus. Following the treatment of Goodwin and his coworkers (76), the shear modulus of ordered latexes could be derived from the increase in electrostatic energy caused by a small shear strain to a structured dispersion. To avoid the duplication, detailed mathematic derivations are not recorded here. Instead, important concepts involved are pointed out.

Consider a pair of particles separated by a distance in the Cartesian coordinate system, fixing one at origin and one at remote. A small shear strain is then applied, which initiates a high frequency shear wave. The time period of shear wave is short compared with the relaxation time of the particles in the array. Also, the relaxation time of the electrical double layer is small compared with that of the crystal lattice. These conditions enable shear modulus determination on the basis of equilibrium electrical double layer.

The shear strain displaces the remote particle with a distance. The restoring force required is calculated from the DLVO particle pair interaction. The pairwise contribution to the shear stress obtained by ratio of restoring froce and projected area of particle pair was then averaged over all orientations. Consider only the nearest neighbour interactions and use pairwise additive approach, the high frequency limiting shear modulus G (∞) which is equal to the total shear stress divided by the shear strain is finally attained.

$$G(\infty) = \frac{\alpha}{R}\left(\frac{\partial^2 V_T}{\partial R^2}\right) \tag{5.1}$$

where α is a geometric factor and equal to $(3/32)\phi_m n$, ϕ_m, the maximum close packing volume fraction of particles, n, number of nearest neighbour particles, R, the nearest interparticle distance in nm and V_T, total potential energy of

interaction between a pair of particles.

As pointed out by DLVO theory (1), V_T is composed of two main contributions, the electrostatic repulsion, V_R, due to overlay of the electrical double layers, and the van der Waals attraction, V_A, arising from electromagnetic fluctuations. Substitute equations (3.3) to (3.5) for V_T in Chapter 3 into equation (5.1), the analytical expression for $G(\infty)$ then has the following form:

$$\text{for } \kappa a < 3 \qquad G(\infty) = 4\pi\alpha D\varepsilon_0 a^2 \psi_d^2 \left(\frac{\kappa^2R^2 + 2\kappa R + 2}{R^4}\right) \exp[-\kappa(R-2a)] - \frac{2A_{121}\alpha}{3a^2R}\left\{\left[\frac{3s^2+4}{(s^2-4)^3}\right] + \left(\frac{3}{s^4}\right) - \left[\frac{2(3s^2-4)}{s^2(s^2-4)^2}\right]\right\} \tag{5.2}$$

$$\text{for } \kappa a > 10 \qquad G(\infty) = \frac{2\pi\alpha D\varepsilon_0 \psi_d^2 a}{R}\left(\frac{\kappa^2 \exp[-\kappa(R-2a)]}{\{1+\exp[-\kappa(R-2a)]\}^2}\right) - \frac{2A_{121}\alpha}{3a^2R}\left\{\left[\frac{3s^2+4}{(s^2-4)^3}\right] + \left(\frac{3}{s^4}\right) - \left[\frac{2(3s^2-4)}{s^2(s^2-4)^2}\right]\right\} \tag{5.3}$$

where D, the dielectric constant of continuous medium (78.54 for water at 25°C), ε_0, the permittivity of free space (8.854 x 10^{-12} coul/v m), ψ_d, the stern potential in mV, a, the particle radius in nm, $1/\kappa$, the Debye length in nm, A_{121}, the Hamaker constant in Joule and S, the ratio between R and a.

5.4 RESULTS AND DISCUSSION

5.4.1 Steady State Viscometry

Figure 5-1 shows the viscosity curve of cleaned latex A at various particle concentrations at 25°C. It is expected that at low shear rate, the viscosity of cleaned latex will climb as though approaching a vertical asymptote, which would indicate a yield stress, as observed by Krieger and Eguiluz (62), and the yield stress will increase with increasing particle concentration. However, due to the sensitivity limitations of the instrument, the anticipated infinite viscosity at low shear is not found. Instead, typical pseudoplastic behavior and

Newtonian high-shear limit were seen for samples with high and low particle concentration, respectively. The rising viscosity with higher particle concentration can be explained qualitatively by the secondary electroviscous effect, i.e. the increase in energy dissipation resulting from alterations of particle trajectories due to the presence of electrical charges, which cause the particles to avoid one another.

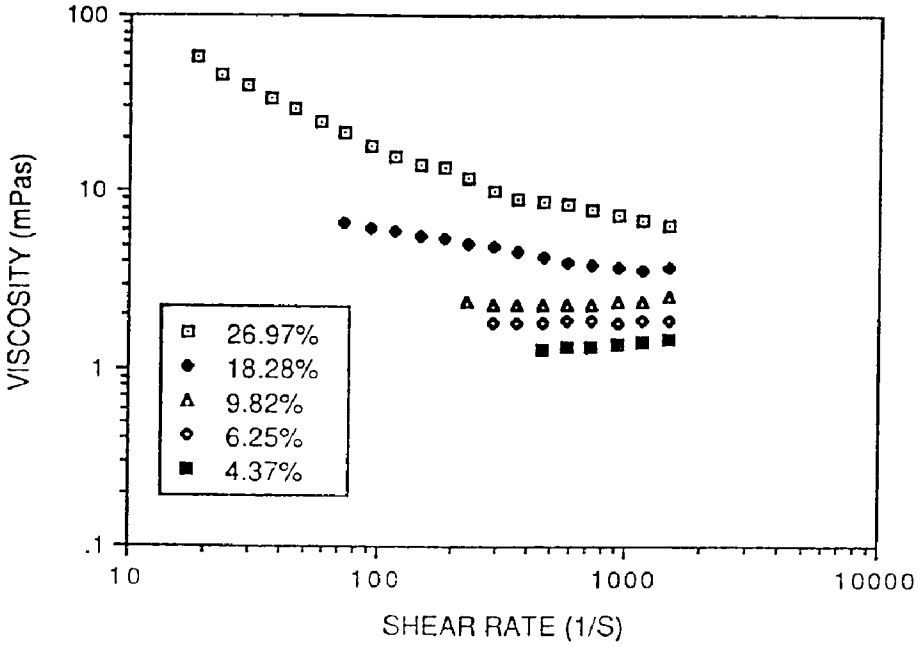

Figure 5-1: *The viscosity profile of cleaned latex A at various particle volume fractions at 25°C.*

Hoffman (154, 155) proposed a mechanism for shear flow of uniform dispersions which covers the whole shear rate range. The low shear Newtonian region (I) corresponds to flow of a particle array characteristic of the static dispersion without disturbance. The high shear Newtonian region (III) corresponds to fully developed hexagonally ordered layers gliding over one another. Shear thinning region (II) is the transition as the ordered sheets develop. Eventually, shear thickening region (IV) sets in where ordered layer

flow becomes unstable and then continuous or discontinuous jump in viscosity is observed. The formation of layered structures in highly concentrated dispersions for Pe>>1 and the breakup of these layers due to the pevailing hydrodynamic couple acting across them over restoring couple from the interparticle force were well substantiated by the Hoffman's rheo-optical analyses. In Figure 5-1, dilatancy behavior was found for samples with particle concentration below 10 %. This is attributed to the onset of turbulent flow at high shear rate for samples with low kinematic viscosity (a ratio between viscosity and density). In general, calculation of viscosity assumes laminar fluid flow. When secondary flows set in, the added energy dissipation gives rise to additional torques. These torques then produce data which mistakenly suggests shear thickening of a Newtonian fluid. Shear induced order disorder transition was not the case here because at low particle concentration unhindered particle rotations dissipated the viscous couple that was required to destroy the stability of ordered layer flow.

In the viscosity measurements, the maximum shear rate before the onset of turbulence depends on the measuring couette geometry and the kinematic viscosity of samples. Laminar flow in the system in which the outer cylinder is rotating is strongly stabilized by centrifugal forces. Thus a fluid particle from an outer layer opposes being moved inwards because the centrifugal force on it is greater than on particles nearer the axis of rotation. At the same time, its outward movement is resisted by the higher centrifugal force on the particles it would have to replace. As a result, the transition to turbulent flow takes place at a much higher Reynolds number here than in the corresponding system in which the inner cylinder is rotating and in which the centrifugal force tends to introduce instability. In this work, the calculated critical shear rate (156, 157) to induce secondary flow for C14 measuring geometry and latex dispersion with

ϕ=9.82% is 280 1/s. But the fact that turbulent flow occurs at a higher shear rate around 800 1/s indicates that the ordered microstructures suppress the flow instability. The sheared ordered dispersion is a fairly low viscosity fluid along the flow lines but retains its rigidity in the radial direction. Since turbulent flow requires radial velocity, the flow instability is suppressed. This point of view was supported by Chaikin et al's (60) observation on the onset of combined shear melting and turbulence instability for couette geometry with the inner cylinder rotating. They found the critical shear rate increased with decreasing electrolyte concentration in the latex dispersion.

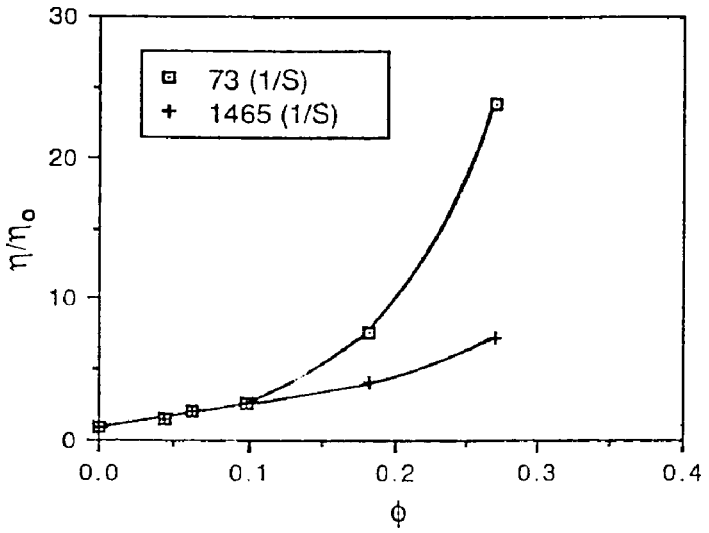

Figure 5-2: *The low and high shear viscosity of cleaned latex A as a function of volume fraction at 25 °C (η_o=0.8937 mPas).*

A crossplot of data in Figure 5-1, giving viscosity versus particle concentration at two different shear rates, is given in Figure 5-2. At values of ϕ below 0.1 the curves are coincident, but for $\phi > 0.1$ they diverge. These shear thinning results can be rationalized in terms of structure formation suggested by Hoffman (154, 155). At low shear rate (low Pe), particles are randomly placed by the dominant Brownian motions. They will jam into one another as

they are forced to move in a shear field. When viscous forces prevail, particles moving in layers flow past one another in the direction of shearing with essentially no jamming. Without particle jamming, less energy will be required to induce flow. Therefore, it is reasonable to expect the high shear limit viscosity at 1465 1/s to be lower than the viscosity at low shear rate 73 1/s at high particle concentration. Electrostatic repulsion forces favor the formation of three-dimensional structure while the hydrodynamic forces favor the two-dimensional layered structure. At low particle concentration, ordered layers might not be formed even at high shear rate, due to the insufficient range of electrostatic interaction between particles. Hence, the differences in structure at two different shear rates vanish and the viscosities become indistinguishable.

Figure 5-3 illustrates the effect of temperature on the viscosity profile of cleaned latex A at two particle concentrations. Again, pseudoplastic and high shear Newtonian behavior were observed. Figure 5-3(a) shows that as temperature is increased, viscosity is decreased and less pronounced shear-thinning behavior was found. The decreased viscosity with increasing temperature can be explained by the secondary electroviscous effect, i.e. the corresponding decreased strength and range of electrostatic repulsion forces allow less energy dissipated upon particle contact. While Hoffman's four regime flow mechanism (154, 155) is still capable to account for the flow properties, the possibility of forming ordered layers at high shear is reduced at higher temperature because of the reduced range of electrostatic interaction between particles. Consequently, the degree of shear-thinning became less obvious at elevated temperature and structure difference between low and high shear rate disappeared eventually and Newtonian flow curve was reached at 75°C. As particles were easier to be packed into layers at higher particle concentration, the structure difference between the low and high shear became significant and

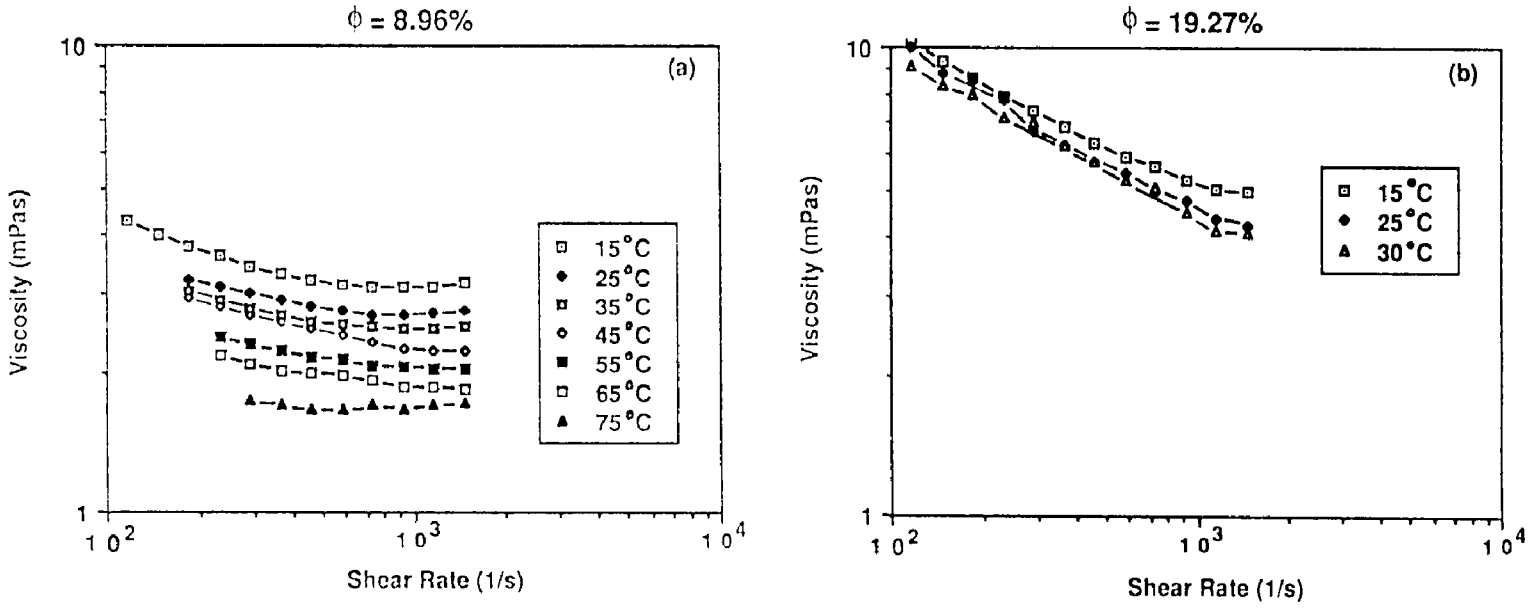

Figure 5-3: *The viscosity profile of cleaned latex A at various temperatures (°C).*

more pronounced shear-thinning was thus seen in Figure 5-4(b). It seems the temperature places less impact on the viscosity of dispersions with higher particle concentration. This can be understood because stronger and more numerous electrostatic interactions at higher particle concentration become less sensitive to the change in temperature.

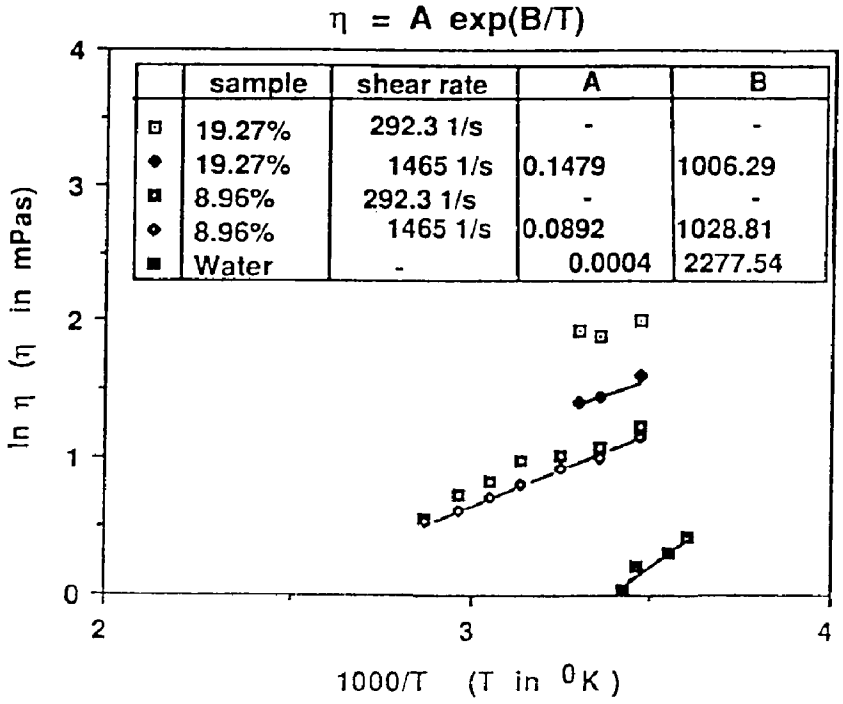

Figure 5-4: *The temperature dependence of viscosity of cleaned latex A at various particle concentrations and shear rates.*

According to the kinetic theory of simple liquids developed by Eyring and coworkers (158), the viscosity follows the Arrhenius equation.

$$\eta = A \exp(B/T) \tag{5.4}$$

where T is the absolute temperature in °K, A is a constant and B represents the activation energy for viscous flow. The quantity B is related to the latent heat of vaporization of the liquid. In order to test the validity of above equation for the latex dispersion system, $\ln\eta$ vs. 1/T with data taken from Figure 5-3 was

plotted in Figure 5-4. Data for water were added for comparison. Surprisingly, a linear relationship was obtained, particularly at high shear rate. This implies that the colloidal dispersions can be theoretically treated as dense liquids. However, physical significance of A and B may be reassigned as follows. Constant A now is a particle packing factor indicating the availability of unoccupied free volume. B is still an enthalpy term relating with the total potential energy of interaction between particles. Parameters A and B can be obtained from the intercept and slope of the linear curve. The results show that A increases with increasing particle concentration due to less space available for particle movement. The reason for the insensitive B values to particle concentration is not known. It is interesting to note that the viscosity of dispersion medium (water) is more sensitive to the temperature than that of colloidal dispersion, probably because of the different relaxation time corresponding to different dimensions of structure units in these materials.

Figure 5-5 shows the effect of salt concentration and valency on the viscosity profile of polystyrene latex A at 25°C. Shear-thinning behavior is observed initially with the addition of electrolyte. But upon increasing the salt concentration further, shear-thickening behavior starts to appear. This dilatancy is attributed to the Brownian coagulation or shear-induced coagulation which results from the addition of excess electrolyte that reduces the height of the potential energy barrier and the shearing action that enhances the average kinetic energy of the particles. The strength of electrostatic repulsion between particles is also very sensitive to the counterion valency of the salt. Indeed, the divalent salt $MgCl_2$ decreases the viscosity to a greater extent, induces coagulation at a lower salt concentration and has a more pronounced shear-thickening behavior than does the monovalent NaCl.

A crossplot of data in Figure 5-5, giving viscosity versus salt concentration

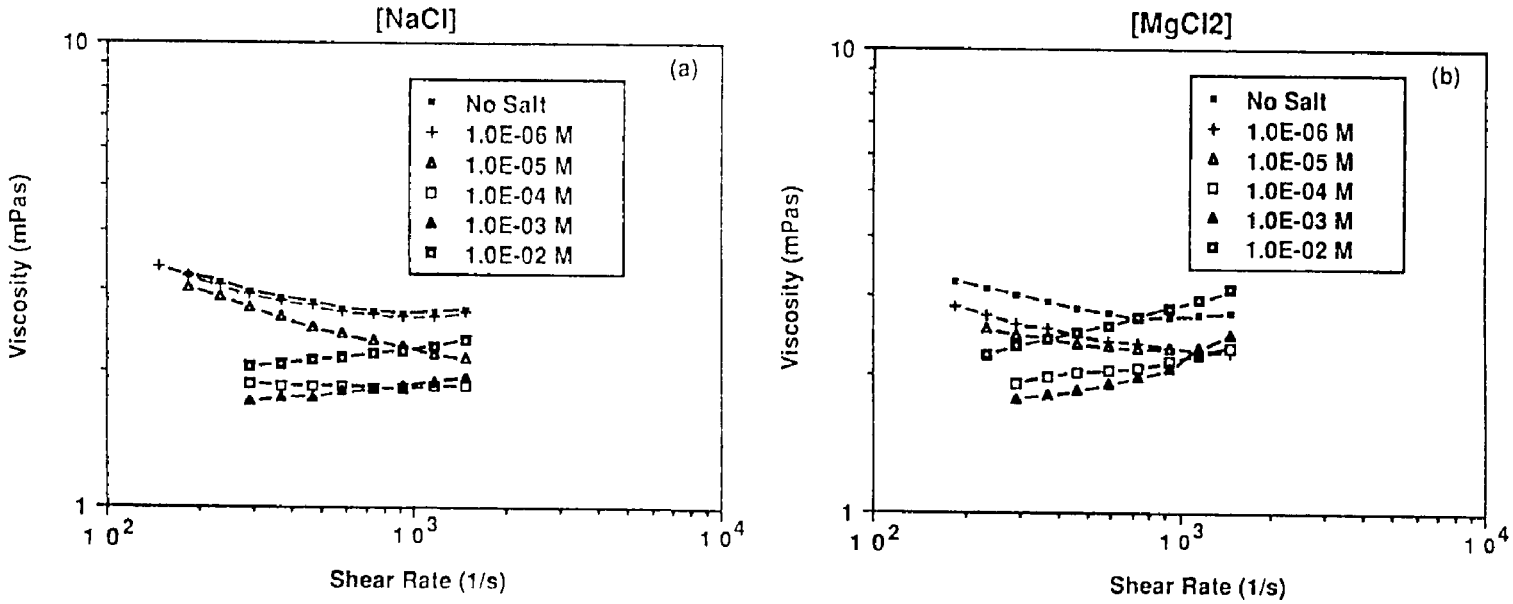

Figure 5-5: *Effect of salt concentration (mole/l) and valency on the viscosity profile of latex A with* ϕ*=8.96% at 25°C.*

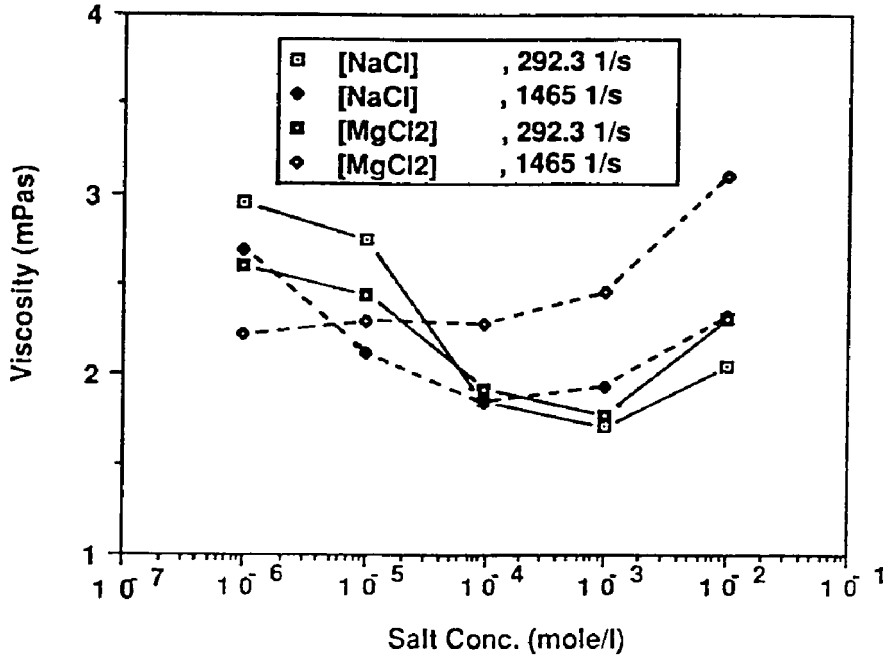

Figure 5-6: *Effect of salt valency and concentration on the viscosity of latex A with ϕ=8.96% at 25°C and various shear rates.*

at two different shear rates, is given in Figure 5-6. A viscosity minimum is observed in every cases except the one with divalent salt $MgCl_2$ and high shear rate 1465 1/s. The viscosity first decreases with increasing salt concentration due to compression of Debye length and reduction of Coulombic repulsion strength. Upon further addition of electrolyte, the interparticle Coulombic forces are effectively screened out and van der Waals attraction comes into play. Brownian or shear-induced coagulation of latex particles thus occurs to give higher viscosity. Higher salt valency and shear rate greatly destabilize the dispersion. Hence, viscosity increases monotonically with electrolyte concentration without observing the minimum. Comparing the data for NaCl at two different shear rates, the viscosity minimum shifts to lower salt concentration with increasing shear rate. The intersection of these two curves

corresponding to two different shear rates displaces toward lower salt concentration with increasing salt valency. Whereas the intersection of two curves corresponding to two different salt valency moves to lower salt concentration with increasing shear rate. All the observations stated above agrees strongly with the DLVO theory for colloidal stability. It is interesting to see that viscosity data for $MgCl_2$ at 292.3 1/s can be superimposed on that for NaCl at 292.3 1/s if considering the equivalent salt concentration but not molarity. This observation is in agreement with Krieger and Eguiluz's (62) finding that the secondary electroviscous effect is a function of equivalent concentration of added electrolyte, changing type or valence of ions has little effect.

5.4.2 Dynamic Oscillation

The viscosity measurements probe the strength of the dispersion microstructure by subjecting samples to relatively large stresses. On the other hand, dynamic and transient techniques are more useful in dealing with the state of dispersion at standing because of the unperturbed structure at small deformations. It is interesting to think of oscillatory measurements as analogous with mechanical spectroscopy as we sweep through a frequency range and look at the frequencies at which the material responds. In infra-red spectroscopy we study the vibration of molecular segments such as an sulfate group or a carboxyl group. In rheology it is the motion of the microstructural units either macromolecules or colloidal particles, as they diffuse in order to relieve the applied stress.

Concentrated dispersions showing multiparticle interactions are systems in which the particle diffusion is restricted. Such dispersions usually display a viscoelastic response upon subjecting to an oscillatory strain (or stress) within a

certain frequency range. This can be understood from a consideration of the relaxation time of such dispersions which become comparable to the time of oscillation, i.e. they have a Deborah number of the order of unity (the Deborah number (De) is the ratio of the relaxation time of the system to the experimental time). The frequency range 10^{-3} - 20 Hz employed in Bohlin Rheometer offers an experimental time scale of 8 x 10^{-3} - 159 seconds which covers the relaxation time of most concentrated dispersions. Typically, storage modulus G' dominates at high frequency and reaches a limiting plateau modulus G(∞) as increasing frequency whereas loss modulus G" prevails at low frequency. This indicates as De>>1 material will behave more like a solid whereas material will perform like a liquid as De<<1. The principle of oscillatory technique and definition of various rheological parameters, such as G', G", $\tan^{-1}$(G"/G') and η', have been presented in the section of experimental. Typical oscillation results of cleaned polystyrene latex A with a volume fraction of 26.97% at 35°C are given in Figure 5-7. G' dominates over G" throughout the frequency range employed. The data also show that logG' and logG" increase linearly with the log frequency according to relationships $G'=13.59(2\pi f)^{0.09}$ and $G''=2.43(2\pi f)^{0.09}$ while the phase shift δ ($\tan^{-1}$(G"/G')) maintains a constant low angle of 10° which indicates this structured dispersion is highly elastic and G' and G" are equally sensitive to the frequency. It is interesting to see that there also exists a power law shear-thinning relationship between dynamic viscosity and frequency analogous to that found between the steady state viscosity and shear rate ($\eta=m(\dot{r})^{n-1}$).

In steady shear the particles are forced to flow past one another and the interaction energy is dissipated. The small amplitude oscillation, however, induces weaker hydrodynamic interactions and maintain the ordered structure. Electrostatic energy is thus stored and generates the observed elasticity in G'. Therefore, one might expect at same shear rate dynamic viscosity η' will be

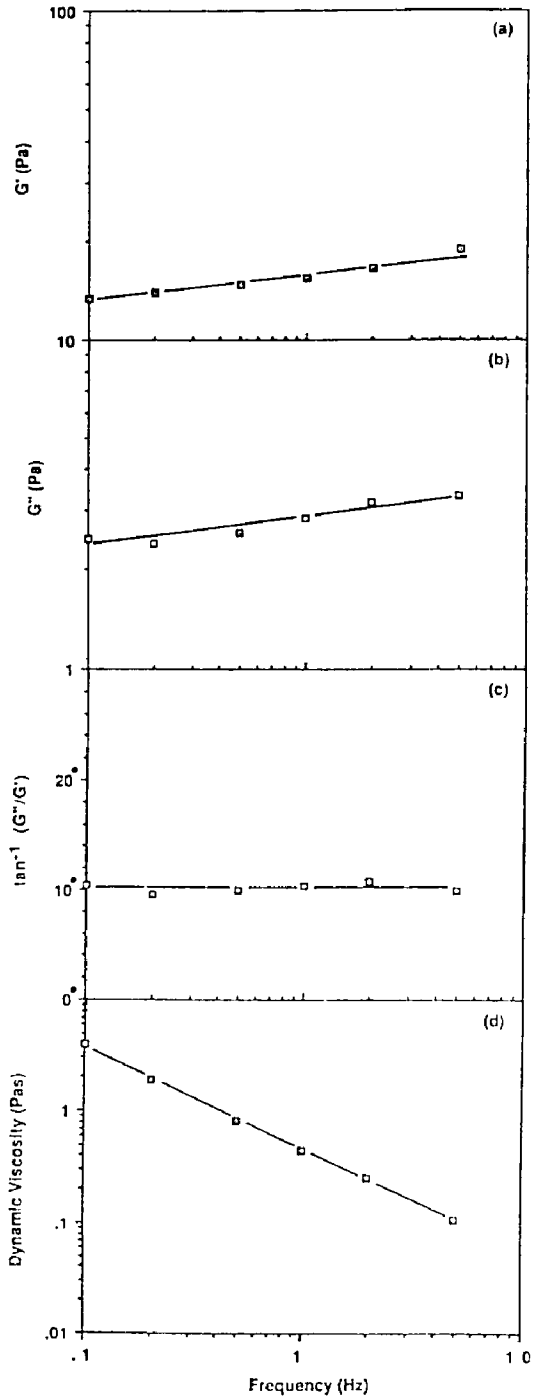

Figure 5-7: *Effect of frequency on the storage modulus G', loss modulus G'', phase shift δ ($tan^{-1}(G''/G')$) and dynamic viscosity η' of cleaned polystyrene latex A with ϕ=26.97% at 35°C.*

significantly lower than steady shear viscosity η. Indeed, Mitaku et al. (64) found the dispersion dynamic viscosity even lower than the viscosity of continuous medium. But the fact that 10° phase shift and finite amount of loss modulus G" appear upon deformation implies the existence of a "weak" ordered structure. Then, it is possible dynamic viscosity η' becomes comparable in magnitude with steady state viscosity η, e.g. 100 mpas of η' from Figure 5-7(d) and 40 mpas of η from Figure 5-1 at shear rate 30 1/s.

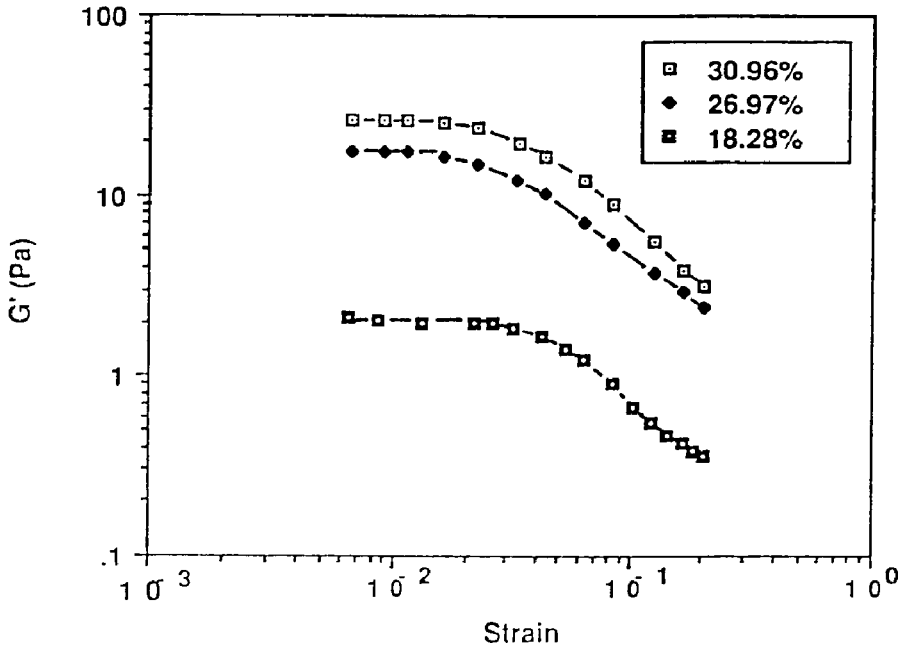

Figure 5-8: *Effect of strain and particle concentration (vol.%) on the storage modulus of cleaned latex A at 25°C and frequency 2 Hz.*

5.4.3 Strain Sweep

Strain sweep is also an oscillation measurement which is carried out at a fixed frequency but at varied strain amplitudes. This test is useful to establish the range of linear viscoelastic behavior where dynamic moduli are independent of the strain amplitude. Figure 5-8 shows the particle concentration dependence of the strain sweep of cleaned polystyrene latex A. It can be clearly seen that G'

remains constant with applied strain ε, until a critical value ε_m is reached above which G' decreases with a further increase in ε. In small amplitude oscillations, the particles never move out ouf their potential well so the electrostatic energy is stored and appears as the elasticity of the dispersion, G'. Above ε_m, the ordered structure is perturbed and the dispersion shows a nonlinear response. G' increases with increasing particle concentration at same strain amplitude because the electrostatic interactions between particles become stronger and numerous. Surprisingly though, the ε_m does not follow the same trend. It is possible that higher volume of continous medium is easier to damp out the oscillation, therefore the dispersion with lower particle concentration can withstand higher strain amplitude and extend the linear G' plateau.

Effect of particle concentration on the storage modulus G', loss modulus G" and phase shift $\tan^{-1}(G"/G')$ of cleaned latex A is illustrated in Figure 5-9. While G' rises sharply, G" has an unexpected mild increase with increasing particle concentration. Higher possibility of having more crystal defects and disordered regions at higher particle concentration might explain the higher dissipated viscous energy which appears as G". For the case of water, the phase shift is 90°. Hence, a dramatic decrease in phase shift from 90° to 3° was observed for latex particle concentration varying from 0 - 31 %. This indicates that the latexes with higher particle concentration behave more like a perfect Hookean elastic body and store most of the electrostatic energy upon deformation.

Figure 5-10 illustrates the temperature dependence of the strain sweep of cleaned polystyrene latex A. The latex dispersion with a lower particle concentration is first examined in Figure 5-10(a). The elasticity (G') of the structured dispersion decreases with increasing temperature (T) due to the corresponding reduction in electrostatic repulsion. It is also seen that a linear

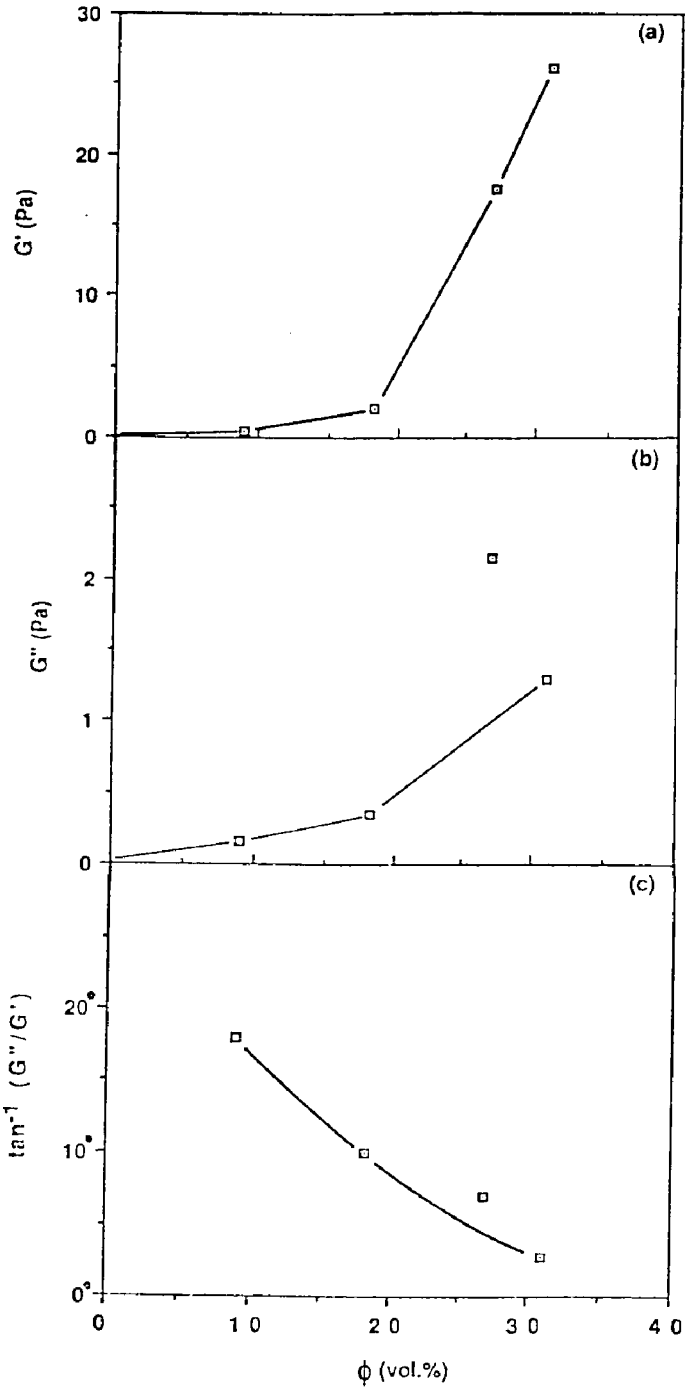

Figure 5-9: *Effect of particle concentration on the storage modulus G', loss modulus G" and phase shift $\tan^{-1}(G''/G')$ of cleaned latex A at 25°C and frequency 2 Hz.*

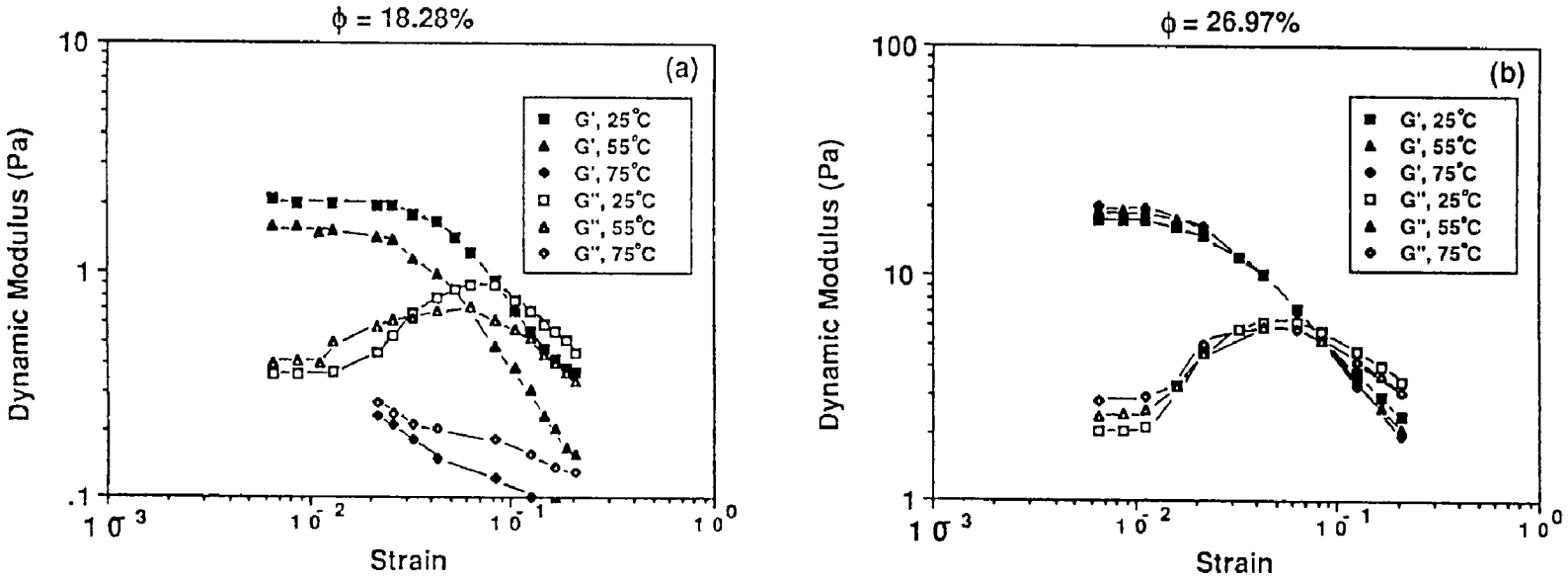

Figure 5-10: *Effect of strain and temperature on the storage and loss modulus of cleaned latex A at frequency 2 Hz.*

viscoelastic plateau can be observed at low temperature as long as the dispersions possess the ordered structure. The elasticity drops dramatically at high temperature since the ordered structure is perturbed by the thermal motion of the particles. This represents a temperature induced order-disorder phase transition, i.e. a melting transition of colloidal crystals. On the other hand, upon increasing the strain (ε) G" shows an initial plateau, climbs up to reach a maximum, then intersects with G' and drops thereafter. G', G" vs. ε behavior resembles G', G" vs. T behavior of polymeric materials. The glass transition temperature interpreted as the onset of long-range, coordinated molecular motion represents the transition point between glassy state and rubbery state of polymeric materials. Whereas the intersection strain (ε_c) between G' and G" of structured latex dispersion indicates a solid-liquid transition point as a result of long range particle diffusion. This interpretation is based on the observation that G' dominates over G" as $\varepsilon < \varepsilon_c$ and G" dominates as $\varepsilon > \varepsilon_c$. It is also found that the strain at which the system gives a nonlinear viscoelastic response (ε_m) for G' is higher than that (ε_n) for G". ε_m decreases with increasing temperature. For the latex dispersion with a higher particle concentration (Figure 5-10 (b)), temperature has less impact on the elasticity and on the ordered structure of the dispersion. No melting transition is observed throughout the temperature range employed.

Figure 5-11 exhibits the effect of temperature on the storage modulus G', loss modulus G" and phase shift $\tan^{-1}(G"/G')$ of cleaned latex A. While G" and $\tan^{-1}(G"/G')$ rise, G' decreases slightly with increasing temperature for the latex with a lower particle concentration. The increased temperature compressed the Debye length, decreased the magnitude of electrostatic repulsion between particles and fueled the Brownian motion of particles. Therefore, the weaker dispersion microstructure results in lower elasticity and more electrostatic

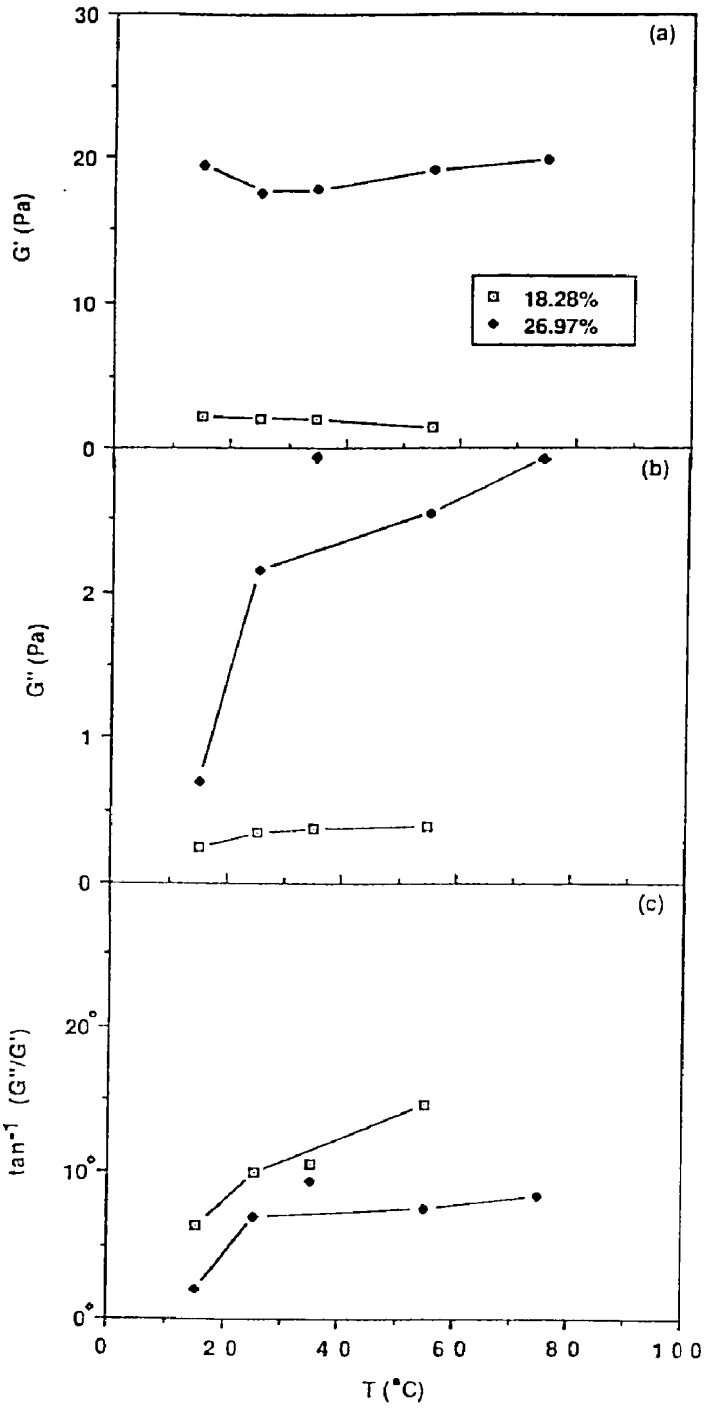

Figure 5-11: *Effect of temperature on the storage modulus G', loss modulus G'' and phase shift $\tan^{-1}(G''/G')$ of cleaned latex A at frequency 2 Hz and various particle concentration (vol. %).*

energy is dissipated. With regard to the latex with the higher particle concentration, an unexpected minimum in G' was observed due to experimental artifact of water evaporation at higher temperature. The particle concentration dependence of G', G" and $\tan^{-1}$(G"/G') agrees with that observed in Figure 5-9.

The salt concentration dependence of the strain sweep of latex A with ϕ=20.70 % at 25°C is shown is Figure 5-12. Linear viscoelastic response was alaways obtained as the applied strain was below 0.02. As may be seen, the various curves at different salt concentrations appear to reach a common horizonal asymptote as strain increases. Zero G' is expected to be obtained eventually upon applying sufficiently large deformation because the ordered structure of dispersion is totally destroyed. G' decreases with increasing salt concentration because of the corresponding reduction in the strength and range of interparticle Coulombic repulsion force. Thermal motions of particle then overcome the suppressed electrostatic repulsion and disintegrate the crystal-like structure of dispersion. Closer examination reveals that within the nonlinear viscoelastic region G' for latex with lower salt concentration decreases at a faster pace with strain than that for latex with higher salt concentration. This can be understood because the structured dispersions become less sensitive to the strain when the dispersions become more disordered at higher electrolyte concentration.

Figure 5-13 illustrates the effect of salt valency and concentration on the storage modulus G', loss modulus G" and phase shift $\tan^{-1}$(G"/G') of latex A. At low added salt concentration, plateau storage and loss modulus were observed because the total ionic strength dominated by the counterion density is constant. With increasing the salt concentration further, the Debye length is significantly compressed, and hence the elasticity originated from electrostatic interactions between particles vanishes accordingly. While the loss modulus G"

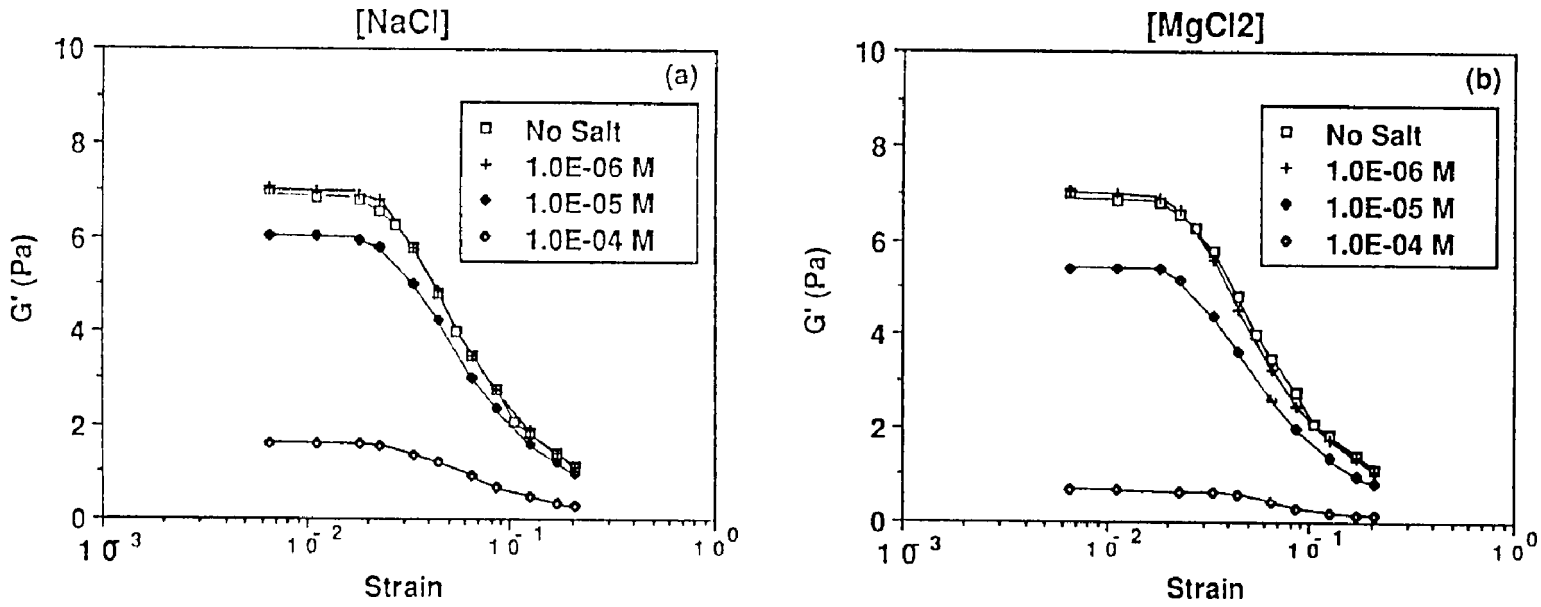

Figure 5-12: *Effect of strain and salt concentration on the storage modulus G' of latex A with ϕ=20.70 % at 25°C and frequency 2 Hz.*

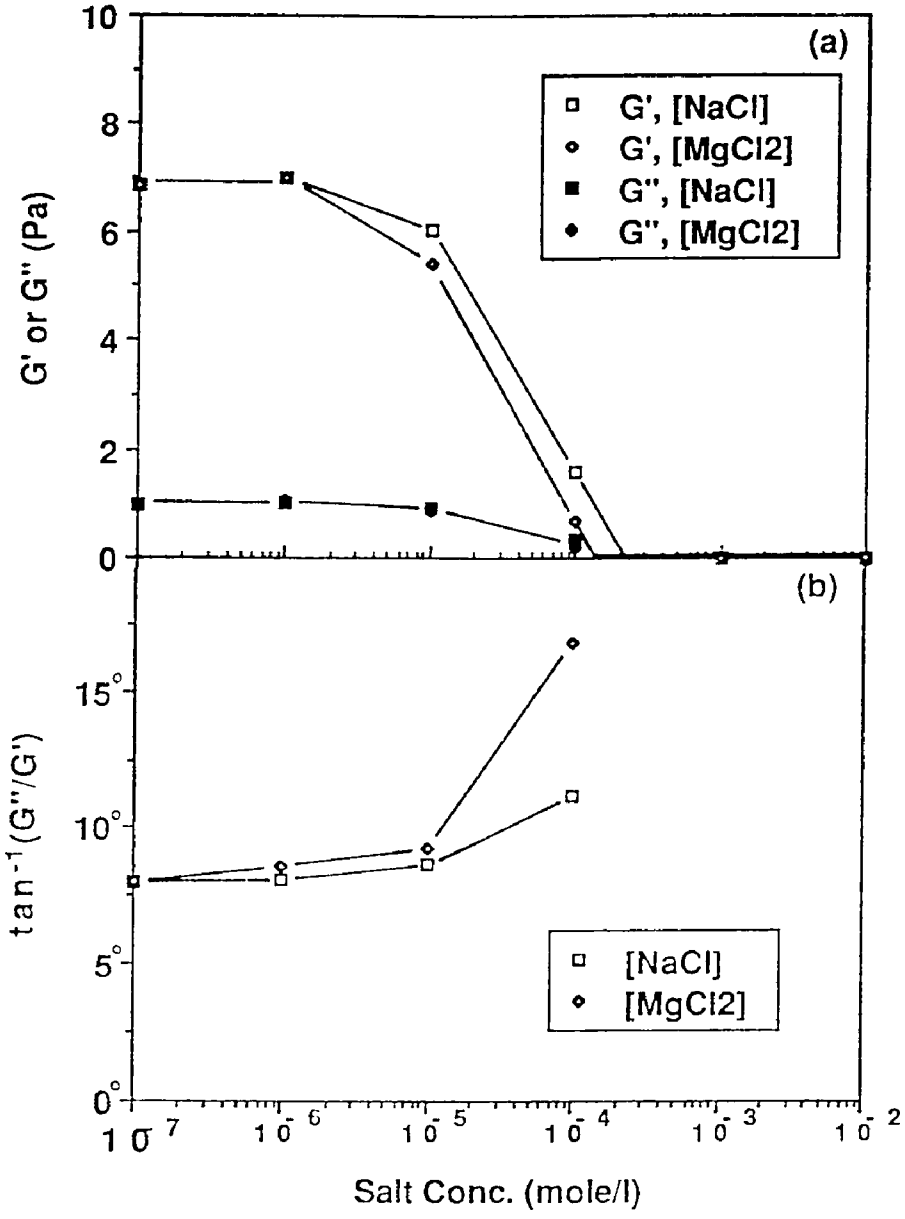

Figure 5-13: *Effect of salt valency and concentration on the storage modulus G', loss modulus G" and phase shift $tan^{-1}(G"/G')$ of latex A with ϕ=20.70 % at 25°C and frequency 2 Hz.*

or dynamic viscosity η' decreases, the phase shift (i.e. ratio between G" and G') increases with increasing salt concentration. The results also show that the divalent $MgCl_2$ decreases the elasticity and increases the phase shift to a greater extent than does the monovalent NaCl. This is because $MgCl_2$ contributes higher ionic strength and suppresses the Debye length more markedly. Once the range of electrostatic interaction falls below the interparticle separation, the elasticity disappears and dispersion becomes disordered. On the other hand, G" does not exhibit significant specificity to salt valency type. What is most interesting is $MgCl_2$ data are superimposed on the NaCl data at the same normality either in the case of G' and G" or $\tan^{-1}(G"/G')$. This indicates that the secondary electroviscous effect produced by two electrolytes is identical at the same equilvalent concentration. Same observation has been attained from the viscosity data in Figure 5-5 of this work and in literature (62). This is really a surprising finding as most of the colloidal properties are sensitive to the valency and nature of the counterions. This also demonstrates that counterions play a bigger role than the coions in determining the colloidal behavior. One mole/l of Mg^{2+} concentration works like two mole/l of Na^+ concentration to screen off part of the particle charge.

5.4.4 Flow Oscillation

Many applications exist where it is crucial to know the structure recovery in a dispersion after steady shearing for a finite time period. Such cases include the levelling and sagging problems in paint application, film formation after high speed printing, etc. Figure 5-14 shows the effect of shearing strength on the flow oscillation of cleaned polystyrene latex A with a volume fraction of 26.97 % at 15°C. G' increases while G" and δ drop as a function of time elasped after shearing. All these changes indicate a gradual recovery of the crystal-like

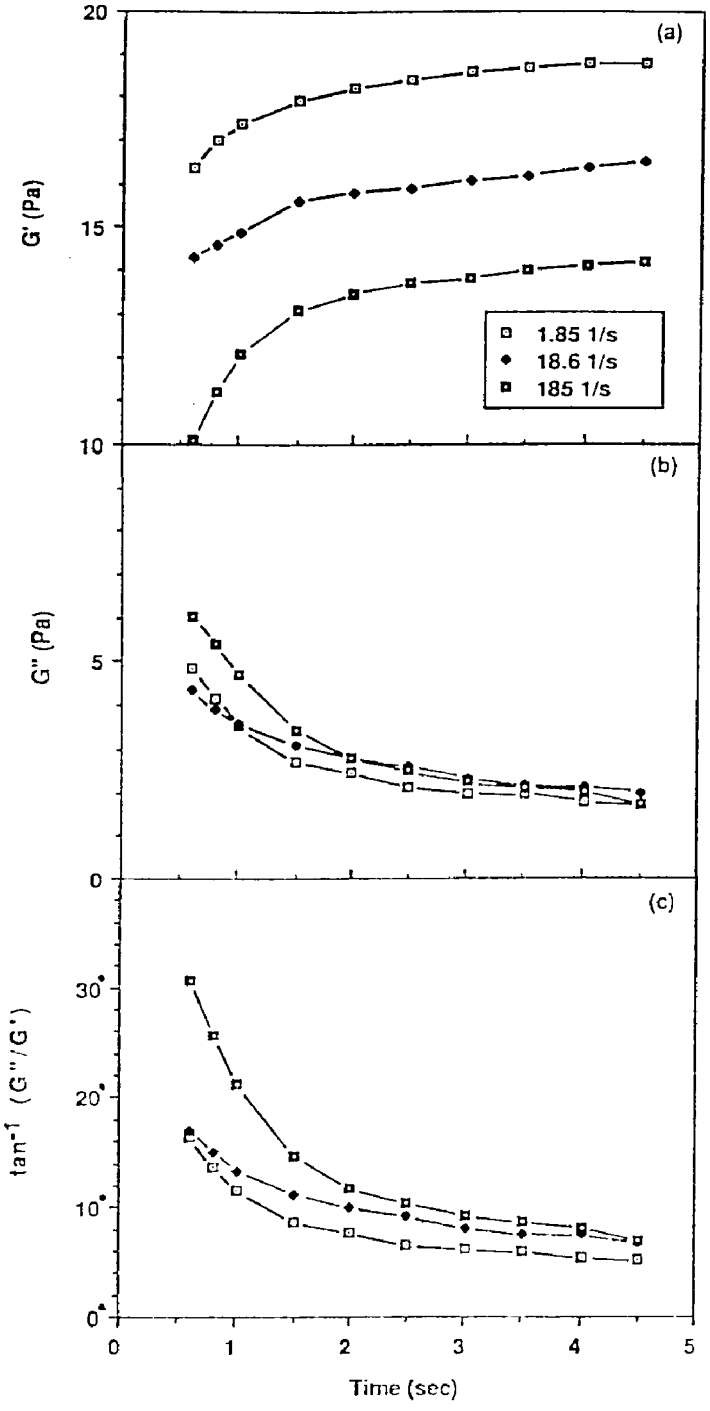

Figure 5-14: *The oscillation at frequency 2 Hz after steady shearing for 1 sec of cleaned latex A with ϕ=26.97 % at 15°C.*

structure of the latex dispersion. The more rigorous the shear is, the more the ordered structure is perturbed, and hence the less elastic the dispersions become. Therefore, G' decreases while G" and δ increase with increasing shear rate. It is expected that G', G" and δ obtained at different shear rates will converge eventually after waiting long enough. It seems that this flow oscillation technique has potential to be an important tool for studying the kinetics of crystallization of the structured latex dispersion.

5.4.5 Stress Relaxation

The three possible stress relaxation processes which exist in the latex dispersion include relaxation due to movement of water molecules, relaxation of the ionic cloud surrounding the particles and the relaxation caused by particle diffusions. The last process is much slower than the rest, so the rate controlling step is the particle motion. The effect of temperature and particle concentration on the stress relaxation and relaxation spectra of cleaned polystyrene latex A is illustrated in Figure 5-15. Figure 5-15(a) exhibits the decayed stress vs. time upon applying a small, constant strain. It indicates that with a short time scale (i.e. at a very high frequency), the characteristic time of the deformation was much shorter than that of microstructural rearrangement, so the ordered dispersion stored the energy, and the plateau glassy modulus Gg was observed. As a matter of fact, Gg is equal to $G(\infty)$, the storage modulus measured at an extremely high frequency in the oscillation experiments. Above correlation is supported by the following examples. 17.5 Pa of relaxation modulus measured at 0.08 sec (i.e. 2 Hz) for cleaned latex A with ϕ=26.97 % at 35°C is close to 17.0 Pa of storage modulus at frequency 2 Hz obtained from Figure 5-7. Also, it is noted that the predicted storage modulus 20.6 Pa at frequency 16 Hz by empirical equation $G'=13.59(2\pi f)^{0.09}$ attained from Figure 5-7 agrees

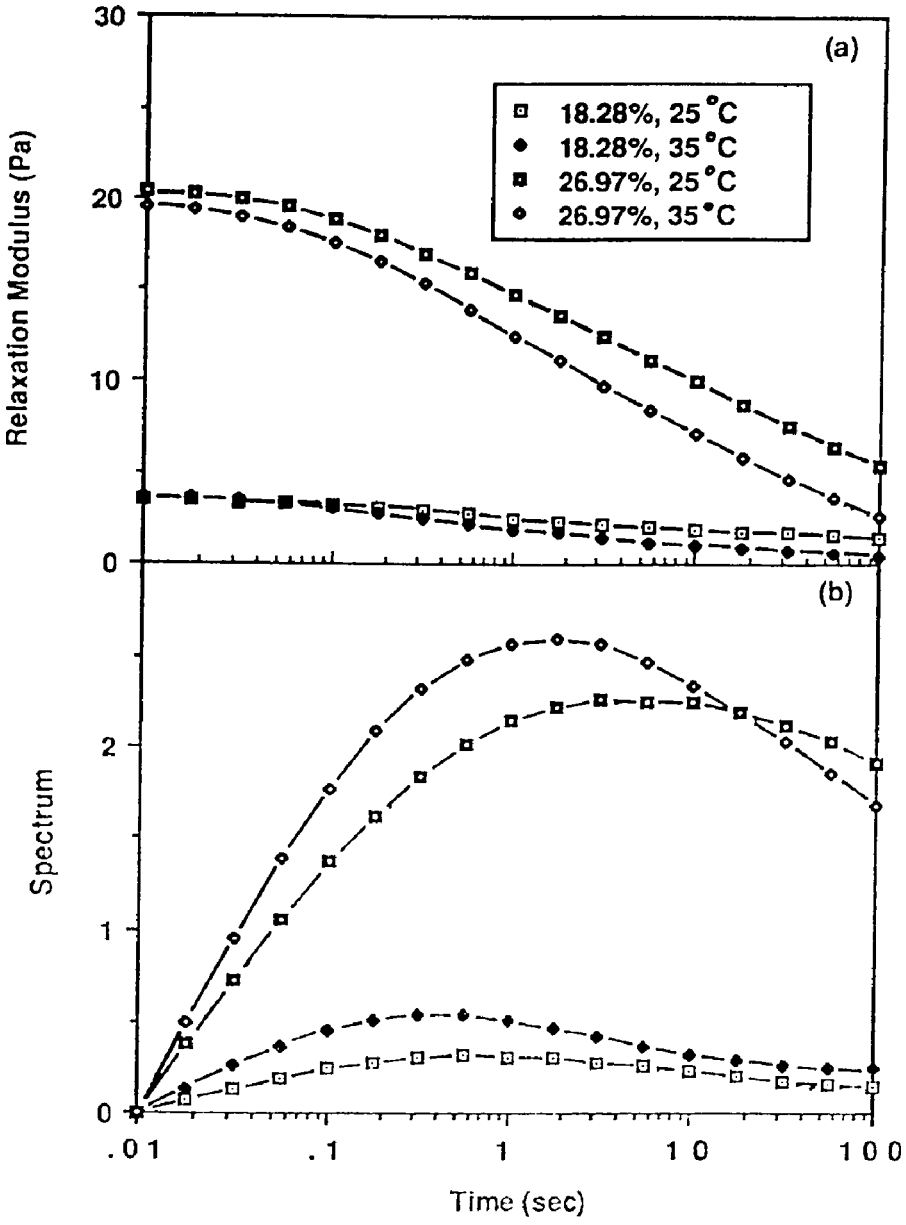

Figure 5-15: *Effect of temperature and particle concentration on the stress relaxation and relaxation spectra of cleaned polystyrene latex A.*

satisfactorily with the relaxation modulus 19.6 Pa measured at 0.01 sec.

If one viscoelastic function is known over a wide range of time or frequency, then in principle any other viscoelastic function can be derived using

exact transformation equations given by the mathematical theory of linear viscoelasticity (152). The exact interrelations among viscoelastic functions include:

$$G'(\omega) = Ge + \omega\int_0^{\infty}[G(t) - Ge]\sin\omega t\, dt \quad (5.5)$$

$$G''(\omega) = \omega\int_0^{\infty}[G(t) - Ge]\cos\omega t\, dt \quad (5.6)$$

$$G(t) = Ge + \int_{-\infty}^{\infty} H(\lambda)\exp(-t/\lambda)\, d\ln\lambda \quad (5.7)$$

where Ge, equilibrium modulus (at long time), ω, the angular frequency ($\omega=2\pi f$), t, time, λ, relaxation time, G(t), relaxation modulus and $H(\lambda)$, relaxation spectrum. The empirical equation to represent the stress relaxation modulus was proposed by Smith (159).

$$G(t) = Ge + \frac{(Gg - Ge)}{[1+(t/t_0)]^{1-m}} \quad (5.8)$$

Where Gg, glassy modulus (at short time), t_o and m, positive empirical constants. This equation was found to fit G(t) data in Figure 5-15(a) very well. For example, equation with Gg=19.6 Pa, Ge=0, m=0.57 and t_o=1.00 well represents the experimental data for cleaned latex A with ϕ=26.97 % at 35°C. Upon substituting equation (5.8) into equation (5.7) and taking inverse Laplace transform, $H(\lambda)$ can thus be obtained (159). The integrals in equations (5.5) and (5.6) can also be perfomed numerically or graphically since the starting function G(t) has been expressed in analytical form. G' and G'' thus obtained can then be compared with experimental data. The above mathematical exercise enables one to test the applicability of linear viscoelastic theory on structured latex dispersions. Such important research area deserves further attention.

Based on the concept that electrostatic interactions dominate the stress relaxation behavior of the ordered structure by slowing the long rang diffusive motion of the particles, a broad spectrum of relaxation processes will be expected to occur. Indeed, Figure 5-15(b) shows the distributions of relaxation time for the ordered dispersions. A shorter characteristic (peak) relaxation time is obtained with lower particle concentration or higher temperature. This is

anticipated since the structured dispersions under the same conditions become less elastic due to the decreased strength and range of electrostatic repulsion force between particles. Same particle concentration dependence of the most frequently occurring relaxation time has been reported by Goodwin, et al. (77). Neither Maxwell Element (152) nor Four-Element model (combination of Maxwell and Voigt Element in series) was found to successfully describe the viscoelastic behavior of the ordered dispersions, such as G(t), G' and G". This is not surprising since limited number of relaxation time attained from these models contradicts with what is observed in Figure 5-15(b). Hence, it is expected that generalized Maxwell model (Maxwell elements in parallel) (152). will better account for the broad relaxation spectrum. Thus, if there are n Maxwell elements,

$$G(t) = \sum_{i=1}^{n} Gi \exp(-t/\lambda i) \tag{5.9}$$

where Gi, shear modulus for spring, ηi, viscosity for dashpot, λi, relaxation time of the element defined as $\eta i/Gi$. For a viscoelastic solid, one of the relaxation times must be infinite and the corresponding modulus contribution is Ge, the equilibrium modulus. Whereas for a viscoelastic liquid, Ge=0.

The order of magnitude of $G(\infty)$ or Gg may be written in terms of the magnitude of the thermal fluctuation, δ, of a particle around the crystal lattice point as

$$Gg \cong \frac{f}{b} \cong \frac{(kT/<\delta^2>)}{b} \tag{5.10}$$

where f is the force constant of particle, b is the unit lattice constant, k is the Boltzmann constant, and T is the absolute temperature. Previous optical study in Chapter 4 has shown that the ordered dispersions with high particle concentrations possess the fcc (face-centered cubic) crystal structure. Since four particles per unit cell is known for fcc crystal, if $<\delta^2>^{1/2}/b$ is replaced by a dimensionless parameter β, we obtain the elastic modulus as a linear function of

number density (N) of particles,

$$Gg \equiv \frac{NkT}{4\beta^2} \tag{5.11}$$

Lindemann's law of crystal melting (160) tells that $\beta<0.1$ for a stable crystal. Equation (5.11) gives the β values as 0.09 and 0.05 for cleaned latex with particle volume fraction 18.28 % (2.76×10^{13} cm^{-3}) and 26.97 % (4.07×10^{13} cm^{-3}) at 25°C, respectively. The anticipated $\beta>0.1$ for $\phi<15\%$ indicates that ordered latexes with lower particle concentrations are vulnerable to elevated temperature and excess electrolyte, and are easily perturbed to become disordered. β represents the degree of particle fluctuation away from the lattice point and is a measure of strength of electrostatic interactions between particles. Overlooking the finite number of particles per unit cell results in higher β values as were found in Mitaku (66) and Okubo's (88) work.

5.4.6 The Comparison Between Experimental and Theoretical Shear Modulus

The theoretical shear modulus of ordered latexes has been derived from the increase in electrostatic energy caused by a small shear strain to a structured dispersion in previous section. In this analysis, high frequency deformation did not allow a measurable relaxation to occur and only nearest neighbour interactions using pairwise additivity approach were considered. The analytical expression for high frequency limiting storage modulus $G(\infty)$ has been shown in equations (5.2) and (5.3). The second term in $G(\infty)$ equations which accounts for the contribution from the short range van der Waals attraction is negligibly small, whereas the first term which represents the contribution from the long range electrostatic repulsion between particles dominates in the ordered latex system.

The study by reflection spectrophotometry in Chapter 4 has indicated that the ordered latexes with high particle concentrations possess the fcc (face-

centered cubic) crystal structure. The nearest interparticle distance R can thus be obtained from the equation $(R/2a)^3=0.74/\phi$ by knowing the particle concentration. The geometric factor α can calculated as 0.8325 with the information of $\phi_m=0.74$ and n=12.

In dealing with the concentrated latex dispersion, a correction to the Debye length ($1/\kappa_o$) has to be made by considering the increased counterion density and the decreased liquid volume due to the presence of particles (96). Therefore, the corrected Debye length ($1/\kappa$) is shorter than $1/\kappa_o$ corresponding to the added salt alone. The corrected Debye length can be expressed as below:

$$(a\kappa)^2 = (1/1-\phi)[(a\kappa_o)^2+3\phi(1+a\kappa_o)(e\psi_d/kT)] \quad (5.12)$$

The first term (1/1-ϕ) accounts for the reduction in liquid volume by the increase in particle concentration. The second term $(a\kappa_o)^2$ accounts for the effect of added electrolyte. The third term $[3\phi(1+a\kappa_o)(e\psi_d/kT)]$ represents the effect of counterion density.

Zeta potential, ζ, obtained from the microelectrophoresis measurements at infinite dilution was used to approximate ψ_d in calculating $1/\kappa$ under given conditions. Shear moduli thus obtained deviate one or two order of magnitude from the observed Gg. This indicates that the stern potential used for this calculation might not be realistic. In order to determine an appropriate ψ_d value, Gg as measured from the stress relaxation experiments in Figure 5-15 was plotted against $G(\infty)/\psi_d^2$ as calculated from equation (31), in Figure 5-16. A value of ψ_d=16.5 mv could be obtained from the slope of the linear plot by making an assumption of constant stern potential.

Comparison of the shear modulus from experiment and theory can be made now since every needed parameter for equations (5.2) and (5.3) is known. Before doing that, one extra note has to be made. What has been measured experimentally is the storage modulus G' at a frequency of 2 Hz which

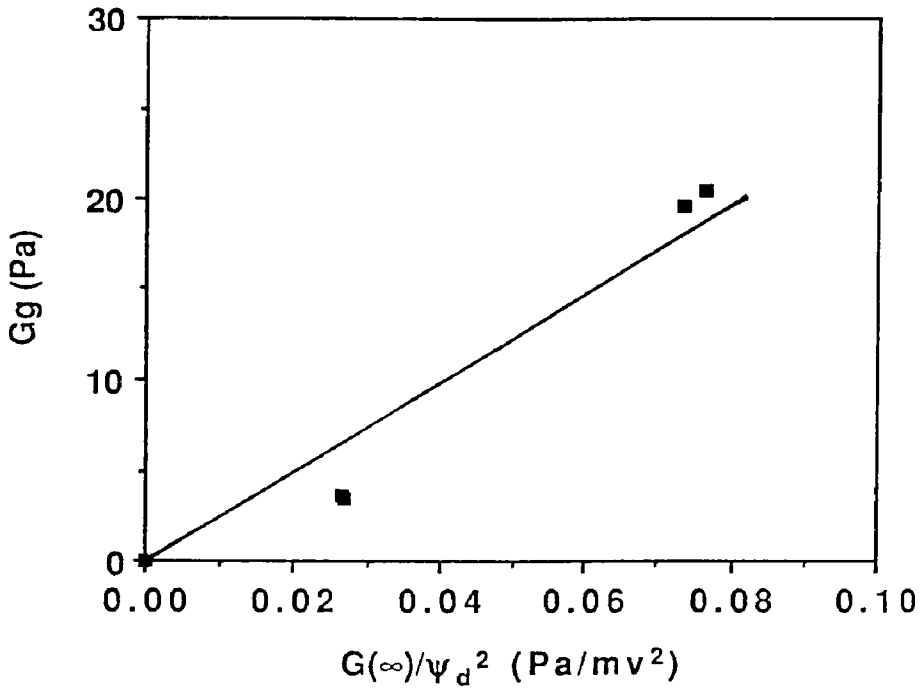

Figure 5-16: *Plot of the experimental glassy modulus, Gg, against the calculated* $G(\infty)/\psi_d^2$.

corresponds to the relaxation modulus obtained at a time scale of 0.08 sec. It is obvious from Figure 5-15(a) that a value for G' at 2 Hz should be a little below, but close to, the value of Gg (i.e. G(∞)).

Figure 5-17 illustrates the effect of sodium chloride concentration on the elastic modulus of latex A with ϕ=20.70% at 25°C and displays the comparison between experimental G' at 2 Hz with theoretical G(∞). The range and strength of double-layer interactions is reduced by the addition of electrolyte, so the shear modulus is expected to decrease with increasing salt concentration. At low NaCl concentrations, a plateau modulus was seen because the total ionic strength dominated by the the counterion density (3rd term in equation (5.12)) is constant. Upon further addition of salt, the foreign electrolyte (2nd term in equation (5.12)) in conjunction with counterions control the ionic strength and

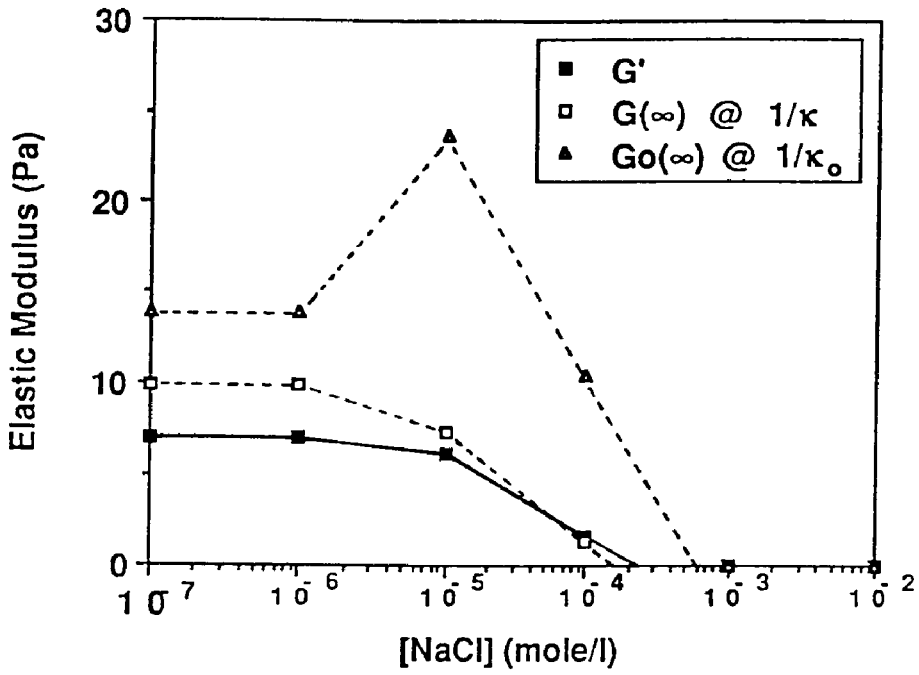

Figure 5-17: *Effect of salt concentration on the elastic modulus of latex A with ϕ=20.70% at 25°C; G' at 2 Hz: experimental storage modulus; G(∞), $G_o(\infty)$: theoretical high frequency limiting modulus calculated by using corrected and uncorrected Debye length, respectively.*

compress the Debye length, and hence the elasticity caused by the electrostatic interactions between particles attenuates accordingly. Finally, no elasticity was detected at high salt concentrations. The predicted G(∞) based on the corrected Debye length agrees nicely with the experimental G'. However, failing to recognize the effect of counterions on Debye length leads to incorrect predictions as shown by the maximum. From now on, the theoretical G(∞) will be calculated by applying the corrected Debye length.

The effect of salt valency on the elastic modulus is shown in Figure 5-18. Divalent salt $MgCl_2$ contributes higher ionic strength, suppresses the electrical double layer, reduces the Coulombic interparticle force, and hence decreases the elasticity more significantly than does the monovalent NaCl. The theoretical

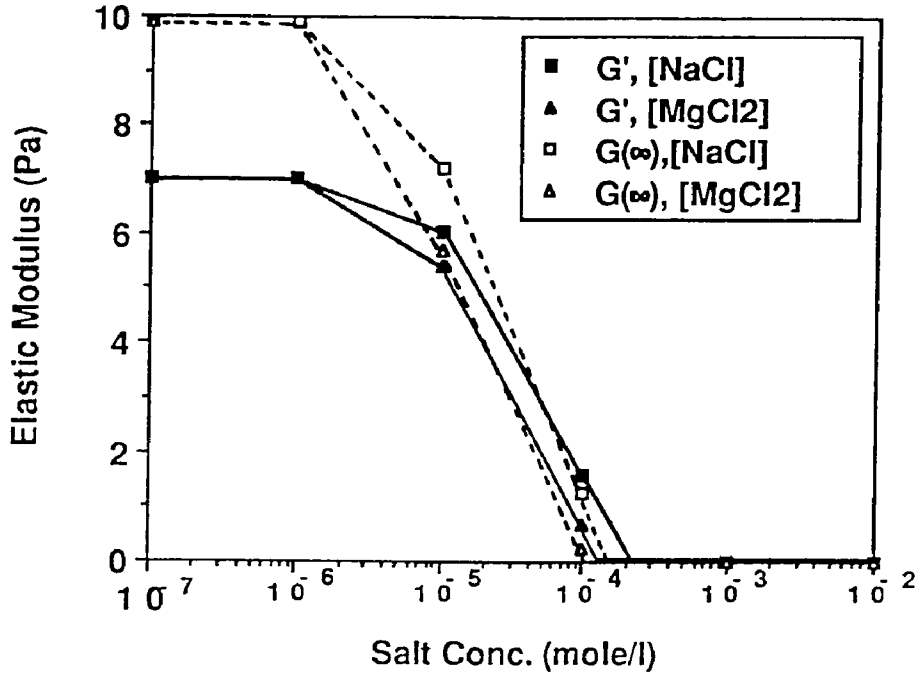

Figure 5-18: *Effect of salt valency on the elastic modulus of latex A with ϕ=20.70% at 25°C; G' at 2 Hz: experimental storage modulus; G(∞): theoretical high frequency limiting modulus.*

G(∞) agrees not only qualitatively but also quantitatively with the experimental G'.

Figure 5-19 exhibits the effect of temperature on the elastic modulus of cleaned latex A. The increased temperature reduces the Debye length, decreases the magnitude of electrostatic repulsion, imposes rigorous thermal particle motions and therefore lowers the elasticity. Experimental artifact of water evaporation results in the climb-up of G' at higher temperature for latex with higher particle concentration. Again, theoretical G(∞) follows satisfactorily with the experimental G'.

The effect of particle concentration on the elastic modulus of cleaned latex A at 25°C is illustrated in Figure 5-20. Elasticity rises sharply with increasing particle concentration because the electrostatic interactions become stronger

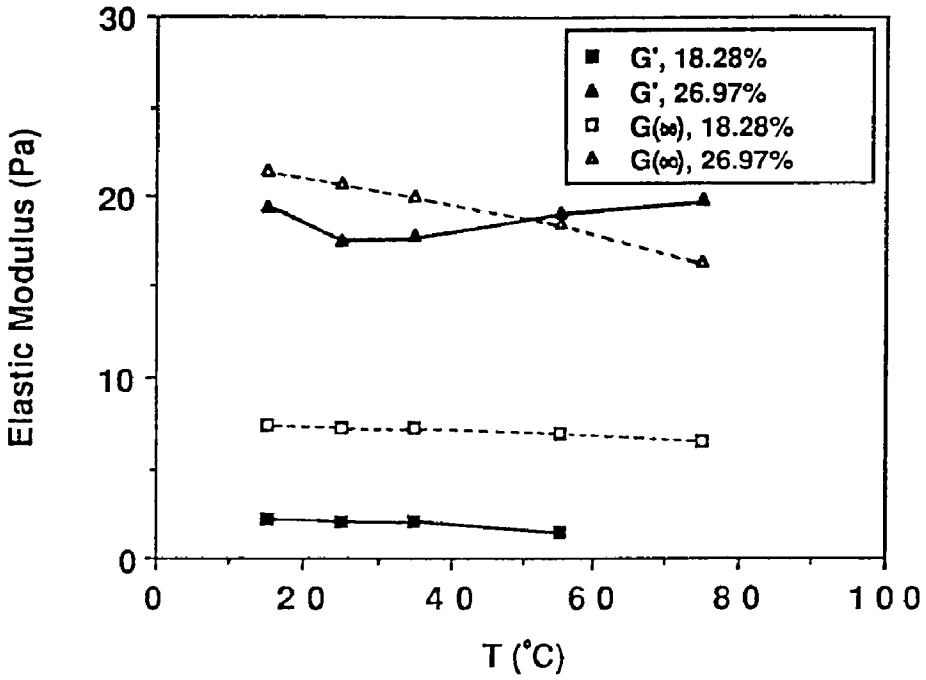

Figure 5-19: *Effect of temperature on the elastic modulus of cleaned latex A at various particle concentrations (vol. %); G' at 2 Hz; experimental storage modulus; G(∞): theoretical high frequency limiting modulus.*

and more numerous. Once again; the predicted G(∞) agrees with the experimental data not only in trend but also in magnitude. An increase in particle concentration causes a decrease in particle separation. The interparticle distance can also be adjusted by varying the particle size while keeping the particle concentration constant. From the equation (5.2) and (5.3), it lead us to believe that shear modulus of ordered latexes will decrease with increasing particle size for a given particle concentraiton.

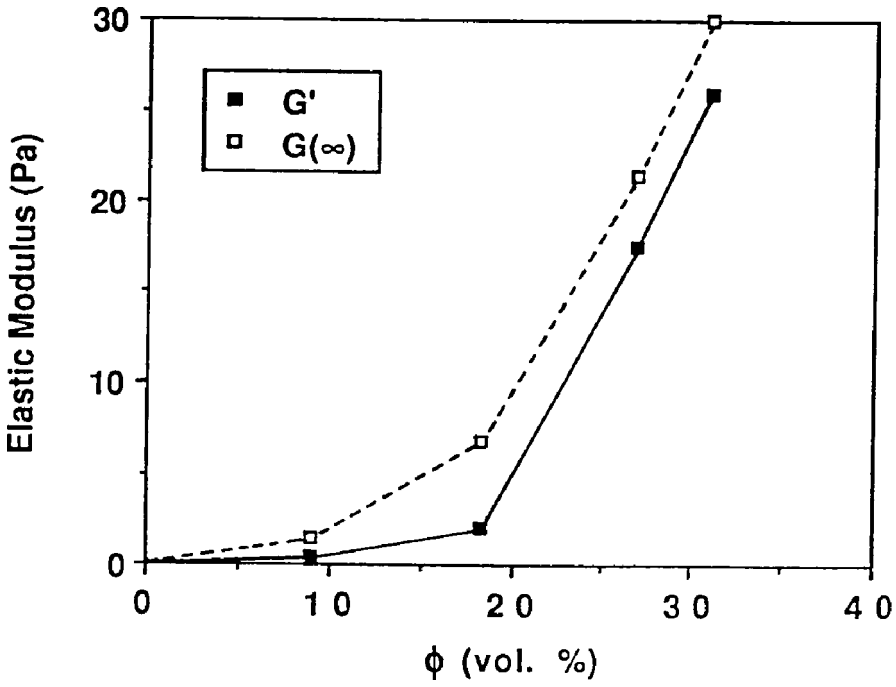

Figure 5-20: *Effect of particle concentration on the elastic modulus of cleaned latex A at 25°C; G' at 2 Hz; experimental storage modulus; G(∞): theoretical high frequency limiting modulus.*

Chapter 6
THE ORDER-DISORDER PHASE TRANSITION

6.1 INTRODUCTION

The monodisperse latex suspensions are frequently observed to be disordered at low particle concentration, high temperature or high salt concentration, as were demonstrated in Chapter 4 and 5 by the vanishing reflection peak and elastic modulus in the optical and rheological study, respectively. These disordered systems display milky white in color. Whereas the ordered, crystalline dispersions Bragg-diffract visible light and exhibit opalescence because the average interparticle distance is comparable to the wave length of visible light. The types of phase transition discussed in this chapter are of interest in many disciplines. For example, understanding of phase stability is important in the process of colloidal consolidation for high technology ceramics (40). Order-disorder phase transition of colloidal dispersions resembles the solid-liquid transition of atomic systems. Moreover, colloidal phase transitions have been widely observed in biological systems (103).

The experimental efforts to construct the phase diagram of monodisperse latexes have been shown by few investigators. Hachisu et al. (32) mapped out the particle volume fraction-electrolyte concentration phase diagram by visual observation of iridescence. The phase boundaries define three regions, each representing the states of the ordered and disordered structures and the state of coexistence of the two structures, respectively. In the coexistent state, the ordered structure separates out as an iridescent sediment while the disordered structure remains as a white supernatant. They attributed this phase

separation to the Kirkwood-Alder transition in a hard sphere system (107). Non-aqueous dispersions (33) and aqueous latexes of high salt concentration being stabilized with nonionic surfactant (4) were employed to simulate hard spheres in order to verify above postulation. Their results are in good agreement with Alder, Hoover and Young's (161) prediction that the phase transition starts at about 0.5 particle volume fraction and is completed at about 0.55 volume fraction of hard sphere. Fujita and Ametani (50) established the phase digram by a titration method. This method suffers the disadvantage of not revealing the coexisting phase domain since the end point of the titration is always on the phase boundary across which the completely disordered state will begin. Monovoukas and Gast (41) quantified the order-disorder and crystal structure transition (bcc-fcc) phase diagram at low ionic strengths by examining the Kossel patterns of light diffraction. The phase diagram for 0.091 μm polystyrene spheres in 0.9-methanol-0.1-water (by volume) dispersion as a function of particle density and HCl concentration was determined by a small angle, synchrotron X-ray scattering technique (55). The liquid, fcc and bcc solid phases were found along with fcc + bcc coexistence and a glass phase at high particle concentration ($\phi > 20$ %). It is also shown that long-range electrostatic interactions (low particle density and electrolyte concentration) favor bcc whereas short-range interactions favor fcc structure.

To date, several attempts have been made to account theoretically for the phase transition of monodisperse latexes. Both exact and approximate methods in statistical mechanics has been used to obtain the phase equilibrium properties of a colloidal dispersion with a given potential of mean force. Snook and van Megen (47-49, 106) applied Monte Carlo approach, first-order perturbation theory and the cell model, respectively, to determine the phase transition in hydrophobic colloids. They found the particle volume fraction at

which the phase transition occurs decreases as the particle size decreases. Although approaches of this kind reasonably predict the onset of ordering, they fail to account for the coexistence regime. Recently, Kremer, Robbins and Grest (162) calculated the order-disorder and the bcc - fcc boundaries from molecular dynamics simulations. They reported that the transition from fcc to bcc with increasing temperature is a result of a higher entropy in the bcc phase. Chaikin et al. (37) examined the internal energy and free energy difference between two phases, took into account the temperature dependent dielectric constant of dispersion medium and found the high entropy phase occurs upon either heating or cooling from the more-ordered phase. This trend has not been experimentally confirmed. Shih, Aksay and Kikuchi (46) have determined the phase diagram by directly comparing the Helmholtz free energies of different phases at the same parameters and by treating the ordered phase as Einstein oscillators and the disordered phase as a hard sphere fluid. By using a Debye-Huckel screened interparticle potential with correction for finite particle size, they found that for particles with low surface charge only the fcc phase is observed while the bcc phase forms at very low particle concentration for systems with higher charge, with the fcc stable at higher particle concentrations. Another approach on casting colloidal order-disorder transformations is in terms of Kirkwood-Alder transition (107) by specifying effective hard sphere diameters which take into account either the Debye length ($1/\kappa_0$) (51) or the radial distance at which the pair potential has a preselected value (such as magnitude of thermal energy) (34).

Analytical calculations on the order-disorder phase transitions have been performed using very limited experimental data and only a few authors have mapped out the phase diagrams by themselves. In this work, the conditions (such as particle concentration, temperature, and salt valency and

concentration) for the occurrence of ordered and disordered structures have been studied systematically. The experimental phase transition conditions established in the previous optical (Chapter 4) and rheological (Chapter 5) studies are then compared with the theoretical calculations based on either the Kirkwood-Alder transition theory coupled with hard sphere concept or the thermodynamics (6). Above theories of phase transition will be explained in details in the next section. The ordering mechanism and the driving forces for order-disorder phase transition under various conditions will also be thoroughly examined.

6.2 THEORY OF ORDER-DISORDER PHASE TRANSITION

6.2.1 Kirkwood-Alder Transition Theory and Hard Sphere Model for ϕ-[Salt] Phase Diagram

Kirkwood (163) in 1939 studied the molecular distribution in liquids and found that a hard sphere assembly would undergo a phase transition from a disordered, fluid-like structure to an ordered, solid-like structure at a volume fraction well below the one corresponding to the closest packing. Alder and Wainwright (164, 165) verified the Kirkwood's speculation by molecular dynamics computations. The subsequent theoretical work then established the range of volume fractions where the two phases coexist at roughly 0.5 to 0.55 (107). Wadati and Toda (31) has further pointed out the colloidal phase transition is an evidence of existence of Kirkwood-Alder transition in nature. Assuming "hard sphere" potential for pair interaction between particles is an approximation in the case of electrostatically stabilized dispersion because the colloidal forces can modify the hard sphere interaction in following manners: first, the Coulombic repulsion force increases the "effective" diamether of particles; secondly, the combined forces of electrostatic repulsion and van der

Waals attraction often "soften" the interaction potential. Nevertheless, hard sphere model provides a useful conceptual basis to understand the phase transition phenomena of colloidal dispersions.

In the present analysis, monodisperse spherical latex particles will be regarded as "effective hard spheres" whose size is determined by the thickness of the electrical double layer. Russel (96) has made a correction to the Debye length by considering the increase in the counterion density and the reduction in the fluid volume with increasing particle concentration. Effective hard sphere which includes either uncorrected ($1/\kappa_o$, see equation (3.1)) or corrected Debye length ($1/\kappa$, see equation (5.12)) will both be examined in this work. Figure 6-1 illustrates schematically the effective hard sphere concept.

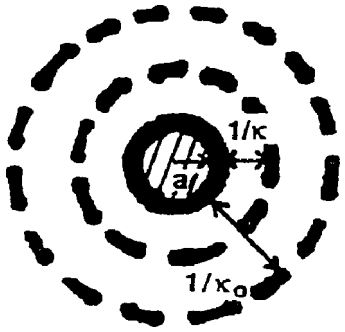

Figure 6-1: *The schematic representation of effective hard sphere concept.*

The Kirkwood-Alder transition theory (107) has located the melting and freezing point of the hard sphere assembly. Therefore, prediction of the order-disorder transition requires recognizing that there exists a solid state when

$$\phi_{eff} = \left(\frac{a + \frac{1}{\kappa}}{a} \right)^3 \phi_s = \left(1 + \frac{1}{\kappa a} \right)^3 \phi_s \geq 0.55 \tag{6.1}$$

and a fluid state when

$$\phi_{eff} = \left(\frac{a + \frac{1}{\kappa}}{a} \right)^3 \phi_l = \left(1 + \frac{1}{\kappa a} \right)^3 \phi_l \leq 0.50 \tag{6.2}$$

Combining equations (3.1), (5.12) and (6.1)-(6.2),the isothermal phase diagrams

as a function of particle volume fraction and salt concentration can be constructed with the assumption that the zeta potential obtained from electrophoretic measurement approximates the stern potential of latex particle.

6.2.2 Thermodynamics for T-ϕPhase Diagram

A proper theory for crystal melting would invoke the equality of free energies of the two phases (ordered and disordered dispersion in this case) in equilibrium. Williams et al. (6) applied above thermodynamics concept and developed a simple model which accounts for the concentration dependence of the observed melting transition. Following their treatment but with deeper appreciation, phase diagram as a function of temperature and particle concentration can be constructed. The brief mathematical derivations for this model are presented as following.

The temperature at which a first-order phase change occurs is determined by the condition $\Delta F=0$, i.e. by the diminishing free energy difference between two phases. The melting temperature T_m is thus euqual to $\Delta H/\Delta S$, where ΔH is the heat of melting and ΔS is the entropy change.

The entropy of the ordered phase is very small and is assumed to be zero. The entropy change ΔS can be estimated as

$$\Delta S = Nk\,[\phi^{-1}\,ln\phi^{-1} - (\phi^{-1}-1)\,ln(\phi^{-1}-1)] \tag{6.3}$$

where N is number of spheres in the dispersion, k is Boltzmann's constant and ϕ is particle volume fraction. The repulsive interactions among the charged polystyrene spheres contributes most significantly to the phase transition. The above electrostatic energy can be conveniently estimated by only taking into account the nearest-neighbor interactions. The energy of the ordered phase can then be approximated by

$$H_{ordered} = (M/R)\,exp\,(-\kappa R) \tag{6.4}$$

where R is the nearest-neighbor distance in the crystal lattice, κ is the

reciprocal corrected Debye length (see equation (5.12)) and M is a constant. The energy of disordered dispersion is assumed to approximate in a similar way.

$$H_{disordered} = (M'/R') \exp(-\kappa R') \tag{6.5}$$

where R' is some mean nearest-neighbor distance and M' is a different constant (reflecting the possible different number of neighbors in the disordered dispersion).

The optical study presented in Chapter 4 has indicated that the crystal structure of ordered latexes with high particle concentration is of fcc type. R can then be determined from $(2a/R)^3=\phi/0.74$ (equation (4.13)). Since foreign electrolytes are not added into the cleaned latex system, the third term in equation (5.12) which accounts for the counterion density prevails in determining the corrected Debye length. Therefore, both of $H_{ordered}$ and $H_{disordered}$ can be expressed in terms of the particle concentration by noting that $R \alpha \phi^{-1/3}$, $R' \alpha \phi^{-1/3}$, and $1/\kappa \alpha \phi^{-1/2}$.

$$H_{ordered} = C\phi^{\frac{1}{3}} \exp(-A\phi^{\frac{1}{6}}) \tag{6.6}$$

$$H_{disordered} = C'\phi^{\frac{1}{3}} \exp(-A'\phi^{\frac{1}{6}}) \tag{6.7}$$

where C, C', A, and A' are constants. If the screening constants, A and A' , are assumed to be equal, the heat of melting then can be obtained as

$$\Delta H = \Delta C\, \phi^{\frac{1}{3}} \exp(-A\phi^{\frac{1}{6}}) \tag{6.8}$$

where $\Delta C=C'-C$ is assumed to be positive and $A=\kappa R/\phi^{1/6}$. Combining equations (6.3) and (6.8) gives the volume fraction dependence of the melting temperature.

$$Tm = \frac{\Delta C}{Nk} \frac{[\phi^{\frac{1}{3}} \exp(-A\phi^{\frac{1}{6}})]}{[\phi^{-1}\ln\phi^{-1} - (\phi^{-1}-1)\ln(\phi^{-1}-1)]} \tag{6.9}$$

For the cleaned latexes system, $a\kappa_o=0.38$ and constant stern potential 16.5 mv (i.e. $e\psi_d/kT=0.64$) obtained from previous rheological study in Chapter 5 were used to get the corrected Debye length from equation (5.12) at a certain

volume fraction ϕ. Proper selection of A and $\Delta C/Nk$ value will result in a better prediction in melting temperatures but A value used should be close to that calculated from $\kappa R/\phi^{1/6}$. Heat of melting(ΔH) and entropy change (ΔS) for phase transition of latexes with known particle concentration ϕ are then attained from equation (6.8) and (6.3), respectively.

6.3 RESULTS AND DISCUSSION

Figure 6-2 shows photographs of monodisperse latexes with ϕ=9.03% and added salt concentrations of 0, $1.0x10^{-5}$, $3.0x10^{-5}$ and $5.5x10^{-5}$ M, increasing from left to right, taken 11 days after introduction into the vials at 22 °C. The top and bottom photograph represents NaCl and $MgCl_2$ series, respectively. The reflection spectra for these samples have been presented in Figure 4-10. For cleaned latexes without adding any electrolytes, scattered crystallites appear throughout the volume of vial. As the electrolyte concentration increases, the samples start to display the coexistence of a iridescent sediments and a milky white supernatant and a sharp horizontal boundary in between, the portion of ordered lower phase decreases and finally the disordered phase occupy the total volume of vial. The volume fraction of the upper and lower phases withdrawn from each part were measured gravimetrically in a few cases. It is intriguing that the sediments are 1.2-1.4 times more concentrated than the supernatants, same results being found by Hachisu and his coworkers (32). The phase separation in a latex is difficult to understand because the latex particle size is below the critical diameter at which Brownian motion will outweigh sedimentation (166). One possible explanation is that the crystallites behave as single units and are large enough to settle under gravity. It is also interesting to note that the green color tends to appear more frequently than orange color toward the bottom of vials. This color version indicates the Bragg reflections at

the bottom are at shorter wavelengths than those at the top and the crystallites are compressed due to gravity. Comparing the top and bottom photograph tells that the iridescent portion of $MgCl_2$ series decreases at a faster pace with salt concentration than that of NaCl series. $MgCl_2$ contributes higher ionic strength and weakens the electrostatic interactions to a greater extent than NaCl does at same salt concentration. Hence, $MgCl_2$ allows Brownian motion of particles to collapse the crystal-like structure in a much easier fashion.

The sedimentation rate (v_0 of extremely dilute dispersion of rigid spheres of radius (a), in a gravitational field with acceleration constant (g) can be expressed by Stokes' equation,

$$v_o = \frac{2\,a^2\,(\rho - \rho_o)\,g}{9\,\eta_o} \tag{6.10}$$

where ρ is the density of polystyrene spheres, ρ_0 is the density of continuous medium with viscosity η_0. v_0 of an isolated latex A particle is thus obtained as 1.79×10^{-7} cm/sec at 25 °C. This means it will take 194 days for a particle to travel 3 cm of vial height. An increase in particle volume fraction will further decrease the settling rate (93) since particles no longer sediment independent of each other. Therefore no significant sedimentation of the individual particles will take place within 11 days, the time period for crystallites to fully settle under gravity.

The crystalline fraction in each vial shown in Figure 6-2 is measured. Figure 6-3 illustrates a phase diagram demonstrating the effect of salt valency and concentration on the crystal fraction for latexes A with ϕ=9.03% at 22 °C. A linear dependence in the case of NaCl was observed. Extrapolating this linear curve to 0 and 100% crystal yields a "freezing" NaCl concentration of 8.0×10^{-5} M and a "melting" concentration of 5×10^{-6} M. Same "lever rule" relationship between the crystal fraction and particle volume fraction has been reported (39)

Figure 6-2: *Photographs of monodisperse latexes with ϕ=9.03% and electrolyte concentrations of 0, $1.0x10^{-5}$, $3.0x10^{-5}$ and $5.5x10^{-5}$M (from left to right) at 22 °C; the top and bottom photograph represents NaCl and $MgCl_2$ series, respectively.*

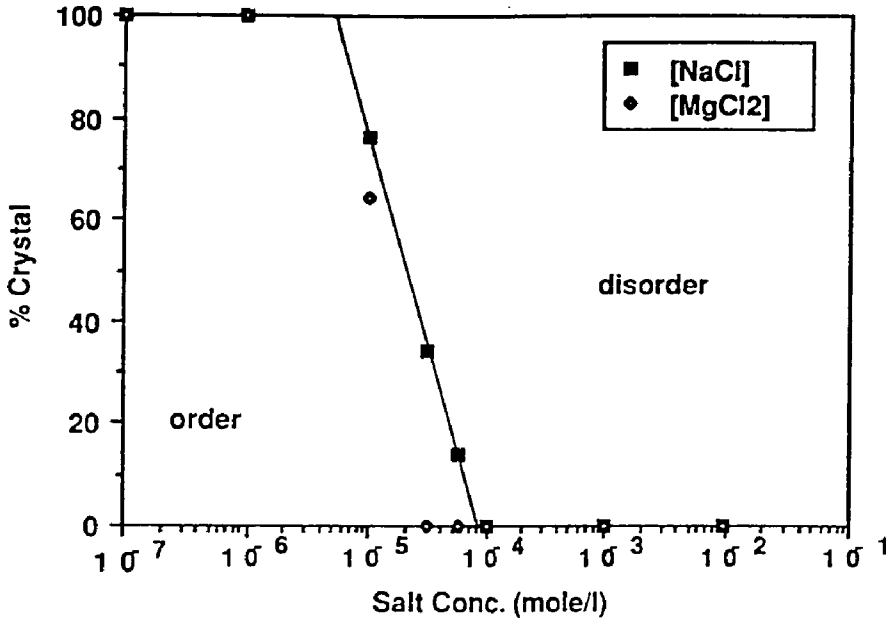

Figure 6-3: *Phase diagram demonstrating the effect of salt valency and concentration on the crystal fraction for latexes A with ϕ=9.03% at 22 °C.*

for sterically stabilized Poly(methyl methacrylate) suspensions. If crystal fraction was plotted against salt concentration in normality unit instead of original molarity unit, data for NaCl and $MgCl_2$ will fall into the same curve. This finding is reminiscent of what were found in Figure 5-6 and 5-13 of Chapter 5. This implies that the counterions play a more important role than coions in determining the colloidal properties. Also, the concentration and valency of counterions are truly effective variables to finetune the dispersion characteristics since those ions in diffuse double layer decide to what extent particle charges are shielded. The divalent electrolyte functions essentially identical as monovalent electrolyte as long as the same normality concentration is applied.

Table 6-1 exhibits the correlation of $[1-(R_e/R)]$ with β value at various particle concentrations. R_e is the effective hard sphere diameter and is

Table 6-1: *Correlation of [1-(R_e/R)] with β at various particle volume fractions ϕ; please refer to text for symbol designation.*

ϕ (%)	κa	R_e (nm)	R (nm)	[1-(R_e/R)]	G' at 2Hz (Pa)	β
8.96	1.38	402	471	0.15	0.49	0.17
18.28	2.04	347	371	0.07	2.02	0.12
26.97	2.60	322	326	0.01	17.50	0.05
30.96	2.86	314	311	-0.01	26.00	0.04

expressed as 2a[1+(1/κa)]. For cleaned latexes at 25 °C, corrected Debye length 1/κ is calculated from equation (5.12) with $a\kappa_0$=0.38, $e\psi_d/kT$=4.3 obtained from Figure 3-5 of Chapter 3. The nearest interparticle distance R can be calculated from equation $(2a/R)^3=\phi/0.74$ with a known fcc crystal structure. Factor [1-(R_e/R)] represents the degree of fluctuation freedom of hard sphere away from the equilibrium lattice site. β, a dimensionless parameter in Lindemann's law of crystal melting, carries the same physical significance but was derived from equation (5.11). Since value of storage modulus G' measured at 2 Hz was proved to be close to that of glassy modulus Gg in stress relaxation study of Figure 36, G' instead of Gg was used for calculation in equation (5.11). The results in Table 6-1 shows [1-(R_e/R)] agrees satisfactorily with β in magnitude if one takes into account the facts that longer interparticle distance has been observed in reflection spectra study and value of G' used is less than that of Gg. This finding supports the effective hard sphere model and indicates electrostatic repulsion force between particles plays a key role in crystal-like ordering. The β and rigidity values obtained for $\phi < 9\%$ lead me to classify the structured

dispersions by the following criteria:

$\beta<0.2$ or $R_e>0.8R$: solid-like

$\beta \approx 0.2$ or $R_e \approx 0.8R$: liquid-like

$\beta>>0.2$ or $R_e<<0.8R$: gas-like

Increasing the particle concentration alters the ionic environment surrounding the particle by introducing more counterions. Thus one might expect a corresponding reduction in Debye length. Indeed, this is what is shown in Table 6-1.

Above exercise justified the use of effective hard sphere model to theoretically account for the equilibrium properties of colloidal dispersions. Figure 6-4 illustrates the phase diagrum showing order-disorder transition for latex A at 25 °C, as predicted by Kirkwood-Alder transition theory and by specifying effective hard sphere diameter in terms of the uncorrected or corrected Debye length (i.e. $1/\kappa_o$ or $1/\kappa$). Each phase diagram was comprised of three zones: order, disorder and coexistence of both. The predicted phase boundaries conform qualitatively with the data of Hachisu (32) in terms of the sigmoidal trend and the width of the coexistence region. It also shows that as the electrolyte concentration increases, the excess ions screen the electrostatic interactions more effectively, thinning the electrical double layer, thus requiring higher particle concentration to induce ordering. At high electrolyte concentration, the phase transition line is essentially independent of ionic concentration. This is anticipated since the double layer thickness around a particle under this condition is negligibly small in comparison with the particle radius.

Experimental transition data attained from the visual observation of iridescence disappearance, fading reflection peak in optical study and vanishing

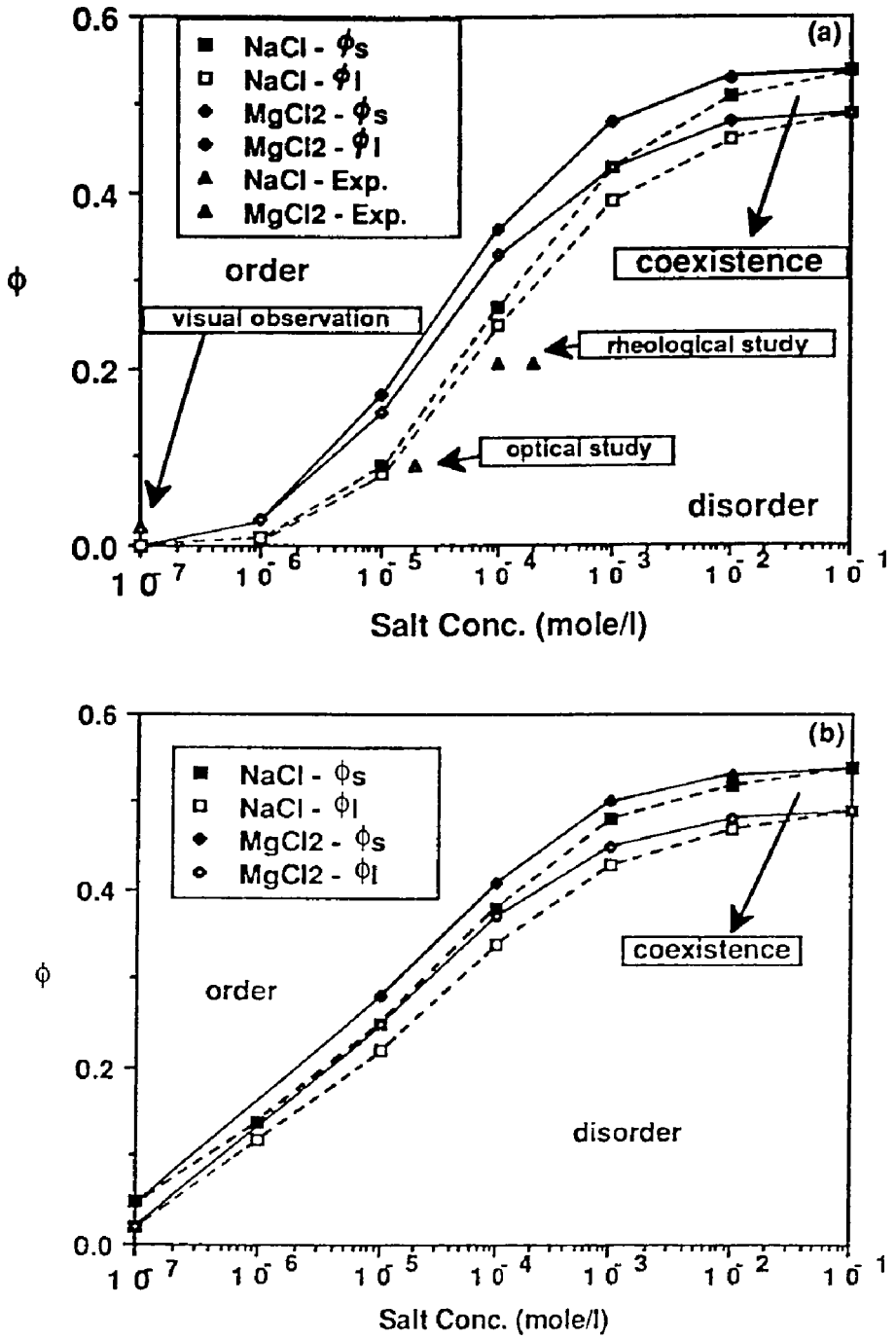

Figure 6-4: *Phase diagram showing order-disorder transition for latex A at 25 °C, as predicted by Kirkwood-Alder transition theory and by specifying effective hard sphere diameter in terms of the (a) uncorrected or (b) corrected Debye length.*

elasticity in rheological study were used to test the validity of these predictions. Although qualitative agreement between experiment and prediction was obtained, both phase diagrams underestimate the phase transition at high electrolyte concentration, predicting higher melting and freezing particle concentration. The predictions based on $1/\kappa$ (Figure 45(b)) deviate even more significantly from experimental data than that based on $1/\kappa_0$ (Figure 6-4(a)) because $1/\kappa$ is always shorter than $1/\kappa_0$ under the same conditions. If the individual latex particles are regarded as effective spheres of radius $[a+(\lambda/\kappa)]$ and the parameter λ determines the distance at which repulsive interactions between particles becomes negligible, then λ is definitely greater than one in our case. Indeed, $\lambda=1.9$ has been reported by Barnes et al.(51) in their study of phase transition in concentrated latex dispersions. The poor predictions resulted from an underestimation of effective interaction range between particles indicate that it might be better to define effective hard sphere diameter in terms of a radial distance at which the pair potential magnitude is of the order of thermal energy.

Phase diagram as a function of temperature and particle volume fraction for cleaned latex A is shown in Figure 6-5. The solid curve in the figure is a representation of equation (6.9) with A=4.0 and $\Delta C/Nk=3.9\times10^4$ °K. In view of the fact that $1/\kappa$ obtained from equation (5-12) is about one half to one third of the nearest interparticle distance (R) and A can be calculated from $\kappa R/\phi^{1/6}$, A=4.0 is a very appropriate choice. Experimental phase transition data attained from the visual examination of vanishing opalescence and attenuating reflection peak in optical study agree reasonably well with the thermodynamics' prediction. Upon increasing the particle concentration, particles interact more rigorously and numerously. Higher temerature is thus required to disrupt the ordered structure by decreasing the strength and range of repulsive interactions

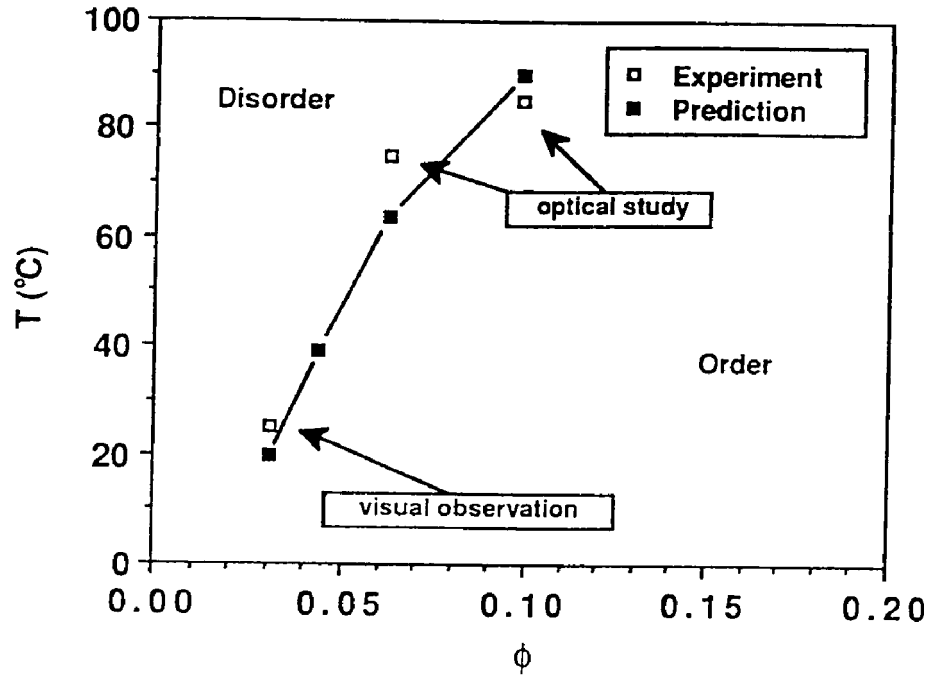

Figure 6-5: *Phase diagram as a function of temperature and particle volume fraction for cleaned latex A; the solid curve is a representation of equation (6.9) with A=4.0 and $\Delta C/Nk=3.9x10^4$ °K.*

and fueling the thermal particle motion. The heat of melting and entropy change can be calculated from equation (6.8) and (6.3), respectively, by using the quoted constant value. ΔH varies from 2.59 to 2.35 Kcal/mole and ΔS varies from 8.82 to 6.49 cal/mole °K for ϕ ranging from 3.11 to 9.82 %. These values for 0.23 μm latexes were comparable but half in magnitude to those found by Williams et al. (6) who employed 0.11 μm latexes.

The van der Waals forces between polystyrene spheres are expected to play a minimal role in the ordering phenomenon. The secondary minimum is formed as a result of significant contribution from the attraction energy to the total pairwise interaction energy, as shown in Figure 3-2 of Chapter 3. The secondary minimum becomes deeper as the electrolyte concentration is increased. Therefore, if the phase transition was caused by this minimum

energy well, the system should become more ordered when the ionic concentration is raised while maintaining a constant particle concentration. However, this contradicts to what was seen in Figure 6-4. Furthermore, by lowering the electrolyte concentration, the ordered phase was observed at very low particle concentration, such as 3% by volume fraction, which corresponds to 678 nm in center-center interparticle distance with particle diameter as 233 nm. The van der Waals force is not effective at all at such interparticle spacing. Also, the ordering has been observed for latex systems with nil van der Waals interaction by either matching refractive index (39) or matching molecular structure (33) between the polymer particle and organic solvent. Above discussions lead us to the conclusion that the van der Waals force is not essential for the ordering formation and the phase transition phenomena are therefore to be attributed mainly to electrostatic repulsion between particles.

Since sufficient experimental evidences have been presented, it seems mature now to elucidate the ordering mechanism. The order-disorder phase transition with respect to the change in particle concentration, temperature, salt valency and concentration will be explained in terms of the combined magnitude of pair potential energies which the middle particle feels, as illustrated in Figure 6-6. In an extremely diluted latex system, particles seldom interact with each other because of limited range of repulsive interaction and large interparticle spacing, therefore, they move randomly and independently due to Brownian motion. But with increasing particle concentration, the average interparticle distance becomes so small that the potential well at the center of the neighbouring particles starts to possess energy higher than thermal energy (kT). At this stage, the dual energy barrier and the effective potential well fix each particle at the lattice site, ordered structures are thus formed. Same consideration applies regarding the change in temperature, salt

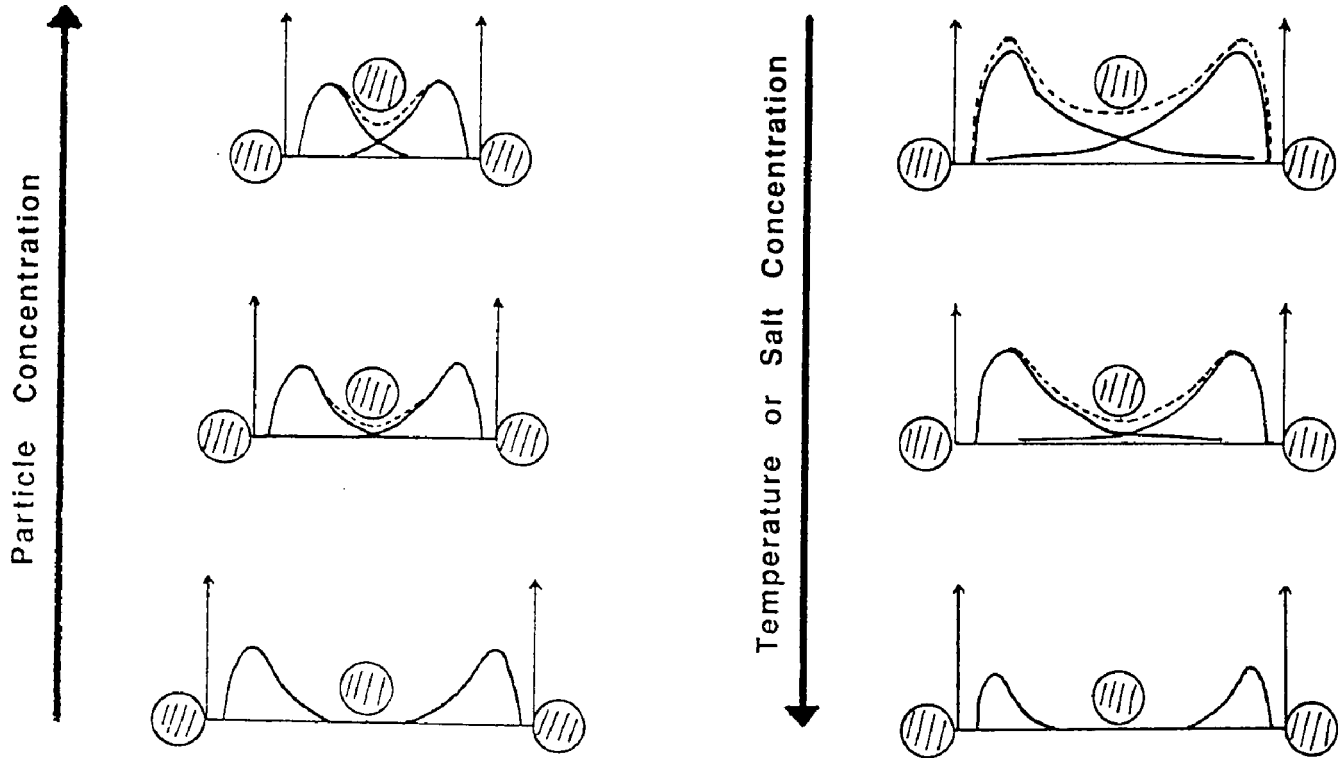

Figure 6-6: *The order-disorder phase transition with respect to the change in particle concentration, temperature, salt valency and concentration, showing schematically in terms of the combined pair potential energies.*

valency and concentration. According to the findings and discussions in Chapter 3, the potential energy barrier and range of electrostatic interaction will be reduced upon increasing temperature or electrolyte valency or electrolyte concentration. The center potential valley between two neighbour particles becomes too shallow to "freeze" the particle, the particle has more freedom to move by thermal motion and the crystal-like structure is thus collapsed. Effect of decreasing particle size at a constant particle concentration on the phase transition is expected to behave like the effect of increasing particle concentration but with a fixed particle size.

The structure of the ordered latexes has been examined by reflection spectrophotometry in Chapter 4 and identified as face-centered cubic (fcc) at high particle concentration. Melting enthalpy for the first order phase transition found in this Chapter is around 2.5 Kcal/mole which is comparable in magnitude to that of atomic crystals (167) (for example, copper has a fcc structure and heat of fusion 3.2 Kcal/mole). The ordered latexes also possess rigidity against deformation, as shown in rheological study of Chapter 5. All the above indications suggest the ordered latex is a kind of "crystal" caused by the screened electrostatic repulsion force.

Chapter 7
THE RHEOLOGICAL IMPLICATIONS ON PRINTING

7.1 INTRODUCTION

The order-disorder phase transition of monodisperse latexes has been discussed in Chapter 6. An analogy in solid-liquid phase transition exists among more practical complex systems such as printing inks. The printing process usually requires a knowledge of rheological and wetting properties of the ink so that the ink splitting and transfer mechanism can be elucidated and control for the amount of ink transfer and printing quality can be achieved. Good printability can be defined in terms of uniform ink coverage, sharp edge definition and controlled ink film thickness. In this chapter, two examples will be shown in order to demonstrate the impact made by the understanding of condition-driven phase transition. One is the correlation of ink transfer with dynamic viscoelasticity of ink under given intaglio printing conditions. The other example is the phase diagram of test printing inks. The former has been one of the long lasting goals in printing ink research. The latter provides a guideline for choosing the press parameters which in turn determine how the ink behaves rheologically during printing.

The experimental approach to achieve the above reseach objectives was designed as follows. Two series of model inks were generated by means of systematic formulation changes in varnish nature and solid content. These inks were then fully characterized in terms of the steady state viscosity and dynamic viscoelasticity. Ink transfer was quantified by the modified laboratory Prufbau Printability Tester which has the capability to simulate intaglio printing conditions. The correlation of ink transfer with ink rheology is then achieved

with the dimensionless Deborah number as an liaison. This methodology will be explained in details later in this report. A phase diagram, which establishes the phase boundary between fluid-like and solid-like region, was also constructed as a function of strain level and printing time by employing information from the characterized dynamic viscoelasticity of the test inks.

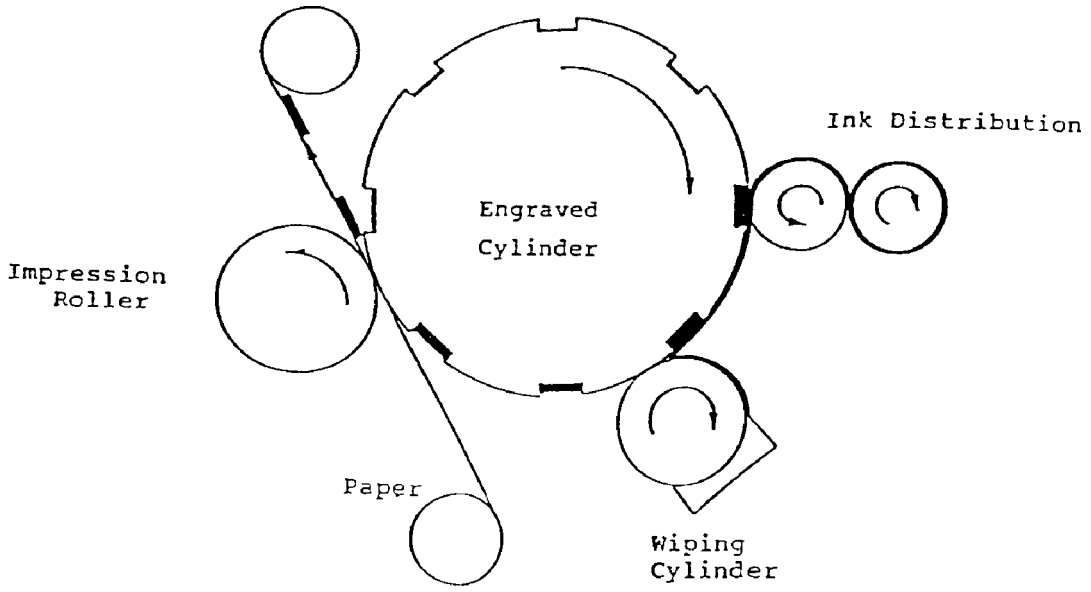

Figure 7-1: *Schematic of the intaglio printing process.*

An understanding of ink transfer requires an appreciation of the forces which the ink is subjected to and the time element involved in the printing process. Figure 7-1 illustrates the schematic of an intaglio printing process. The ink goes through distribution, wiping and printing stages. Each stage subjects the ink to high shear. The ink structures relax and recover during or between these chain of deformation events. The ink is never at rheological equilibrium during the printing process because of the high speed printing and the long relaxation time required for the ink to respond to deformation. Printing speed is thus expected to be a controlling factor for ink transfer.

7.2 EXPERIMENTAL

7.2.1 Model Inks

The formulations for the model intaglio inks are presented in Table 7-1. All the inks were well dispersed on a three roll mill. The MB1A, MB2A and MB3A series is made with different varnishes of different viscosity. The MB1E, MB1A and MB1C series is formulated by varying the calcium carbonate concentration. A production ink, BEP, was also investigated in this work.

Table 7-1: *Model intaglio ink formulations.*

	Weight %		
Component	MB-E	MB-A	MB-C
Pigment (PCN Blue)	3.8	4.0	3.6
Varnish*	39.47	33.00	29.70
Calcium Carbonate	56.16	62.40	66.16
Cobalt Drier	0.285	0.30	0.270
Lead/Manganese Drier	0.285	0.30	0.270

*MB-1 Series I-35
MB-2 Series #3 Regular Linseed
MB-3 Series #5 Pale Linseed

7.2.2 Ink Rheology

The Bohlin rheometer was used to measure the steady state viscosity and dynamic viscoelasticity of the model and BEP inks. The principles involved in the measurement and definition of rheological terms have been fully described in the Experimental section of Chapter 5.

7.2.3 Ink Transfer

The Prufbau Printability Tester was modified in order to evaluate intaglio ink transfer at printing speeds up to 6 m/sec and a cylinder/substrate pressure of 25 MPa. The impression materials used on the carrier to which the paper substrate is attached include a soft Prufbau blanket and a hard commercial BEP impression material. The Prufbau cylinder, which has a diameter of 6 cm, was engraved with lines of controlled length, width and depth. The engraving dimensions for the cylinder are shown in Table 7-2. The engravings are rectangular in cross section and represent two depths of engravings of essentially the same width and length. An ink transfer experiment with a cylinder involves : weighing the clean cylinder, filling the engravings with ink, cleaning the cylinder of excess ink, weighing the inked cylinder, producing one print, and reweighing the cylinder. The amount of ink transferred is quantified by the weight change of the cylinder.

Table 7-2: *Engraving dimensions of Prufbau cylinder.*

Length = 6 mm

	Width, um	Depth, um	Number	Vol, mm^3
Cylinder #1	660	50	73	15
Cylinder #3	600	150	74	40

7.3 THE RHEOLOGICAL CONCEPTS

The typical frequency sweeps, operated at a constant strain, for dynamic modulus and phase shift of inks are illustrated in Figure 7-2. It is shown in Figure 7-2(a) that G' dominates at high frequency whereas G" prevails at low frequency. The critical frequency f_c specifies the intersection between G' and G". Figure 7-2(b) shows that the phase shift $\tan^{-1}(G''/G')$ decreases with increasing frequency. The phase shift is 45° at the critical frequency where G'=G", and is 0° for a perfectly elastic solid and 90° for a perfectly viscous fluid. Since G' is a measure of energy stored (elastic contribution) and G" is a measure of energy dissipated per cycle of deformation (viscous contribution), the above typical results imply that the ink will behave more like a solid at high printing speed and more like a liquid at low printing speed. It is apparent that the critical frequency can be used to characterize the ink regarding the tendency of the ink to respond to printing speed as a elastic or viscous body. This concept is useful to establish the phase diagram of printing ink. The characteristic relaxation time required for ink to relax after the imposed deformation can be defined as $1/2\pi f_c$.

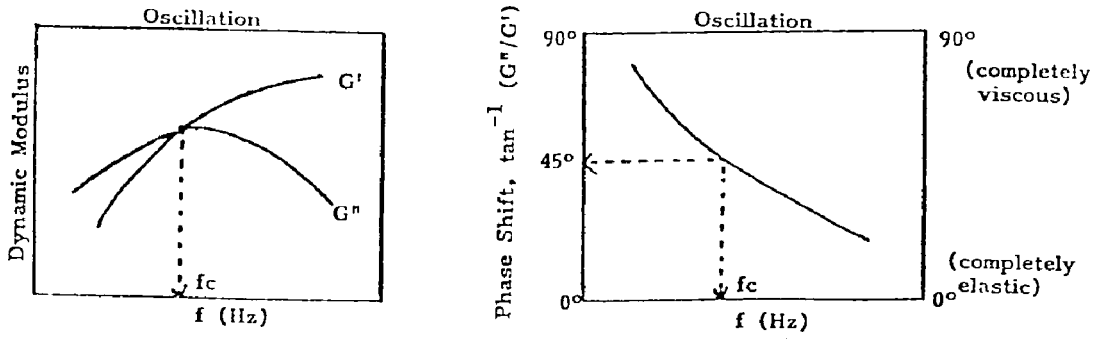

Figure 7-2: *Frequency sweeps for (a) storage and loss modulus and (b) phase shift.*

The ratio between a characteristic time for the relaxation of the material

and a characteristic time for the process is named the Deborah number and is regarded as a criterion to classify viscoelastic materials. The Deborah number for a frequency sweep, D_f, is defined as:

$$D_f = \frac{(1/2\pi f_c)}{(1/2\pi f)} = \frac{f}{f_c} \tag{7.1}$$

The Deborah number for the printing process, D_v, is expected to be a function of printing speed as it relates to the time for ink splitting from a specific engraving. The printing nip length of 2 mm was used to approximate the ink split distance. The ink splitting time, t, is thus equal to 2 mm divided by the printing speed. D_v can therefore be defined as:

$$D_v = \frac{(1/2\pi f_c)}{t} \tag{7.2}$$

The Deborah number plays a crucial role in relating the ink transfer to the dynamic viscoelasticity of ink, as will be shown in the next section.

7.4 RESULTS AND DISCUSSION

7.4.1 Correlation of Ink Transfer with Dynamic Ink Rheology

The viscosity profile for model inks MB1A, MB2A and MB3A, which contain different varnishes, is shown in Figure 7-3. All the inks exhibit shear-thinning behavior, i.e. apparent viscosity decreases with increasing shear rate. The viscosity decreases in the order of MB3A, MB2A and MB1A. The viscosity profile for model inks MB1E, MB1A, and MB1C which contain different $CaCO_3$ loading is illustrated in Figure 7-4. The viscosity increases with increasing $CaCO_3$ concentrations. All the model inks display non-Newtonian shear-thinning behavior. This is reminescent of what was seen in Figure 5-1 and 5-2 of Chapter 5.

Figure 7-5 shows the frequency sweep for the dynamic modulus of model inks MB1A, MB2A and MB3A. In all the cases the storage modulus G' increases

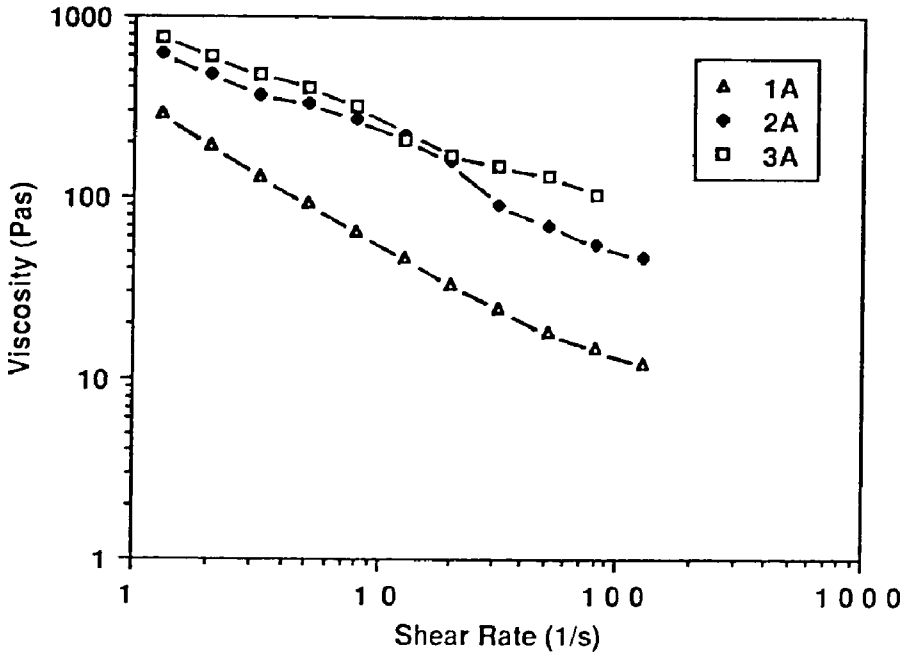

Figure 7-3: *The viscosity profile for model inks MB1A, MB2A, and MB3A.*

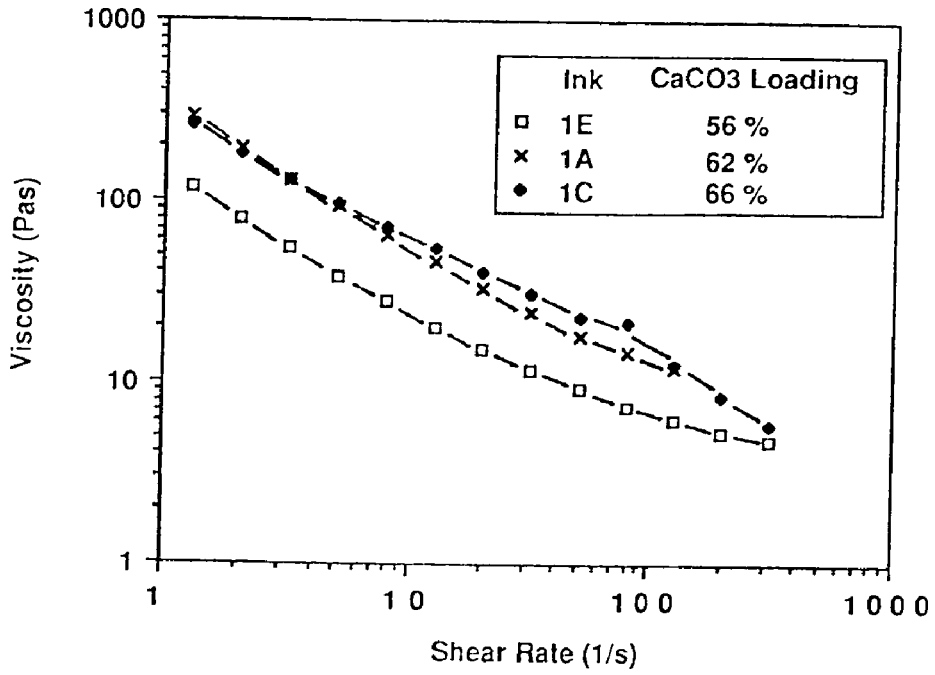

Figure 7-4: *The viscosity profile for model ink MB1E, MB1A, and MB1C.*

with increasing frequency and reaches a plateau at high frequency. Although the loss modulus G" increases initially with increasing frequency, which results in an intersection with G', it reaches a maximum followed by a decrease. MB3A possesses the highest G' and lowest G" value. This indicates that MB3A is the most elastic ink which has the longest relaxation time required to relax the deformation. Indeed, the critical frequency, which is the reciprocal of characteristic relaxation time, increases in the order of MB3A, MB2A and MB1A. Figure 7-6 illustrates the frequency sweep for the dynamic modulus of model inks MB1E, MB1A and MB1C. The results show, especially at high frequency, that G' increases while G" decreases with increasing $CaCO_3$ loading. Generally speaking, the critical frequency at which G' and G" intersects shifts to lower frequency with increasing $CaCO_3$ content as expected.

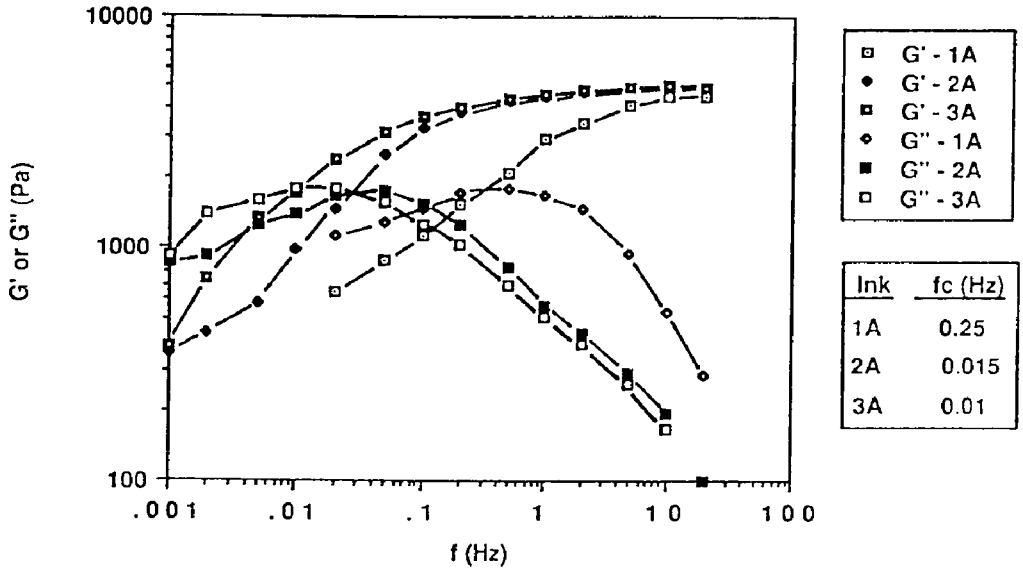

Figure 7-5: *The frequency sweep for dynamic modulus of model inks MB1A, MB2A, and MB3A.*

Frequency sweeps of the phase shift for model inks MB1A, MB2A and MB3A, Figure 7-7, show that MB3A is the most elastic ink throughout the frequency range investigated. If the phase shift is plotted against the Deborah

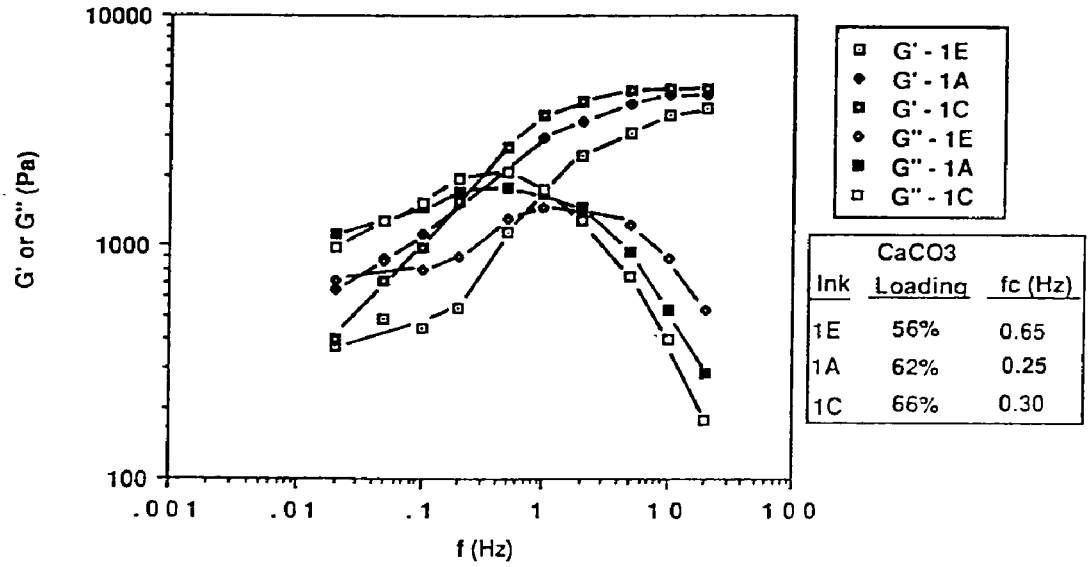

Figure 7-6: *The frequency sweep for dynamic modulus of model inks MB1E, MB1A and MB1C.*

number D_f (i.e. f/f_c) as illustrated in Figure 7-8, three curves originally separated were normalized into one sigmoidal curve. In the regions of very high and extremely low D_f, phase shift appears to be independent of frequency. As $D_f>>1$, the ink tends to behave like a solid as evidenced by a very low value of $\tan^{-1}(G''/G')$. When $D_f<<1$, the ink tends to perform like a liquid as seen by the high values for $\tan^{-1}(G''/G')$. For D_f in between above two limiting case, the phase shift exhibits the highest sensitivity to frequency or time. Figure 7-9 and 7-10 for model inks MB1E, MB1A and MB1C show essentially the same trends as discussed above. The phase shift, furthermore, is shown to decrease with increasing $CaCO_3$ concentration, especially at high frequency region. This implies that the ink with higher solid content will behave more like a solid during printing, particularly at high printing speed.

Intaglio ink transfer data at various printing speeds on the Prufbau using Portals paper with two engraved cylinders are presented in Table 7-3. Ink transfer increases with decreasing printing speed or increasing engraving

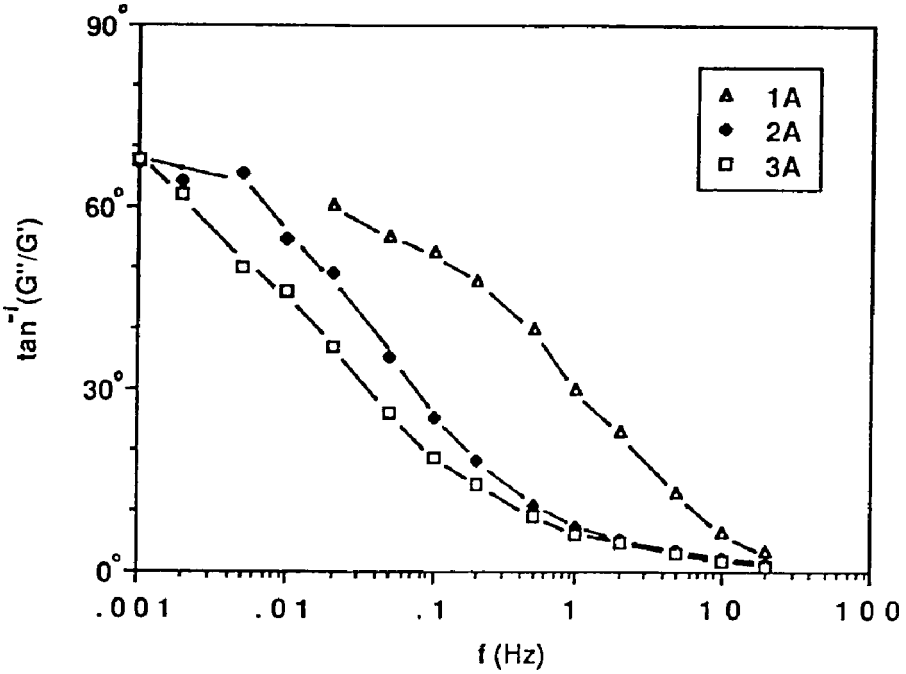

Figure 7-7: *The frequency sweep for phase shift of model inks MB1A, MB2A, and MB3A.*

depth. It appears that there is a relationship between the amount of ink removed from the engravings during wiping and the amount of ink transferred during printing. The printing Deborah number D_v has been defined as the ratio of the ink relaxation time, which is related to critical frequency f_c, to the printing time. The elastic response is expected to predominate for high D_v values while the viscous response prevails for low D_v values. The ink transfer data at various speeds were reprocessed to give a plot of the absolute ink transfer as a function of log D_v as shown in Figure 7-11. The results show that the ink transfer decreases linearly with increasing log D_v. Ink transfer with deeper engraved cylinder displays higher sensitivity to D_v.

D_f is the oscillation measurement Deborah number while D_v represents the printing Deborah number. It is reasonable to assume that D_v is qualitatively equivalent to D_f, and to combine the results in Figure 7-8 and 7-10

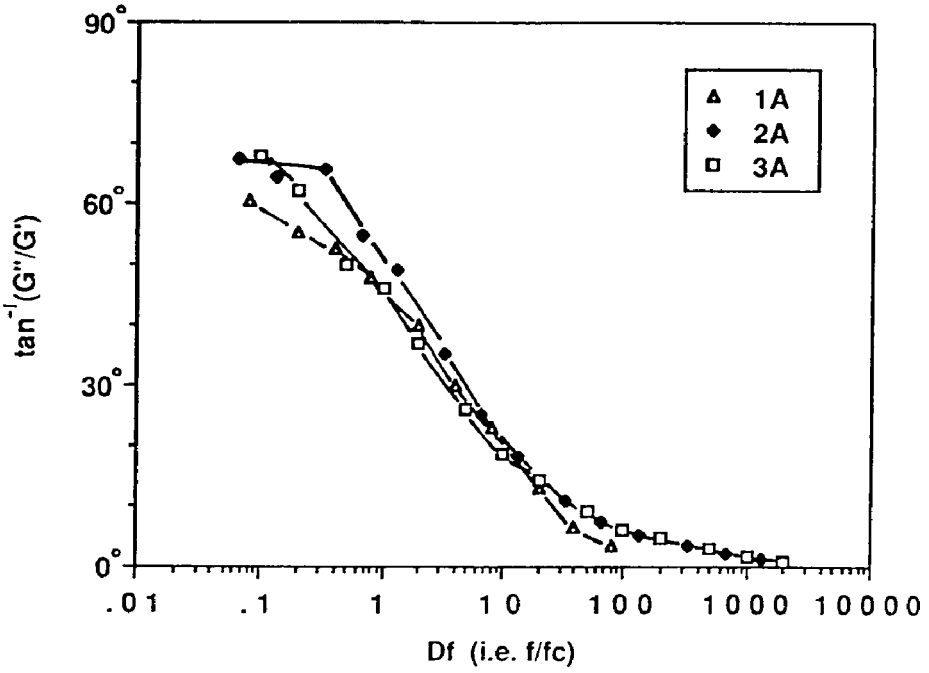

Figure 7-8: *Phase shift as a function of Deborah number, D_f for model inks MB1A, MB2A, MB3A.*

with the results in Figure 7-11. The above approach produces a plot of ink transfer vs. phase shift as illustrated in Figure 7-12. It is shown that the ink transfer decreases linearly with decreasing phase shift, i.e. increasing elastic response brought about by increasing printing speed. Ink transfer with deeper engraved cylinder exhibits higher sensitivity to the dynamic viscoelasticity of inks. It is interesting to note that for a given engraved cylinder the slopes obtained from the ink transfer curves in Figure 7-12 have similar values. The average for these slope values were plotted against the ink depth in the engraing in Figure 7-13. A linear relationship was observed which passes through the origin. An ink transfer equation can thus be proposed from these data as follows.

$$T = 0.0036\, D\, (\delta - \delta_o) \tag{7.3}$$

where T is the amount of ink transferred, δ is the phase shift, δ_o is the phase

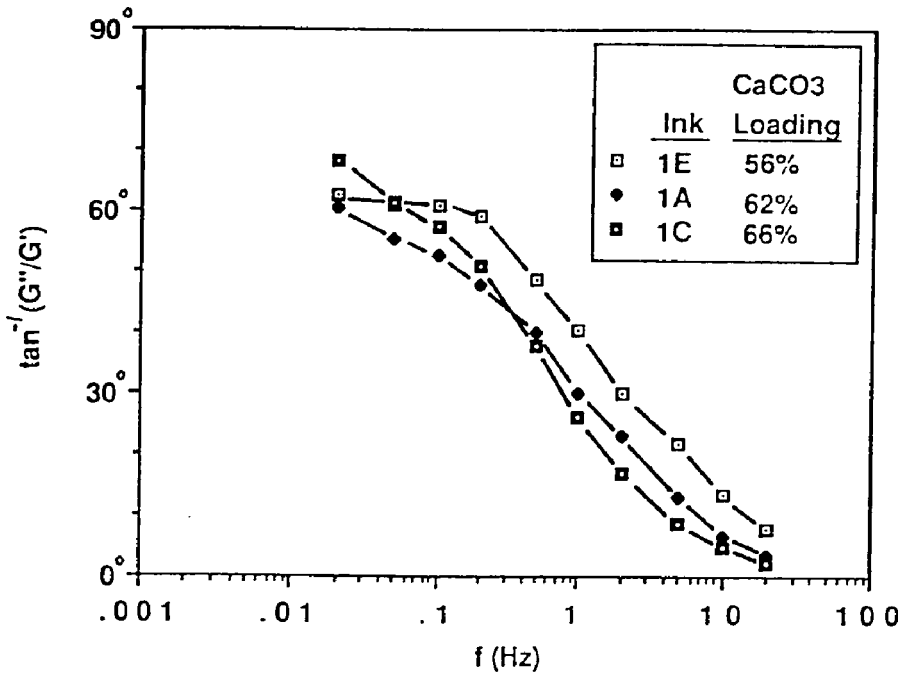

Figure 7-9: *The frequency sweep for phase shift of model inks MB1E, MB1A and MB1C.*

shift where T=0, and D is the ink depth in the engraving (μm).

Figure 7-14 shows the ink transfer vs. phase shift for the model inks MB1A and MB3A printed with two impression materials of different hardness. Similar linear relationship as seen in Figure 7-12 was observed for the harder BEP impression material. The results indicate that under the same printing conditions ink transfer with softer Prufbau backing is higher because the impression material with lower modulus is deformed sufficiently to provide better ink-to-paper contact. It is believed that dynamic mechanical spectrum of impression materials will offer additional information concerning critical frequency and printing speed as a function of backing deformation. It appears that δ_o, which is the intercept at zero ink transfer, is influenced by the hardness of impression material, the viscosity level and the ink depth in the engraving.

The definition of ink split time used in the previous calculation of D_v has

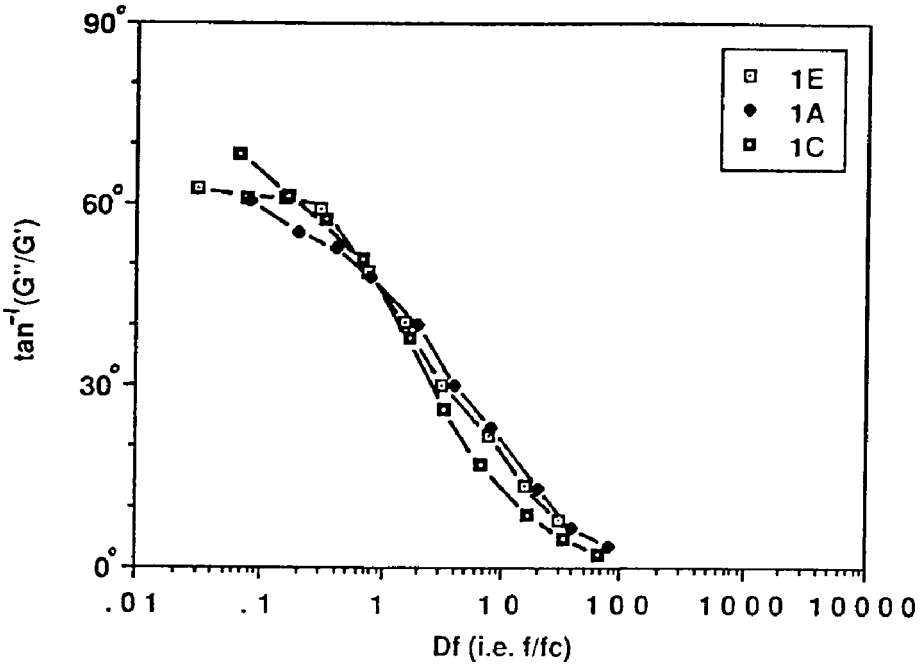

Figure 7-10: *phase shift as a function of Deborah number, D_f for model inks MB1E, MB1A and MB1C.*

been argued (168) to be theoretically unsound because the split time can be expected to be affected not only by the printing speed (V) and half of nip length (b) but also by the maximum ink strain (ε_o), ink depth in the engraving (d) and the radius of engraved cylinder (R). The results of this line of reasoning (168) suggest the following equation for defining the ink split time.

$$t = \frac{\varepsilon_o R\, d}{b\, V} \tag{7.4}$$

The speed-dependent-ink transfer data can now be reprocessed based on the new split time equation (7.4), although the qualitative significance shown thus far is not expected to be changed by the recalculation.

Table 7-3: *Intaglio ink transfer data at various printing speeds on Prufbau using Portals paper with two engraved cylinders and Prufbau impression material.*

CYLINDER # 1 — Width [um] 660 — Depth [um] 50 — Vol. [mm³] 15

	Speed	Ink on Cylinder		Ink on Print		Transfer
	m/s	mg	mm3	mg	µ	%
1-E	4.0	10.5	7.0	1.5	3.3	14.7
	2.0	10.6	7.2	2.7	5.9	25.3
	1.5	11.2	7.6	3.1	6.8	27.4
	1.0	11.6	7.8	3.5	7.5	29.8
	0.40	12.2	8.2	4.4	9.6	36.0
1-A	4.0	12.6	7.8	1.7	3.5	13.9
	2.0	13.2	8.2	2.5	5.1	18.8
	1.5	13.1	8.2	2.5	5.1	19.1
	1.0	13.5	8.4	3.4	6.9	25.3
	0.40	11.9	7.5	3.8	7.8	32.4
1-C	2.0	12.3	7.6	2.0	4.1	16.2
	1.5	14.7	9.1	2.6	5.3	17.7
	1.0	13.9	8.6	2.8	5.8	20.4
	0.40	15.1	9.4	3.9	7.9	25.8
2-A	2.0	15.4	9.6	1.8	3.7	11.9
	1.5	15.7	9.8	2.0	4.0	12.6
	1.0	14.9	9.4	2.2	4.5	14.8
	0.40	15.5	9.7	3.2	6.5	22.8
3-A	2.0	13.8	9.2	1.8	3.8	12.6
	1.5	14.9	9.9	2.0	4.2	13.2
	1.0	15.1	10.1	2.2	4.8	14.5
	0.40	14.9	9.9	3.4	7.4	22.8
BEP	2.0	22.5	10.2	1.7	2.5	7.5
	1.5	22.2	10.1	1.9	2.8	8.5
	1.0	22.3	9.9	2.7	4.0	12.1
	0.40	22.7	10.3	4.0	5.9	17.6

CYLINDER # 3 — Width [um] 600 — Depth [um] 150 — Vol. [mm³] 40

Speed	Ink on Cylinder		Ink on Print		Transfer
m/s	mg	mm3	mg	µ	%
2.0	37.3	25.0	4.9	12.4	13.1
1.5	37.7	25.3	4.7	11.9	13.8
1.0	38.6	25.8	8.0	20.1	20.8
0.4	40.2	26.9	11.1	28.1	27.7

Speed	Ink on Cylinder		Ink on Print		Transfer
m/s	mg	mm3	mg	µ	%
2.0	43.1	27.0	3.9	9.2	9.0
1.5	45.6	28.5	3.6	8.5	8.0
1.0	44.2	27.6	5.9	13.9	13.3
0.4	41.0	25.6	8.8	20.6	21.4

Speed	Ink on Cylinder		Ink on Print		Transfer
m/s	mg	mm3	mg	µ	%
2.0	42.0	26.0	2.5	5.7	5.8
1.5	43.9	27.3	3.8	8.9	8.7
1.0	42.2	26.2	4.6	10.8	10.8
0.4	45.4	28.2	9.1	21.3	20.1

Speed	Ink on Cylinder		Ink on Print		Transfer
m/s	mg	mm3	mg	µ	%
2.0	46.5	29.0	2.0	4.6	4.2
1.5	47.6	29.8	2.5	5.9	5.3
1.0	44.8	28.0	3.8	8.8	8.3
0.4	46.2	28.8	6.5	15.3	14.2

Speed	Ink on Cylinder		Ink on Print		Transfer
m/s	mg	mm3	mg	µ	%
2.0	46.5	31.0	1.1	2.8	2.4
1.5	46.0	30.7	2.7	6.5	5.5
1.0	45.3	30.2	3.4	8.5	7.5
0.4	44.9	29.9	9.4	23.6	20.9

Speed	Ink on Cylinder		Ink on Print		Transfer
m/s	mg	mm3	mg	µ	%
2.0	60.8	27.6	1.7	2.9	2.8
1.5	63.2	28.7	1.9	3.2	3.0
1.0	62.0	28.2	2.9	4.9	4.7
0.4	62.5	28.4	9.8	16.8	15.8

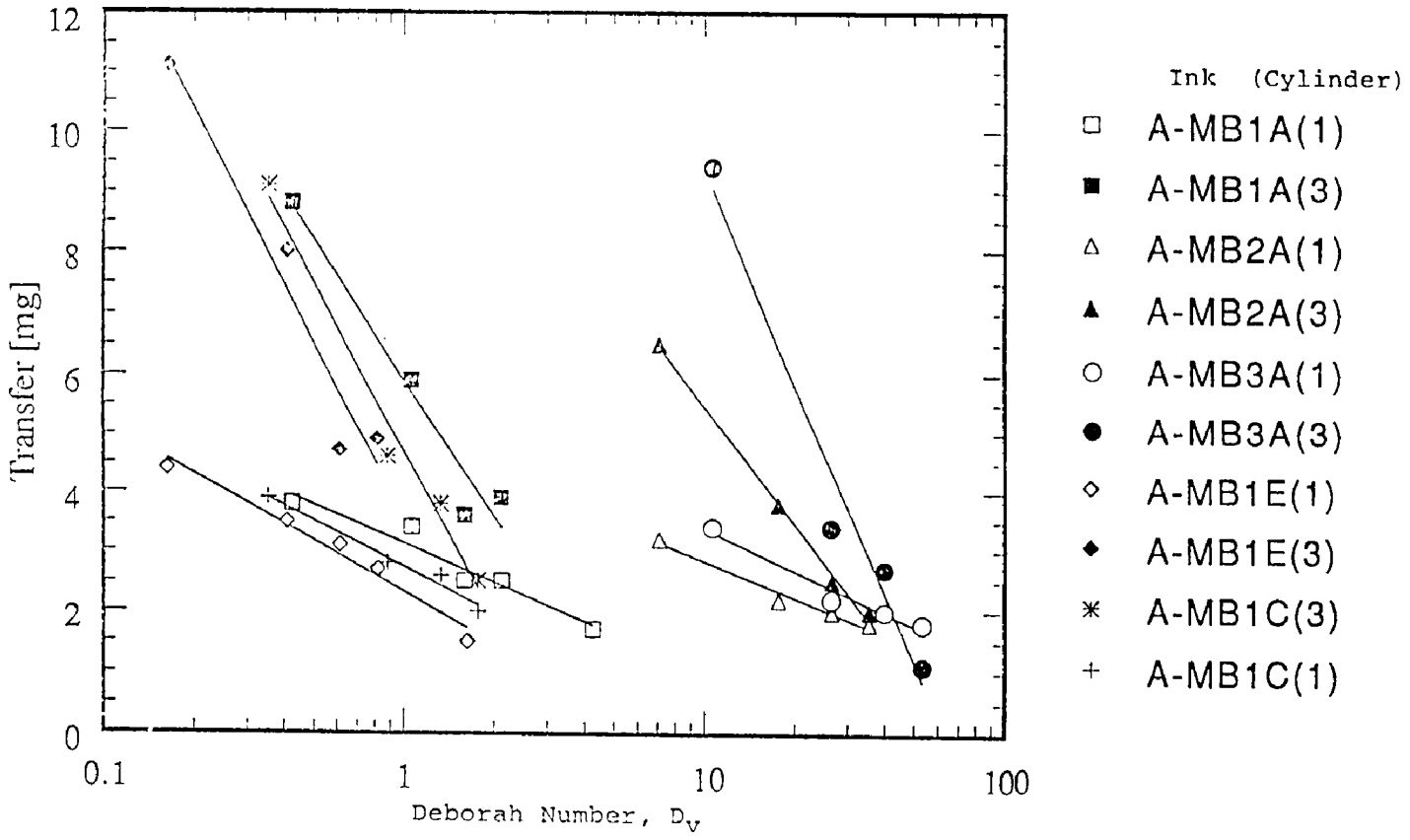

Figure 7-11: *Ink transfer as a function of Deborah number D_v for model inks.*

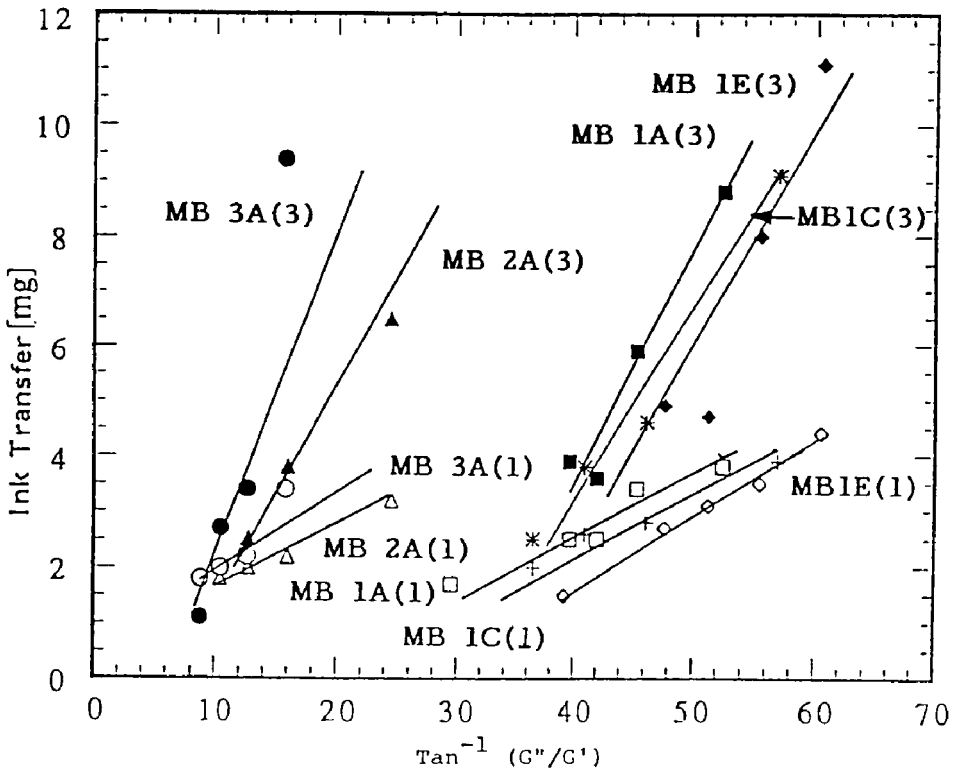

Figure 7-12: *Ink transfer as a function of phase shift for the model inks printed with cylinders (1) and (3) and Prufbau impression material.*

7.4.2 Phase Diagram of Printing Inks

Printing performance depends on the physical properties of ink and the dynamics of ink splitting from the engraving to the paper substrate. Theory predicts that ink behaves like a solid at very high strain rate and as a liquid under conditions of low strain rate. At constant strain, a solid-liquid transition (i.e. G'=G") takes place at a critical frequency f_c as shown in Figure 7-2(a). If the intersection between G' and G" were obtained for various strain-time conditions, it would be possible to establish a criteria for ink behavior under splitting conditions. This concept resulted in a series of frequency sweep measurements for dynamic modulus measured as a function of strain on MB1A and BEP inks

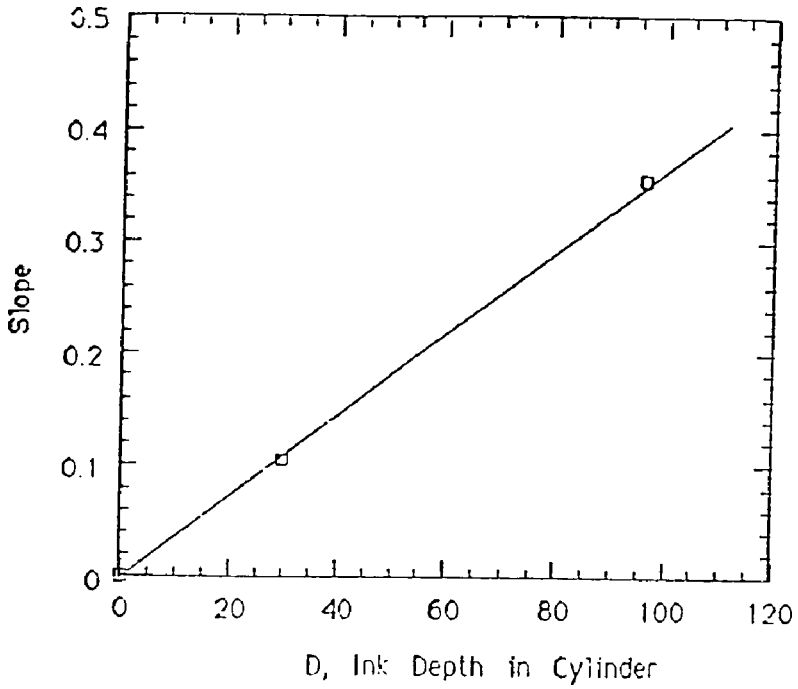

Figure 7-13: *Slope of ink transfer/phase shift curve vs. ink depth in the engraving (μm).*

at 25°C and 80°C. The strain level and the corresponding ink relaxation time, which was calculated from $1/2\pi f_c$, were used to construct a phase diagram which predicts the phase boundary separating fluid and elastic regions, as illustrated in Figure 7-15. The solid lines indicate that the ink relaxation time decreases with increasing strain amplitude. As the oscillation strain is increased, more kinetic energy is imposed on the microstructure units of ink, which results in a perturbation of the ink structure and the ink tends to relax the deformation faster and behave more like a liquid. One implication of this phase diagram is that the ink tends to behave more like a liquid as printing speed is decreased (i.e. longer split time) at constant strain. Another implication is that the inks become more fluid-like upon increasing the printing temperature. The typical frequency sweep for dynamic modulus at different imposed strains is shown in Figure 7-16. At low strains, G' increases while G" rises initially and decreases

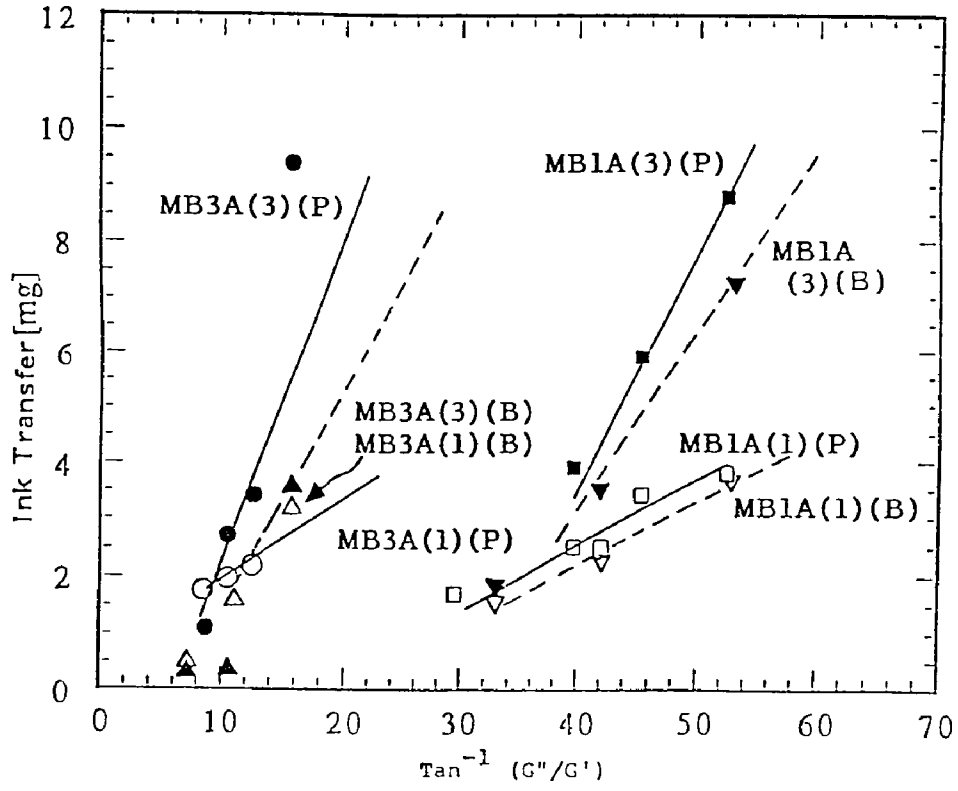

Figure 7-14: *Ink transfer vs. phase shift for the model inks MB1A and MB3A printed with engraved cylinders (1) and (3) and Prufbau (P) and BEP (B) impression materials.*

with increasing frequency after intersecting with G'. At low strains G' dominates over G" at high frequency. However, at high strains, G' and G" both increase with increasing frequency, and eventually become parallel at high frequency without intersecting. G" thus prevails over G' throughout the entire frequency range. The lack of an intersection of G' and G", which disallows the evaluation of a critical frequency, has been illustrated as dashed line in the phase diagram of Figure 7-15. This finding implies that the inks will behave like a liquid after exceeding a certain strain level in spite of the printing speed. The phase shift for MB-1A and BEP as a function of temperature, Figure 7-17, show that the viscoelastic properties of BEP ink at low strain are insensitive to

temperature whereas MB1A becomes dramatically more liquid-like with increasing temperature. These results are consistent with Figure 7-15 which shows that this relationship is true at low strain, but is not true at high strain where the viscoelastic properties of BEP are very sensitive to temperature and become more liquid-like with increasing temperature.

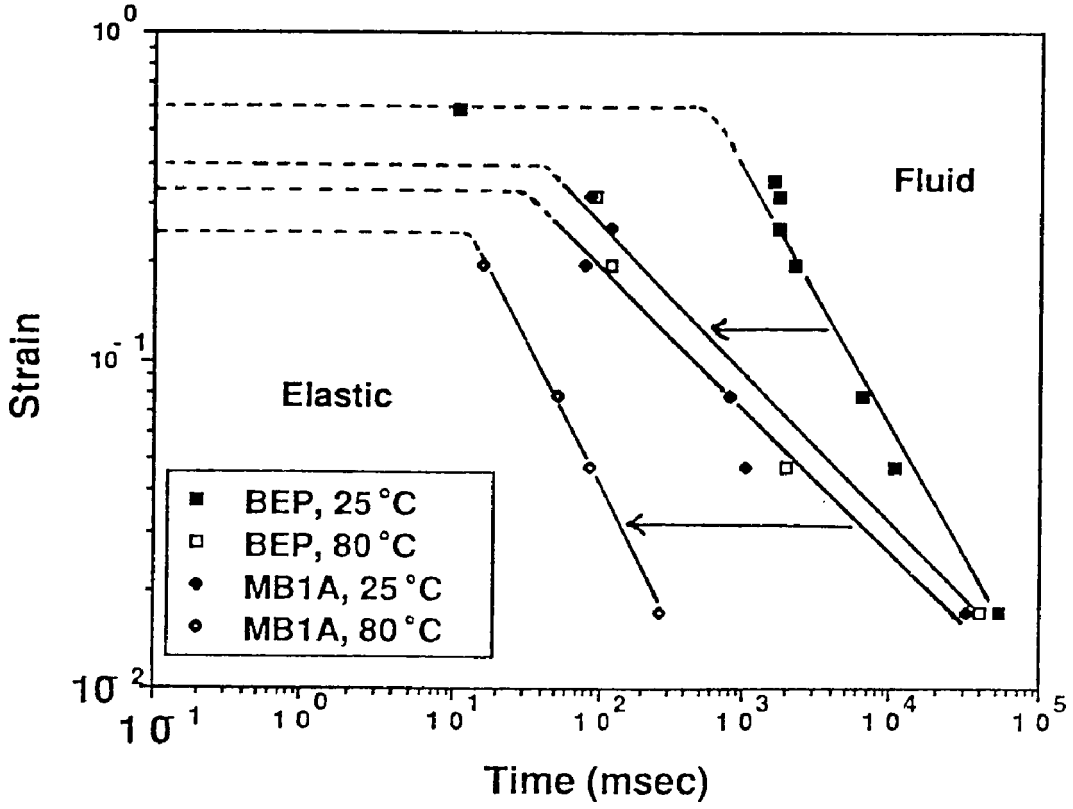

Figure 7-15: *Phase diagram as a function of strain and time for MB1A and BEP inks at 25 °C and 80 °C.*

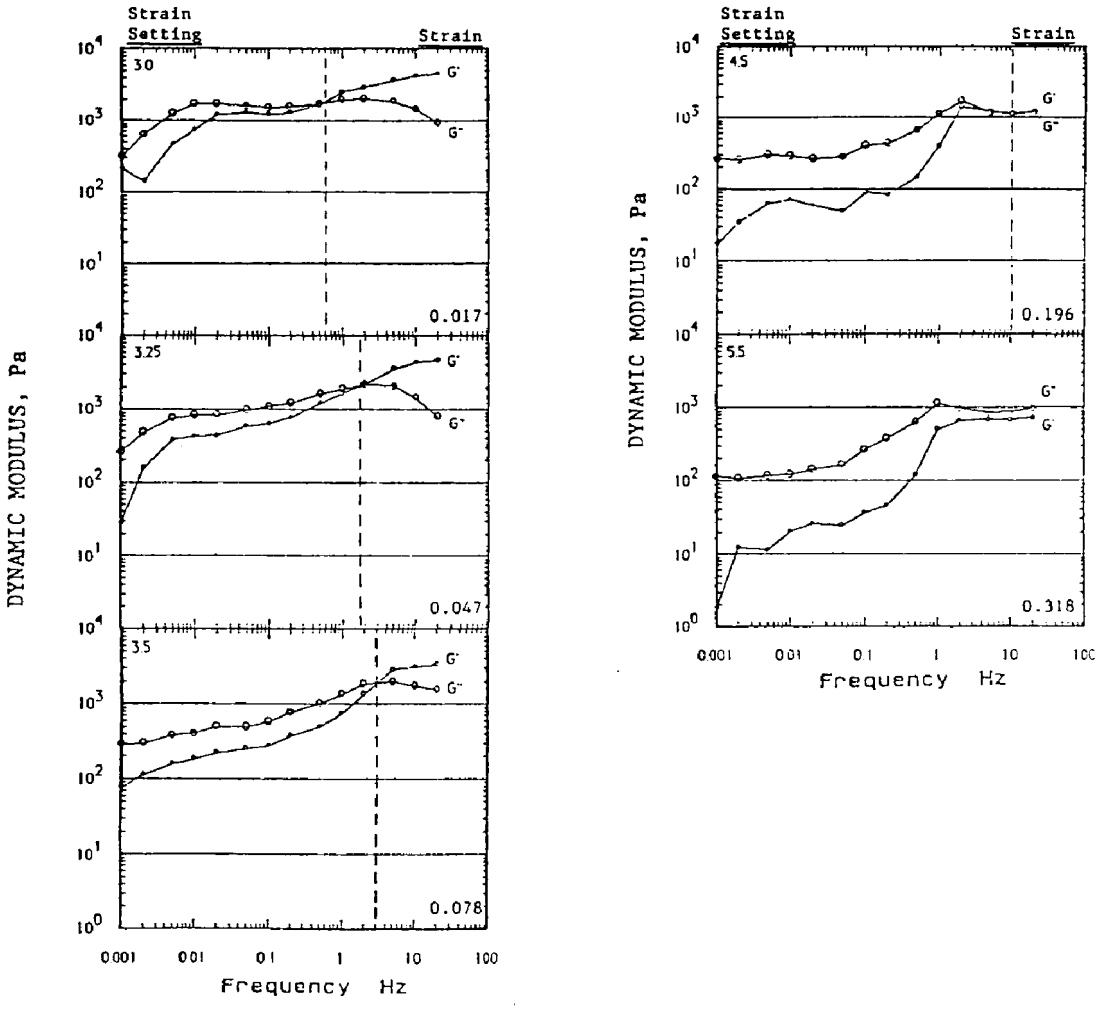

Figure 7-16: *Frequency sweep measurements for dynamic modulus at different imposed strains for MB1A at 80 °C.*

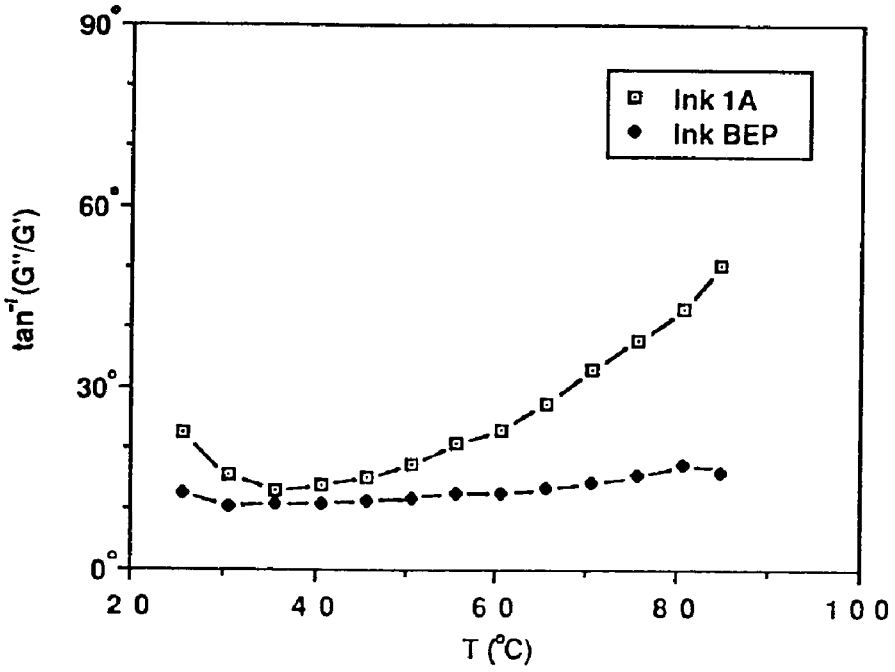

Figure 7-17: *Phase shift as a function of temperature for MB1A and BEP inks, measured at strain equal to 0.03.*

Chapter 8
CONCLUSIONS

The purpose of this research work was to (i) elucidate the interplay among colloidal forces, dispersion microstructure and resulting rheological properties of ordered polymer colloids, (ii) study the order-disorder phase transition behavior of monodisperse latex and (iii) demonstrate how the concept of solid-liquid phase transition places an impact on the understanding of printing performances. These research objectives were fulfilled together with several conclusions drawn out of the work presented in this dissertation.

(1) Dow latex A was fully characterized by transmission electron microscopy, conductometric titration and Fourier Transform Infrared spectroscopy. The results indicate that these latex particles have a mean diameter of 233 nm with a standard deviation 14 nm, carry both strong (sulfate) and weak (carboxyl) acidic group and possibly hydroxyl group on the particle surface, and possess a chemical composition of polystyrene. The spherical geometry, rigidity and uniformity of particles and the well characterized particle surface justify the use of polystyrene latex A as a model colloid.

(2) The electrophoretic mobilities of model latex A were obtained under various conditions of temperature, pH, salt valency and salt concentration. The results support the concept of a dual particle charging mechanism. One mechanism is controlled by the ionization of surface groups. The other mechanism is controlled by the nature of the bare polymer surface which preferentially adsorbs coions. The former mechanism dominates when particles carry high concentration of surface acid groups.

(3) The zeta potentials of latex particles were converted from the measured electrophoretic mobilities by taking into account the retardation effect

due to backward flow of the solvent and the relaxation effect due to distortion of the ionic atmosphere surrounding the particle. It is shown that the zeta potential and electrical double layer thickness of latex A is decreased with increasing either salt valency, salt concentration or temperature. The strength and range of electrostatic repulsion between particles is therefore reduced with decreased zeta potential and Debye length based on the DLVO theory.

(4) The appearance of reflection spectra of cleaned latex A at various particle concentrations clearly offers evidence that ordered structure is formed in the dispersion. It is shown that the reflection peaks become progressively broader and are shifted in the direction of smaller interparticle spacings with increasing particle concentration. The reflection peak was found at a particle volume fraction as low as 4.37% where the particles are 2.5 diameters apart. This implies that long-range electrostatic repulsion between particles is related to the existence of order in dilute dispersion.

(5) Based on the Bragg's law, the experimental nearest interparticle distance (D_e) could be obtained from the wavelength at the reflection peaks. The theoretical one (D_t) could be calculated by assuming a crystal lattice and uniform particle distribution throughout the dispersion. D_e was found to agree satisfactorily with D_t. Closer match between D_e and D_t of face-centered cubic agrees with the literature finding that fcc structure is much more stable than bcc at high particle concentration.

(6) The reflection intensity decreased with increasing temperature. The reflection peak displaced unexpectedly toward smaller wavelength with increasing temperature. One possible explanation for this trend, which is supported by the thermodynamics, is the lattice structure transition, i.e. from fcc to bcc with rising temperature, because bcc possesses narrower interparticle distance than fcc at constant particle concentration.

(7) More rigorous Brownian motion at higher temperature and reduced strength and range of electrostatic repulsion between particles give rise to more freedom to particle motions. Latex spheres can no longer be locked into crystal lattice sites and ordered structure is thus collapsed. This "melting" temperature which is monitored by the diminishing reflection peak is found to increase with increasing particle concentration. The electrostatic interactions become stronger and more numerous as particle concentration is increased. These fortified interactions are more capable of resisting the tendency of thermal motions to disrupt the ordered dispersion structure. Hence, the reflection peak can persist at higher temperature.

(8) The reflection intensity becomes lower and the reflection peak becomes broader upon increasing the salt concentration. The vanishing peak is an indication of order-disorder phase transition since the suppressed electrostatic repulsion no longer can freeze the particles within the crystal lattice and the Brownian motion destroys the ordered structure upon adding excess electrolyte. As the dispersions become more disordered, the limited irradiation penetration and beam attenuation due to particle scattering reduce the reflection intensity and broaden the reflection peaks.

(9) The salt $MgCl_2$ contributes higher ionic strength and suppresses the Debye length more markedly. Therefore, the monovalent NaCl can maintain dispersion order at a higher salt concentration than the divalent $MgCl_2$. The reflection spectrophotometry was proved to be a convenient and effective experimental technique to explore the crystal-like structure of dispersion.

(10) The number of crystalline layers (N) in a dispersion which can be penetrated by irradiation was estimated from the consideration that the peak width is entirely taken into account by the irradiation penetration depth and not by the degree of crystallinity. The results indicate that N decreases from 19

to 5 as particle concentration increases from 4.37 to 23.22%. This is in agreement with the expectation that less turbidity and particle scattering with lower particle concentration lead to deeper irradiation penetration into dispersion.

(11) The rheological characteristics of dispersion depend strongly on the interparticle forces. A particle in a suspension is subjected to various forces, e.g. hydrodynamic, thermal, van der Waals, electrostatic and steric repulsion, etc. Dimensional analysis of the relevant forces allows a classification of dispersions according to their stability and the effect of externally imposed flow.

(12) The rising viscosity with higher particle concentration or lower temperature can be explained qualitatively by the secondary electroviscous effect, i.e. the increase in energy dissipation resulting from alterations of particle trajectories due to the presence of electrical charges, which cause the particles to avoid one another.

(13) While Hoffman's four regime flow mechanism (154, 155) is capable to account for the flow properties of cleaned latex dispersions, the possibility of forming ordered layers at high shear is reduced at higher temperature or lower particle concentration because of the reduced range of electrostatic repulsion between particles. Consequently, the degree of shear-thinning became less obvious at elevated temperature or lower particle concentration and structure difference between low and high shear rate eventually disappear.

(14) Dilatancy behavior was observed for cleaned latexes with particle concentration below 10%. This is attributed to the onset of turbulent flow at high shear rate for samples with low kinematic viscosity. Shear induced order-disorder transition was not operational in this case because at low particle concentration the unhindered particle rotations dissipate the viscous couple that is required to destroy the stability of ordered layer flow. In the viscosity

measurements, the maximum shear rate before the onset of turbulence depends on the measuring couette geometry and the kinematic viscosity of samples. The ordered dispersion microstructures were found to suppress the flow instability, which means that the turbulent flow will occur at a shear rate higher than the one theoretically expected.

(15) The Arrhenius equation (η=A exp(B/T)) was found to be applicable to the system of colloidal dispersions. Constant A is a particle packing factor indicating the availability of unoccupied free volume. B is an enthalpy term relating with the total potential energy of interaction between particles. The viscosity of dispersion medium (water) is more sensitive to the temperature than that of colloidal dispersion, probably because of different relaxation time corresponding to different dimensions of structure units in these materials.

(16) A minimum is observed in the plot of viscosity versus salt concentration. The viscosity first decreases with increasing salt concentration due to compression of Debye length and reduction of Coulombic repulsion strength. Upon further addition of electrolyte, the electrostatic repulsion forces are effectively screened out and van der Waals attraction comes into play. Brownian or shear-induced coagulation of latex particles thus occurs to give higher viscosity. Higher salt valency and shear rate greatly destabilize the dispersion. Hence, viscosity increases monotonically with electrolyte concentration without observing the minimum.

(17) The viscosity data for $MgCl_2$ at low shear rate can be superimposed on that for NaCl if the salt concentration is expressed in units of normality but not molarity. This observation is in agreement with the Krieger and Eguiluz's (62) finding that the secondary electroviscous effect is a function of equivalent concentration of added electrolyte, and is a weak function of the changing type or valence of ions.

(18) In steady shear the particles are forced to flow past one another with the result that the interaction energy is dissipated. The small amplitude oscillation, however, induces weaker hydrodynamic interactions and maintain the ordered structure. Electrostatic energy is thus stored and generates the observed elasticity in storage modulus G'. Hence, the elasticity of dispersions originated from the enthalpy change rather than entropy change as observed in macromolecular fluids.

(19) Storage modulus G' decreases and phase shift $\tan^{-1}(G''/G')$ increases with decreasing particle concentration, or increasing either temperature or salt concentration. This is ascribed to the corresponding reduction in the strength and range of interparticle Coulombic repulsion force. Thermal motions of particles thus overcome the suppressed electrostatic repulsion and disintegrate the crystal-like structure of dispersion. The more electrostatic energy is thus dissipated and this results in an increase in the loss modulus G". Once the range of electrostatic interaction falls below the interparticle separation, the elasticity disappears and dispersion becomes disordered. The vanishing elasticity was thus taken as an indication of order-disorder phase transition.

(20) $MgCl_2$ data are superimposed on the NaCl data at the same normality either in the case of G' and G" or $\tan^{-1}(G''/G')$. The same agreement was observed from the viscosity data. This demonstrates that counterions play a bigger role than the coions in determining the colloidal behavior. One mole/l of Mg^{2+} concentration works like two mole/l of Na^{+} concentration to screen off part of the particle charge.

(21) The flow oscillation technique used to follow the structure recovery has potential to be an important tool for studying the kinetics of crystallization of the structured latex dispersion.

(22) G', G" vs. ε (strain) behavior of structured latex dispersions resembles

G', G" vs. T (temperature) behavior of polymeric materials. The glass transition temperature (T_g) interpreted as the onset of long-range, coordinated molecular motion represents the transition point between glassy state and rubbery state of polymeric materials. The intersection strain (ε_c) between G' and G" of an ordered dispersion thus indicates the presence of a solid-liquid transition point as a result of long range particle diffusion. This interpretation is based on the observation that G' dominates over G" as $\varepsilon<\varepsilon_c$ and G" dominates as $\varepsilon>\varepsilon_c$.

(23) Measurement of stress relaxation has been found to be correlated with that of dynamic oscillation for ordered dispersions. If one viscoelastic function is known over a wide range of time or frequency, then in principle any other viscoelastic function can be derived using exact transformation equations given by the mathematical theory of linear viscoelasticity. Since an empirical equation has been proposed to represent the stress relaxation modulus (G(t)), other viscoelastic properties such as storage modulus (G') and loss modulus (G") can thus be obtained numerically through the exact interrelations among viscoelastic functions.

(24) Neither Maxwell Element nor Four-Element model (combination of Maxwell and Voigt Element in series) was found to successfully describe the viscoelastic behavior of the ordered dispersions, such as G(t), G' and G". This is not surprising since limited number of relaxation time attained from these models contradicts with what is observed in relaxation spectrum. Hence, it is expected that generalized Maxwell model (Maxwell Elements in parallel) will better account for the broad relaxation spectrum. A shorter characteristic (peak) relaxation time is obtained with a lower particle concentration or higher temperature. This result is anticipated since the structured dispersions become less elastic due to the decreased strength and range of electrostatic repulsion force between particles.

(25) The elastic modulus can be expressed in terms of the number density of particles and a dimensionless parameter β which represents the degree of particle fluctuation away from the crystal lattice point and is a measure of strength of electrostatic interactions between particles. Lindemann's law of crystal melting predicts that $\beta<0.1$ for a stable crystal. The results for $\beta<0.1$ for $\phi>15\%$ has been obtained in this work. Overlooking the finite number of particles per unit cell results in higher β values than were reported in Mitaku (66) and Okubo's (88) results.

(26) The theoretical shear modulus of ordered latexes has been derived from the increase in electrostatic energy caused by a small shear strain to a structured dispersion. In this analysis, high frequency deformation did not allow a measurable relaxation to occur and only nearest neighbour interactions using the pairwise additivity approach were considered. The theoretical shear moduli calculated by using the corrected Debye length which takes into account the increased counterion density and the decreased liquid volume with increasing the particle concentration, and a more realistic constant stern potential (16.5 mv) which was derived from the stress relaxation modulus, were found to be in good agreement with the experimental data. Failing to recognize the effect of counterions on Debye length or employing zeta potential to approximate the stern potential leads to incorrect or poor predictions.

(27) Some latex samples display the coexistence of an iridescent sediments and a milky white supernatant with a sharp horizontal boundary in between. The portion of ordered lower phase decreases linearly with increasing the electrolyte concentration and finally the disordered phase occupy the total volume of vial. The phase separation in a latex is difficult to understand because the latex particle size is below the critical diameter at which Brownian motion will outweigh sedimentation (166). One possible explanation is that the

crystallites behave as single units and are large enough to settle under gravity.

(28) The factor [1-(R_e/R)] represents the degrees of fluctuation of freedom for hard sphere away from the equilirium lattice site. The correlation of [1-(R_e/R)] with values of β (see (25)) at different particle concentrations is reasonabbly good when R_e is the effective hard sphere diameter which contains the corrected Debye length and R is the nearest interparticle distance. This finding indicates that the electrostatic repulsion force between particles plays a key role in crystal-like ordering of latex dispersions and justifies the use of the effective hard sphere model to theoretically account for the equilibrium preperties of colloidal dispersions. The monodisperse latexes have been classified by the following criteria according to the rigidity and β values obtained.

$\beta < 0.2$ or $R_e > 0.8R$: solid-like

$\beta \approx 0.2$ or $R_e \approx 0.8R$: liquid-like

$\beta >> 0.2$ or $R_e << 0.8R$: gas-like

(29) The ϕ-[Salt] phase diagram shows the order-disorder transition for latex A at 25 °C, as predicted by Kirkwood-Alder transition theory and by specifying effective hard sphere diameter in terms of the uncorrected or corrected Debye length (i.e. $1/\kappa_o$ or $1/\kappa$). Each phase diagram was comprised of three zones: order, disorder and coexistence of both. The predicted phase boundaries conform qualitatively with the data of Hachisu (32) in terms of the sigmoidal trend and the width of the coexistence region. The results also show that as the electrolyte concentration increases, the excess ions screen the electrostatic interactions more effectively, thinning the electrical double layer, thus requiring higher particle concentration to induce ordering. Experimental transition data attained from the visual observation of iridescence disappearance, fading reflection peak in optical study and vanishing elasticity in

the rheological study were used to test the validity of these predictions. Although qualitative agreement was obtained, both phase diagrams underestimate the phase transition at high electrolyte concentration, predicting higher melting and freezing particle concentration. The poor predictions resulted from an underestimation of effective interaction range between particles indicate that it might be better to define the effective hard sphere diameter in terms of a radial distance at which the pair potential magnitude is of the order of thermal energy.

(30) A proper theory for crystal melting would invoke the equality of free energies of the two phases (ordered and disordered dispersion in this case) in equilibrium. Phase diagram as a function of temperature and particle concentration for cleaned latex A can be constructed by applying above thermodynamics concept. Experimental phase transition data agree reasonably well with the predictions. Upon increasing the particle concentration, particles interact more rigorously and numerously. A higher temperature is thus required to disrupt the ordered structure by decreasing the strength and range of repulsive interactions and fueling the thermal particle motion.

(31) Experimental observations lead to the conclusion that van der Waals force is not essential for the ordering formation and the phase transition phenomena are therefore to be attributed mainly to electrostatic repulsion between particles. The order-disorder phase transition, rigidity or even the dynamics of monodisperse latexes with respect to the change in particle concentration, temperature, salt valency and concentration can be well explained in terms of the combined magnitude of pair potential energies which the middle particle feels.

(32) The structure of the ordered latexes has been examined by reflection spectrophotometry in Chapter 4 and identified as face-centered cubic at high

particle concentration. Melting enthalpy for the first order phase transition found in Chapter 6 is around 2.5 Kcal/mole which is comparable in magnitude to that of atomic crystals (167). The ordered latexes also possess rigidity against deformation, as shown in rheological study of Chapter 5. All the above indications suggest the ordered latex is a kind of "crystal".

(33) The rheological implications of ordered polymer colloids on printing were demonstrated by two examples in terms of the solid-liquid phase transition. One is the correlation of ink transfer with dynamic viscoelasticity of ink under given intaglio printing conditions, achieved with the dimensionless Deborah number as an liaison. The other is the phase diagram of printing inks constructed as a function of strain level and printing time by employing information from the characterized dynamic viscoelasticity of ink. This phase diagram which establishes the phase boundary between fluid-like and solid-like region provides a guideline for choosing the press parameters which in turn determine how the ink behaves rheologically during printing.

(34) An understanding of ink transfer requires an appreciation of the forces which the ink is subjected to and the time element involved in the printing process. The ink structures relax and recover during or between the different deformation events involved in printing. The ink is never at rheological equilibrium during the printing process because of the high speed printing and the long relaxation time required for the ink to respond deformation. Printing speed is thus expected to be a controlling factor for ink transfer. Experimental results show that intaglio ink transfer decreases linearly with decreasing phase shift of inks, i.e. increasing elastic response brought about by the increasing printing speed.

(35) Ink transfer with a deeper engraved cylinder exhibits higher sensitivity to the dynamic viscoelasticity of inks. Ink transfer with softer

impression material is higher because the impression material with lower modulus is deformed sufficiently to provide better ink-to-paper contact. Higher ink transfer can also be achieved by employing highly viscous varnish, decreasing solid content in the ink formulation or elevating printing temperature because all these actions tend to decrease the elastic response of inks.

Reference

1. E.J.W. Verwey and J.Th.G. Overbeek, *Theory of the Stability of Lyophobic Colloids*, Elsevier, Amsterdam, 1948
2. H.J. van den Hul and J.W. Vanderhoff in *Polymer Colloids*, R.M. Fitch, ed., p.1, Plenum Press, N.Y., 1971
3. P.A. Hiltner and I.M. Krieger, *J. Phys. Chem.* **73**, 2386(1969)
4. S. Hachisu and Y. Kobayashi, *J. Colloid Interface Sci.* **46**, 470(1974)
5. I.M. Krieger and P.A. Hiltner in *Polymer Colloids*, R.M. Fitch, ed., P.63, Plenum Press, N.Y., 1971
6. R. Williams, R.S. Crandall, and P.J. Wojtowicz, *Phys. Rev. Lett.* **37**, 348(1976)
7. T. Alfrey, Jr., E.B. Bradford, J.W. Vanderhoff and F. Oster, *J. Opt. Soc. Am.* **44**, 603(1954)
8. W. Luck, M. Klier and H. Wesslau, Ber. Bunsenges. *Phys. Chem.* **67**, 75,84(1963)
9. I.M. Krieger and F.M. O'Neill, *J. Am. Chem. Soc.* **90**, 3114(1968)
10. P.A. Hiltner, Y.S. Papir and I.M. Krieger, *J. Phys. Chem.* **75**, 1881(1971)
11. A. Kose, M. Ozaki, K. Takano, Y. Kobayashi and S. Hachisu, *J. Colloid Interface Sci.* **44**, 330(1973)
12. R. Williams and R.S. Crandall, *Phys. Lett.* **48A**, 225(1974)
13. N.A. Clark, A.J. Hurd and B.J. Ackerson, *Nature* **281**, 57(1979)
14. J.W. Goodwin, R.H. Ottewill and A. Parentich, *J. Phys. Chem.* **84**, 1580(1980)
15. S. Yoshimura, K. Takano and S. Hachisu in *Polymer Colloids II*, R.M. Fitch, ed., Plenum Press, N.Y., 1980
16. S. Hachisu and S. Yoshimura, *Nature* **283**, 188(1980)
17. P. Pieranski, *Phys. Rev. Lett.* **45**, 569(1980)
18. N. Ise and T. Okubo, *Acc. Chem. Res.* **13**, 303(1980)
19. M. Tomita, K. Takano and T.G.M. van de Ven, *J. Colloid Interface Sci.* **92**, 367(1983)
20. N. Ise, T. Okubo, M. Sugimura, K. Ito and H.J. Nolte, *J. Chem. Phys.* **78(1)**, 536(1983)
21. M. Tomita and T.G.M. van de Ven, *J. Colloid Interface Sci.* **100**,

112(1984)

22. T. Yoshiyama, I. Sogami and N. Ise, *Phys. Rev. Lett.* **53**, 2153(1984)

23. N. Ise, T. Okubo, K. Ito, S. Dosho and I. Sogami, *Langmuir* **1**, 176(1985)

24. N. Ise, K. Ito, T. Okubo, S. Dosho and I. Sogami, *J. Am. Chem. Soc.* **107**, 8074(1985)

25. M. Tomita and T.G.M. van de Ven, *J. Phys. Chem.* **89**, 1291(1985)

26. P. Pieranski and B. Pansu, *J. Phys. (Paris) Colloq.*, C3, **46**, 281(1985)

27. S. Yoshimura and S. Hachisu, *J. Phys. (Paris) Colloq.*, C3, **46**, 115(1985)

28. S. Hachisu and S. Yoshimura in *Physics of Complex and Supermolecular Fluids*, S.A. Safran and N.A. Clark, eds., Wiley-Interscience, N.Y., 1987

29. T. Okubo and S. Aotani, *Colloid Polym. Sci.* **266**, 1049(1988)

30. T. Okubo and S. Aotani, *Colloid Polym. Sci.* **266**, 1042(1988)

31. M. Wadati and M. Toda, *J. Phys. Soc.* Japan, **32**, 1147(1972)

32. S. Hachisu, Y. Kobayashi and A. Kose, *J. Colloid Interface Sci.* **42**, 342(1973)

33. A. Kose and S. Hachisu, *J. Colloid Interface Sci.* **46**, 460(1974)

34. S.L. Brenner, *J. Phys. Chem.* **80**, 1473(1976)

35. P.A. Forsyth, Jr., S. Marcelja, D.J. Mitchell and B.W. Ninham, *Adv. Colloid Interface Sci.* **9**, 37(1978)

36. P.R. Krumrine and J.W. Vanderhoff in *Polymer Colloids II*, R.M. Fitch, ed., p.289, Plenum Press, N.Y., 1980

37. P.M. Chaikin, P. Pincus, S. Alexander and D. Hone, *J. Colloid Interface Sci.* **89**, 555(1982)

38. K. Furusawa and S. Yamashita, *J. Colloid Interface Sci.* **89**, 574(1982)

39. P.N. Pusey and W. van Megen in *Physics of Complex and Supermolecular Fluids*, S.A. Safran and N.A. Clark, eds., P.673, Wiley-Interscience, N.Y., 1987

40. I.A. Aksay, W.Y. Shih and M. Sarikaya in *Ultrastructure Processing of Advanced Ceramics*, J.D. Mackenzie and D.R. Ulrich, eds., P.393, John Wiley & Sons, N.Y., 1988

41. Y. Monovoukas and A. P. Gast, *J. Colloid Interface Sci.* **128**, 533(1989)

42. J.M. Victor and J.P. Hansen, *J. Physique Lett.* **45**, L-307(1984)

43. D. Hone, *J. Phys. (Paris) Colloq.* C3, **46**, 21(1985)

44. I.A. Aksay and R. Kikuchi in *Science of Ceramic Chemical Processing*, L.L. Hench and D.R. Ulrich, eds., P.513, John Wiley & Sons, N.Y., 1986

45. G.Y. Onoda in *Science of Ceramic Chemical Processing*, L.L. Hench and D.R. Ulrich, eds., P.504, John Wiley & Sons, N.Y., 1986

46. W.Y. Shih, I.A. Aksay and R. Kikuchi, *J. Chem. Phys.* **86**, 5127(1987)

47. W. van Megen and I. Snook, *J. Colloid Interface Sci.* **57**, 40(1976)

48. I. Snook and W. van Megen, *J. Colloid Interface Sci.* **57**, 47(1976)

49. I. Snook and W. van Megen, *J. Chem. Soc. Far. Trans. II* **72**, 216(1976)

50. H. Fujita and K. Ametani, Japanese *J. Appl. Phys.* **16**, 1091(1977)

51. C.J. Barnes, D.Y.C. Chan, D.H. Everett and D.E. Yates, *J. Chem. Soc. Far. Trans. II* **74**, 136(1978)

52. J.A. Beunen and L.R. White, *Colloids & Surfaces* **3**, 371(1981)

53. I. Sogami, *Phys. Lett.* **96A**, 199(1983)

54. D. Hone, S. Alexander, P.M. Chaikin and P. Pincus, *J. Chem. Phys.* **79**, 1474(1983)

55. E.B. Sirota, H. D. Ou-Yang, S.K. Sinha, P.M. Chaikin, J.D. Axe and Y. Fujii, *Phys. Rev. Lett.* **62**, 1524(1989)

56. B. Dozier, H.M. Lindsay, P.M. Chaikin, H. Hervet, and L. Leger in *Lequid Crystals and Ordered Fluids*, Vol.4, A.C. Griffin and J.F. Johnson, eds., P.987. Plenum Press, N.Y., 1984

57. W.D. Dozier, H.M. Lindsay and P.M. Chaikin, *J. Phys. (Paris) Colloq.* C3, **46**, 165(1985)

58. N. Ise, T. Okubo, K. Ito, S. Dosho and I. Sogami, *J. Colloid Interface Sci.* **103**, 292(1985)

59. P.M. Chaikin, W.D. Dozier and H.M. Lindsay in *Hydrodynamic Behavior and Interacting Particle Systems*, G. Papanicolaou, ed., P.13, Springer-Verlay, N.Y., 198

60. P.M. Chaikin, J.M. di Meglio, W.D. Dozier, H.M. Lindsay and D.A. Weitz in *Physics of Complex and Supermolecular Fluids*, S.A. Safran and N.A. Clark, eds., P.65, Wiley-Interscience, N.Y., 1987

61. J.W. Goodwin and R.W. Smith, *Faraday Discussions of the Chemical Society* **57**, 126(1974)

62. I.M. Krieger and M. Eguiluz, *Trans. Soc. Rheol.* **20**, 29(1976)

63. R.S. Crandall and R. Williams, *Science* **198**, 293(1977)

64. S. Mitaku, T. Ohtsuki, K. Enari, A. Kishimoto and K. Okano, Japanese *J. Appl. Phys.* **17**, 305(1978)

65. T. Ohtsuki, S. Mitaku and K. Okano, Japanese *J. Appl. Phys.* **17**, 627(1978)

66. S. Mitaku, T. Ohtsuki and K. Okano, Japanese *J. Appl. Phys.* **19**, 439(1980)

67. T. Ohtsuki, A. Kishimoto, S. Mitaku and K. Okano, Japanese *J. Appl. Phys.* **20**, 509(1981)

68. K. Okano and S. Mitaku, *J. Physique* **41**, 585(1980)

69. W.J. van Megen, I.K. Snook and R.O. Watts, *J. Colloid Interface Sci.* **77**, 131(1980)

70. D.W. Benzing and W.B. Russel, *J. Colloid Interface Sci.* **83**, 178(1981)

71. W.B. Russel and D.W. Benzing, *J. Colloid Interface Sci.* **83**, 163(1981)

72. H.M. Lindsay and P. M. Chaikin, *J. Chem. Phys.* **76**, 3774(1982)

73. J.W. Goodwin and A.M. Khidher in *Colloid and Interface Sci.* Vol.IV, M. Kerker, ed., P.529, Academic Press, N.Y., 1976

74. J.W. Goodwin, T. Gregory and J.A. Stile, *Adv. Colloid Interface Sci.* **17**, 185(1982)

75. R. Buscall, J.W. Goodwin, M.W. Hawkins and R.H. Ottewill, *J. Chem. Soc. Faraday Trans.* 1, **78**, 2873(1982)

76. R. Buscall, J.W. Goodwin, M.W. Hawkins and R.H. Ottewill, *J. Chem. Soc. Faraday Trans.* 1, **78**, 2889(1982)

77. J.W. Goodwin, T. Gregory, J.A. Miles and B.C.H. Warre, *J. Colloid Interface Sci.* **97**, 488(1984)

78. J.F. Joanny, *J. Colloid Interface Sci.* **71**, 622(1979)

79. E. Dubois-Violette, P. Pieranski, F. Rothen and L. Strzelecki, *J. Physique* **41**, 369(1980)

80. P.M. Chaikin and P.A. Pincus in *Liquid Crystals and Odered Fluids*, Vol.4, A.C. Griffin and J.F. Johnson, eds., P.971, Plenum Press, N.Y., 1984

81. H.M. Lindsay and P.M. Chaikin, *J. Phys. (Paris) Colloq.* C3, **46**, 269(1985)

82. D.A. Weitz, W.D. Dozier and P.M. Chaikin, *J. Phys. (Paris) Colloq.*

C3, **46**, 257(1985)

83. H.M. Lindsay, W.D. Dozier, P.M. Chaikin, R. Klein and W. Hess, *J. Phys. A: Math. Gen.* **19**, 2583(1986)

84. S.A. Ali and M. Sengupta, *J. Colloid Interface Sci.* **113**, 172(1986)

85. F. Rothen, M. Jorand, A.J. Koch, E. Dubois-Violette and B. Pansu in *Physics of Complex and Supermolecular Fluids*, S.A. Safran and N.A. Clark, eds., P.413, Wiley-Interscience, N.Y., 1987

86. B.J. Ackerson in *Physics of Complex and Supermolecular Fluid* S.A. Safran and N.A. Clark, eds., P.553, Wiley-Interscience, N.Y., 1987

87. N.V. Churaev, *Colloid Journal of the USSR* **50**, 87(1988)

88. T. Okubo, *J. Colloid Interface Sci.* **135**, 259(1990)

89. I.M. Krieger, *Adv. Colloid Interface Sci.* **3**, 111(1972)

90. Th. F. Tadros, *Adv. Colloid Interface Sci.* **12**, 141(1980)

91. J.W. Goodwin in *Science and Technology of Polymer Colloids*, Vol. 2, G.W. Poehlein, J.W. Goodwin and R.H. Ottewill, eds., P.552, Martinus Nijhoff Pub., The Hague, 1983

92. R.L. Hoffman, ibid., P.571

93. Th.F. Tadros, ibid., P.531

94. Th.F. Tadros in *Materials Science Forum* **25**, 87(1988)

95. W.B. Russel, *J. Rheol.* **24**, 287(1980)

96. W.B. Russel in *Theory of Dispersed Multiphase Flow*, R. Meyer, ed., P.1, Academic Press, N.Y., 1983

97. W.B. Russel, *The Dynamics of Colloidal Systems*, The University of Wisconsin Press, Madison, 1987

98. I.M. Krieger in *Future Directions in Polymer Colloids*, M.S. El-Aasser and R.M. Fitch, eds., P.119, M. Nijhoff, Boston, 1987

99. N. Ise in *Biomimetic Chemistry*, Z.I. Yoshida and N. Ise, eds., P.115, Elsevier Scientific, N.Y., 1982

100. R.R. Myers and C.J. Knauss in *Applied Polymer Science*, ACS Symposium series #285, R.W. Tess and G.W. Poehlein, eds., P.749, American Chemical Society, Washington, D.C., 1985

101. D.W. J. Osmond and I. Wagstaff in *Dispersion Polymerization in Organic Media*, K.E. J. Barrett, ed., P.243, John Wiley & Sons, 1975

102. I.F. Efremov in *Surface and Colloid Science*, Vol.8, Egon Matijevic, ed., P.85, John Wiley & Sons, N.Y., 1976

103. P. Pieranski, *Contemp. Phys.* **24**, 25(1983)

104. I.M. Krieger in *Science and Technology of Polymer Colloids*, vol.2, G.W. Poehlein, J.W. Goodwin and R.H. Ottewill, eds., P.523, Martinus Nijhoff Pub., The Hague, 1983

105. C.A. Castillo, R. Rajagopalan and C.S. Hirtzel, *Reviews in Chemical Engineering* **2**, 237(1984)

106. W. van Megen and I. Snook, *Adv. Colloid Interface Sci.* **21**, 119(1984)

107. J.M. Ziman, *Models of Disorder*, Cambridge University Press, N.Y., 1979

108. A.A. Kamel, *The Preparation and Surface Characterization of Polystyrene Latexes as Model Colloids*, Ph.D. Thesis, Lehigh University, 1981

109. J.W. Vanderhoff, H.J. van den Hul, R.J.M. Tausk and J.Th.G. Overbeek in *Clean Surfaces: Their Preparation and Characterization for interfacial studies*, P.15, G. Goldfinger, ed., Marcel Dekker, N.Y., 1970

110. R.E. Wachtel and V.K. La Mer, *J. Colloid Sci.* **17**, 531(1962)

111. J.W. Vanderhoff, *J. Polym. Sci.: Polym. Symp.* **72**, 161(1985)

112. J.W. Goodwin, R.H. Ottewill, Robert Pelton, G. Vianello and D.E. Yates, *Br. Polym. J.* **10**, 173(1978)

113. M.S. El-Aasser, in *Science and Technology of Polymer Colloids*, G.W. Poehlein, J.W. Goodwin and R.H. Ottewill,eds., p.422, Martinus Nijhoff Pub., The Hague, 1983

114. R.H. Ottewill and J.N. Shaw, *Kolloid-Z.U.Z. Polymere* **218**, 34(1967)

115. W.C. Wu, *Preparation and Surface Characterization of Latexes as Model Colloids*, Ph.D. Thesis, Lehigh University, 1977

116. J.H. Stone-Masui and A. Watillon, *J. Colloid Interface Sci.* **52**, 479(1975)

117. W.C. Wu, M.S. El-Aasser, F.J. Micale and J.W. Vanderhoff in *Emulsions, Latices and Dispersions*, P. Becher and M.N. Yudenfreund, eds., Marcel Dekker, N.Y., 1978

118. J.H. Stone-Masui and W.E.E. Stone in *Polymer Colloids II*, R.M. Fitch, ed., Plenum Press, N.Y., 1980

119. L.J. Bellamy, *Infrared Spectra of Complex Molecules*, Methuen, London, Wiley, N.Y., 1958

120. J.N. Shaw and M.C. Marshall, *J. Polym. Sci.* **6A1**, 449(1968)

121. A.A. Kamel, C.M. Ma, M.S. El-Aasser, F.J. Micale and J.W. Vanderhoff, *J. Dispersion Sci. and Tech.* **2**, 315(1981)

122. P.C. Hiemenz, *Principles of Colloid and Surface Chemistry*, Marcel Dekker, N.Y., 1977

123. S. Ross and I.D. Morrison, *Colloidal Systems and Interfaces*, Wiley-Interscience, N.Y., 1988

124. P.H. Wiersema, A.L. Loeb and J.Th.G. Overbeek, *J. Colloid Interface Sci.* **22**, 78(1966)

125. R.W. O'Brien and L.R. White, *J. Chem. Soc. Faraday Trans. II* **74**, 1607(1978)

126. R.H. Ottewill and J.N. Shaw, *J. Electro Anal. Chem.* **37**, 133(1972)

127. R.H. Ottewill and J.N. Shaw, *Discuss. Faraday Soc.* **42**, 154(1966)

128. R.H. Ottewill and J.N. Shaw, *Kolloid Z.Z. Polym.* **218**, 34(1967)

129. J. Hearn, R.H. Ottewill and J.N. Shaw, *Br. Polym. J.* **2**, 116(1970)

130. J.W. Vanderhoff, F.J. Micale, M.S. El-Aasser and W.C. Wu, Polymer Preprint, Div. Polym. Chem., ACS, **16(1)**, 125(1975)

131. C.M. Ma, F.J. Micale, M.S. El-Aasser and J.W. Vanderhoff in *Emulsion Polymers and Emulsion Polymerization*, D.R. Bassett and A.E. Hamielec, eds., ACS Symposium series #165, 1981

132. R. Hidelgo Alvarez, F.J. de las Nieves, A.J. Van der Linde and B.H. Bijsterbosch, *Colloids and Surfaces* **21**, 259(1986)

133. B.C. Bonekamp, R. Hidalgo Alvarez, F.J. de las Nieves and B.H. Bijsterbosch, *J. Colloid Interface Sci.* **118**, 366(1987)

134. B.R. Midmore and R.J. Hunter, *J. Colloid Interface Sci.* **122**, 521(1988)

135. R. Hidalgo Alvarez, F.J. de las Nieves, A.J. Van der Linde and B.H. Bijsterbosch, *Colloid Polym. Sci.* **267**, 853(1989)

136. B.R. Midmore, R.J. Hunter and R.W. O'Brien, *J. Colloid Interface Sci.* **120**, 210(1987)

137. H. Maier, J.A. Baker and J.C. Berg, *J. Colloid Interface Sci.* **119**, 512(1987)

138. R.W. O'Brien, *J. Fluid Mech.* **190**, 71(1988)

139. A.J. Babchin, R.S. Chow and R.P. Sawatzky, *Adv. Colloid Interface Sci.* **30**, 111(1989)

140. H Tamai, K. Niino and T. Suzawa, *J. Colloid Interface Sci.* **131**, 1(1989)

141. M. Elimelech and C.R. O'Melia, *Colloids and Surfaces* **44**,

165(1990)

142. R.L.Rowell, S.-J. Shiau and B.J. Marlow, *Polymeric Materials: Sci. & Eng.* **62**, 52(1990)

143. E. Matijevic, *J. Colloid Interface Sci.* **43**, 217(1973)

144. R.C. Weast, *CRC Handbook of Chemistry and Physics*, 67th edition, CRC Press, Boca Raton, Florida, 1986

145. B.D. Cullity, *Elements of X-ray Diffraction*, 2nd. ed., Addison-Wesley, N.Y., 1978

146. I. Sogami, *Phys. lett.* A **96A**, 199(1983)

147. F. Rodriguez, *Principles of Polymer Systems*, 2nd. ed., McGraw-Hill, N.Y., 1982

148. S.J. Willey and L.W. Macosko, *J. Rheology* **22**, 525(1978)

149. E.P. Honig, W.F.J. Punt and P.H.G Offermans, *J. Colloid Interface Sci.* **134**, 169(1990)

150. Y.L. Wang, *J. Colloid Interface Sci.* **32**, 633(1970)

151. G.J. Harmsen, J. van Schooten and J.G.Th. Overbeek, *J. Colloid Sci.* **8**, 72(1953)

152. J.D. Ferry, *Viscoelastic Properties of Polymers*, John Wiley & Sons, N.Y., 1980

153. J. Alfrey and P.J. Doty, *J. Appl. Phys.* **16**, 700(1945)

154. R.L. Hoffman, *J. Colloid Interface Sci.* **46**, 491(1974)

155. R.L. Hoffman, *Adv. Colloid Interface Sci.* **17**, 161(1982)

156. R.M. Turian, *Ind. Eng. Chem. Fundam.*, Vol.11, No.3, 1972

157. J.R. Van Wazer, J.W. Lyons and K.Y. Lim, *Viscosity and Flow Measurements*, Wiley, N.Y., 1963

158. S. Glasstone, K.J. laidler and H. Eyring, *Theory of Rate Processes*, McGraw-Hill, N.Y., 1941

159. T.L. Smith, *J. Polym. Sci.: Part C*, No.**35**, 39(1971)

160. F.A. Lindemann, *Z. Phys.* **11**, 609(1910)

161. B.J. Alder, W.G. Hoover and D.A. Young, *J. Chem. Phys.* **49**, 3688(1968)

162. M.O. Robbins, K. Kremer and G.S. Grest, *J. Chem. Phys.* **88(5)**, 3286(1988)

163. J.G. Kirkwood, *J. Chem. Phys.* **7**, 919(1939)

164. B.J. Alder and T.E. Wainwright, *J. Chem. Phys.* **27**, 1208(1957)

165. B.J. Alder and T.E. Wainwright, *Phys. Rev.* **127**, 357(1962)

166. R. Buscall in *Science and Technology of Polymer Colloids*, Vol. 2, G.W. Poehlein, J.W. Goodwin and R.H. Ottewill, eds., P.279, Martinus Nijhoff Pub., The Hague, 1983

167. L.H. Van Vlack, *Elements of Materials Science and Engineering*, 3rd. ed., Addison-Wesley, Reading, MA, 1975

168. J.W. Kannel, Battelle Memorial Institute, Columbus, Ohio; private communication

Vita

Yann-Per Lee was born on October 2, 1960 in Taichung, Taiwan, Republic of China, the second son of Feng-Juh Lee and Rong-Tze Lin Lee. He received a B.S. degree in Chemical Engineering from National Cheng-Kung University, Tainan, Taiwan in June, 1982. He was awarded a citation from university president for excellence in moral and academic performances in 1980. After two-year military service in Chinese Army, he worked as a chemical engineer in the Power Plant of China Steel Corporation on water treatment and corrosion prevention.

Mr. Lee was married to Yuan-Yu Lo in June 1985 and came to United States of America for graduate study in August 1985. He became a research assistant at the Zettlemoyer Certer for surface Studies of Lehigh University and received his M.S. degree in Polymer Science and Engineering in May 1987. He was awarded a research fellowship from National Printing Ink Research Institute and continued to pursue Ph.D. degree in the same field. He served as the Secretary General of Chinese Student Club in Lehigh University from 1988 to 1989.

Mr. Lee has coauthored a paper on cheese viscoelasticity and published two papers from his doctoral work. Parts of his research have been presented at the August 1989 Annual Meeting of Fine Particle Society in Boston, the June 1990 64th Colloid and Surface Science Symposium in Bethlehem, PA and the 1990 AICHE Annual Meeting in Chicago. He is a member of American Chemical Society, Fine Particle Society and Society of Plastic Engineers.

After fulfilling the requirements for Ph.D. degree, Mr. Lee intends to work for The Procter & Gamble Company as a research scientist on the diaper product development.